Real-time control of the plasma density profile on ASDEX Upgrade

Dissertation
der Fakultät für Physik der
Ludwig-Maximilians-Universität München

vorgelegt von
Alexander Mlynek
aus München

München, 12. März 2010

Erstgutachter: Prof. Dr. Hartmut Zohm
Zweitgutachter: Prof. Dr. Piero Martin

Tag der mündlichen Prüfung: 20. Juli 2010

Zusammenfassung

Das Tokamak-Konzept stellt den aus heutiger Sicht aussichtsreichsten Ansatz zur zukünftigen Energiegewinnung durch kontrollierte Kernfusion dar. Besondere Bedeutung hat dabei die räumliche Verteilung der Teilchendichte in dem in toroidaler Geometrie eingeschlossenen Fusionsplasma. Bei einer gegebenen Teilchenzahl und einer gegebenen, zum Zentrum hin ansteigenden Temperaturverteilung lässt sich eine höhere Fusionsleistung erzielen, wenn das Dichteprofil im Zentrum des Fusionsplasmas zugespitzt ist. Eine zu starke Zuspitzung kann jedoch nachteilige Auswirkungen auf andere Plasmaeigenschaften haben. Die vorliegende Dissertation befasst sich daher mit der Fragestellung, inwieweit sich die Form des Dichteprofils im Fusionsexperiment ASDEX Upgrade, das vom Max-Planck-Institut für Plasmaphysik in Garching bei München betrieben wird, durch einen Regelkreis aktiv kontrollieren lässt.

Für eine solche Regelung des Dichteprofils, die im Rahmen dieser Arbeit in unterschiedlichen Entladungstypen experimentell demonstriert wurde, gibt es zwei wesentliche Grundvoraussetzungen:
Einerseits muss dazu das Dichteprofil während einer Plasmaentladung kontinuierlich unter Echtzeitbedingungen berechnet werden. Der Begriff "Echtzeit" bedeutet in diesem Fall, dass die Berechnung auf einer Zeitskala erfolgen soll, die kürzer ist als die Zykluszeit der Experimentsteuerung von etwa einer Millisekunde, und somit viel kürzer als die Zeitskala, auf der sich das Dichteprofil ändert. Die Berechnung des Dichteprofils basiert auf den Messungen eines Sub-Millimeter Interferometers, das die linienintegrierte Elektronendichte längs 5 verschiedener Sichtlinien durch das Plasma liefert. Bei der interferometrischen Dichtemessung können Messfehler auftreten, die auf das Verzählen um ganzzahlige Vielfache von 2π bei der Bestimmung des Phasenunterschiedes zwischen einem Mess- und einem Referenzstrahl zurückgehen. Da solche Messfehler erheblichen Einfluss auf das rekonstruierte Dichteprofil haben, besteht ein wesentlicher Teil dieser Arbeit in der Entwicklung einer neuen Auslese-elektronik für das Interferometer, anhand derer solche Messfehler in Echtzeit mit hoher Zuverlässigkeit erkannt werden können. Ein weiterer Teil dieser Arbeit behandelt die Erstellung eines Computeralgorithmus, der aus den linienintegrierten Messungen des Interferometers die räumliche Verteilung der Plasmadichte rekonstruiert. Die numerische Komplexität dieses Algorithmus muss so niedrig sein, dass er echtzeitfähig ist, die von ihm gelieferten Ergebnisse müssen den Dichteverlauf dennoch zuverlässig wiedergeben. Dieser Algorithmus ist auf einem Computer zu implementieren, der die Messdaten unter Echtzeitbedingungen zu anderen Computern, vor allem dem der Experimentsteuerung, kommuniziert.
Die zweite Grundvoraussetzung für den erfolgreichen Aufbau eines Regelkreises ist die Identifikation mindestens eines Stellgliedes, mit dessen Hilfe die Form des Dichteprofils beeinflusst werden kann. Die Wahl fiel hierbei auf die Elektronen-Zyklotron-Resonanzheizung (ECRH), mit deren Hilfe sehr lokal Leistung im Zentrum des Plasmas deponiert werden kann. Da ein Kopplungsmechanismus zwischen Temperatur- und Dichteprofil existiert, erlaubt das zentrale Heizen, je nach Entladungstyp, eine Abflachung oder Zuspitzung des Dichteprofils im Zentrum. Dieser Effekt konnte erfolgreich zur Regelung der Profilform genutzt werden.
Der letzte Teil dieser Arbeit untersucht diesen Kopplungsmechanismus zwischen Temperatur und Dichte genauer, insbesondere im Hinblick auf sein zeitliches Verhalten bei plötzlicher Änderung der zentralen Heizleistung. Hierbei wird die Ausbildung einer Hysteresekurve im lokalen Dichte-Temperatur-Diagramm beobachtet. Anhand eines einfachen

numerischen Modells wird schließlich aufgezeigt, dass das Zustandekommen einer solchen Hysteresekurve aufgrund der Transportgleichungen für Wärme und Teilchen zu erwarten ist. Insbesondere deuten die Ergebnisse, im Einklang mit theoretischen Vorhersagen, mit auf eine Temperaturabhängigkeit der Teilcheneinwärtsdrift hin.

Abstract

The tokamak concept currently is the most promising approach to future power generation by controlled thermonuclear fusion. The spatial distribution of the particle density in the toroidally confined fusion plasma is of particular importance. For a given number of particles and a given temperature distribution which increases towards the center, higher fusion power can be achieved when the density profile is peaked in the center of the fusion plasma. Too strong peaking, however, can be deleterious for other plasma properties. This thesis work therefore focuses on the question as to what extent the shape of the density profile can be actively controlled by a feedback loop in the fusion experiment ASDEX Upgrade, which is operated by the Max-Planck-Institut für Plasmaphysik in Garching near Munich.

There are basically two essential requirements for such feedback control of the density profile, which has been experimentally demonstrated within the scope of this thesis work:
On the one hand, for this purpose the density profile must be continuously calculated under real-time constraints during a plasma discharge. In this context, the expression "real-time" means that the calculation should be performed on a time scale shorter than the cycle time of the discharge control system of about one millisecond, and thus much shorter than the time scale on which the density profile changes. The calculation of the density profile is based on the measurements of a sub-millimeter interferometer, which provides the line-integrated electron density along 5 chords through the plasma. Interferometric density measurements can suffer from counting errors by integer multiples of 2π when detecting the phase difference between a probing and a reference beam. As such measurement errors have severe impact on the reconstructed density profile, one major part of this work consists in the development of new readout electronics for the interferometer, which allows for detection of such measurement errors in real-time with high reliability. A further part of this work is the design of a computer algorithm which reconstructs the spatial distribution of the plasma density from the line-integrated measurements. The numerical complexity of this algorithm has to be sufficiently low to permit its real-time application, and the results provided by the algorithm nonetheless have to reliably depict the density characteristics. This algorithm has to be implemented on a computer which communicates the measured data to other computers in real-time, especially to the tokamak control system.
On the other hand, a second fundamental requirement for the successful implementation of a feedback controller is the identification of at least one actuator which enables a modification of the density profile. Here, electron cyclotron resonance heating (ECRH) has been chosen, which permits a very localized power deposition in the plasma center. As a coupling mechanism between temperature profile and density profile exists, central heating effects a central flattening or peaking of the density profile, depending on the type of discharge. This effect was successfully exploited for feedback control of the shape of the density profile.
The last part of this thesis work investigates this coupling mechanism between temperature and density in more detail, especially with respect to the temporal behavior in response to sudden changes in the central heating power. Here, a hysteresis loop in the local density-temperature diagram is observed. With the help of a simple numerical model, it is finally shown that, based on the transport equations for heat and particles, the occurrence of such a hysteresis loop is expected. In particular, the results indicate a temperature dependence of the particle inwards drift, which is in agreement with theoretical predictions.

Contents

1 Introduction

1.1 Nuclear fusion as future energy source

Since the beginning of the Industrial Age, mankind has needed energy sources to energize stationary machines and means of traffic, to heat and air-condition buildings and to illuminate rooms and streets. With an increasing living standard in the industrialized countries, further energy demand arose in the recent decades, for instance for the operation of global telecommunication networks and mobile communication equipment. The global annual energy consumption of the growing world population is presently of the order of $5 \cdot 10^{20}$ J [1]. Today, the largest amount of energy is obtained by burning fossil resources like coal, oil or natural gas. Extracting them from earth's crust and burning them allows to set free the energy that was chemically bound over hundreds of millions of years. The fact that the consumption of fossil resources takes place on a time scale of a few hundred years, whereas their production has lasted almost a million times longer, results in two principal problems: On the one hand, there will be a point where all fossil resources have been used up. Depending on the evolution of worldwide energy consumption and the kind of resource, this may happen within a few decades or centuries. On the other hand, the amount of carbon dioxide that was extracted from the atmosphere by photosynthesis over a long period is now set free within short time. As CO_2 strongly enhances the greenhouse effect, this is expected to have impact on the global climate. Due to this awareness, there are currently international political efforts to limit the worldwide CO_2 emission.

As nuclear binding energies are of the order of several MeV per nucleon and thus much larger than molecular binding energies (several eV per atom), nuclear reactions can deliver an amount of energy with a gram of fuel for which chemical reactions (like the oxidation of carbon) would need tons of fuel. An atomic nucleus can be uniquely characterized by its atomic number Z and its mass number A and consists of Z protons and A-Z neutrons. The mass of the nucleus, however, is less than Z times the rest mass of a proton plus A-Z times the mass of a neutron. Using Einstein's energy-mass relation $E = mc^2$, the binding energy of a nucleus is defined as $E_b = \Delta m c^2$, where Δm is the previously mentioned mass difference. The binding energy in general increases with every nucleon that is added, but it is not strictly proportional to A, i.e. the binding energy per nucleon, E_b/A, is not constant. Figure 1.1 shows the binding energy per nucleon as a function of the mass number A.
There is a maximum of about 9 MeV in the $A = 60$ region. Towards higher and lower A, the binding energy per nucleon drops. So in general, a nuclear reaction will be exothermal if either heavy nuclei are fissioned, producing medium-mass nuclei, or if light nuclei are fused together. Fission reactions have been used for energy production for more than 50 years already. The fuel for fission reactors is either ^{235}U or ^{239}Pu, as these nuclides have

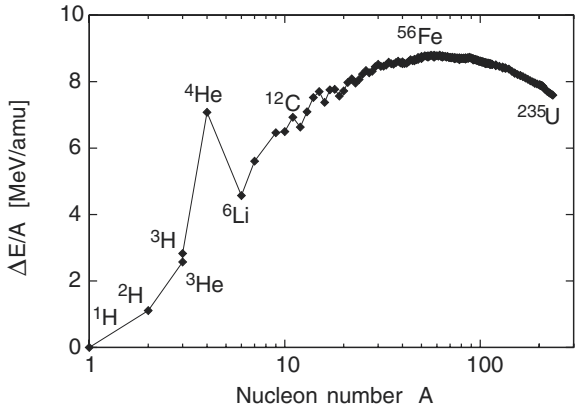

Figure 1.1: *The binding energy per nucleon as a function of the mass number [2].*

low barriers for n-induced fission (neutrons at thermal energy are sufficient) and the reaction produces several neutrons, so that a chain reaction can be achieved. As many fission products have long half-life periods, fission power plants produce radioactive waste that has to be stored for geological periods. Moreover, the large amount of radioactive material inside a fission reactor is very harmful to the biosphere if released in an accident. As the worldwide uranium resources are very limited, also this sort of power plant will run out of fuel within a few decades [1].
Fusion reactions are more difficult to achieve, as it is necessary to overcome the Coulomb barrier before two nuclei can be fused. As ^4He has an especially high binding energy per nucleon, reactions that produce this nuclide are highly desirable for a future fusion power plant. In the sun, the most important fusion reaction has the net equation

$$4\,^1H \rightarrow {}^4He + 2\,e^+ + 2\,\nu_e + 26.7\,\mathrm{MeV}\ .$$

As this reaction involves a process of weak interaction, cross sections are small. This, on the one hand, ensures the stability of stars over billions of years as it limits the reaction rate, but on the other hand, it makes this reaction unattractive for fusion reactors on earth. However, a weak process is not necessary if heavier isotopes of hydrogen are used as fuel. The main candidate is the reaction

$$^2D + {}^3T \rightarrow {}^4He + n + 17.6\,\mathrm{MeV}\ .$$

The proportion of deuterium in natural hydrogen is 0.015%, so the oceans contain almost unlimited fuel resources for a fusion rector. Tritium, however, is an unstable isotope with a half-life period of 12.3 years. There is hardly natural tritium on earth, except for a very small amount produced by cosmic radiation. So tritium has to be artificially produced, e.g. by the neutron-induced reactions

$$^6Li + n \rightarrow {}^3T + {}^4He + 4.8\,\mathrm{MeV}$$

$$^7Li + n \rightarrow {}^3T + {}^4He + n - 2.5\,\mathrm{MeV}\ .$$

[1] Breeder reactors could also use the nuclides ^{238}U and ^{232}Th as fuel, which would make the resources last much longer [3].

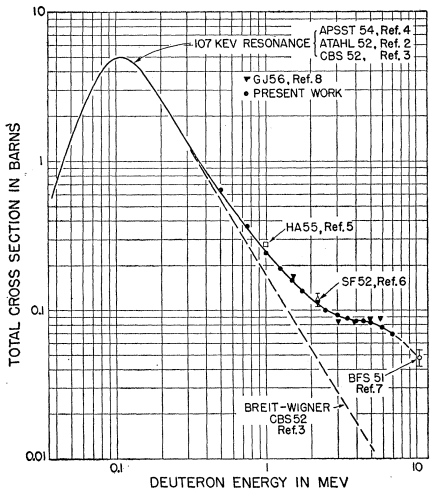

Figure 1.2: *The total cross section of the $T(D,n)^4He$ reaction as a function of the deuteron energy as published by S.J. Bame et al. in 1957 (see reference [4]).*

As the fusion of deuterium and tritium sets free an energetic neutron, it is possible to trigger one of the above breeding reactions to produce further tritium. Once started with an initial quantity of tritium, a future fusion power plant will therefore need deuterium and the alkali metal lithium as fuel, which exists in rich abundance in earth's crust and in the oceans.

To trigger a fusion reaction, the two nuclei have to move at sufficient relative velocity, so that the Coulomb barrier can be overcome. The cross section of the D+T reaction has been studied in fixed-target accelerator experiments, the diagram in figure 1.2 shows results from the 1950s for the total cross section as a function of the D projectile energy. Compared to other fusion reactions, the cross section is remarkably high due to a near excited state in the unstable ^5He nucleus, it reaches a maximum of about 5 barns[2] at a deuteron energy of about 107 keV, which corresponds to about 64 keV in the center of mass frame. With accelerators, it is easy to trigger this reaction, however, there would be no net energy gain as the projectile nucleus has a limited range in the target material and the likelihood of actually triggering a fusion reaction within this range is rather low. Per deuteron that actually reacts with a tritium nucleus in the target, many other deuterons are just stopped without triggering a reaction, meaning that their kinetic energy is dissipated, so the energy expended for their acceleration was therefore a fruitless investment. The only promising approach is to confine deuterium and tritium atoms in a fixed volume and to heat them up so far that the thermal energy reaches values of 10 keV or more and fusion reactions take place. The reaction rate in the resulting plasma is then determined by the temperature and the particle density. There is no vessel material available that could withstand such high temperatures, therefore, mainly two concepts are under investigation today: Inertial confinement and magnetic confinement. Only the latter approach will be discussed here,

[2] 1 barn $= 10^{-24} cm^2$

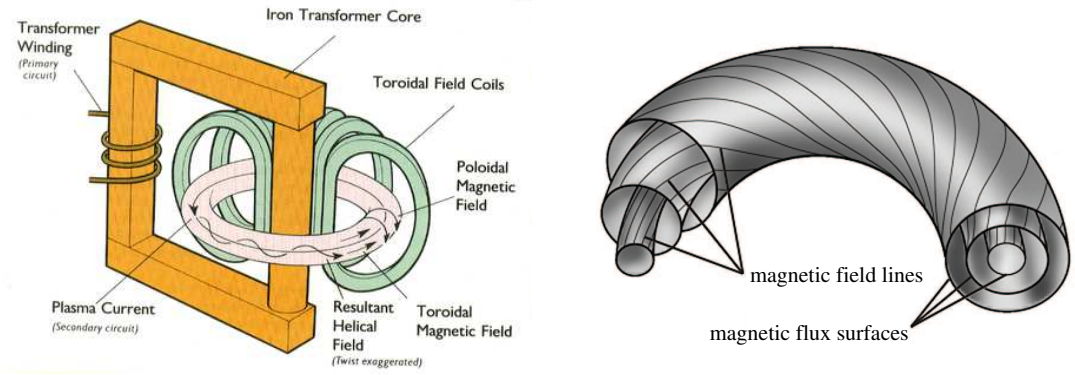

Figure 1.3: *Left: Schematic coil configuration of a tokamak. A plasma current is inductively driven by a transformer. Right: The resulting flux surfaces [5].*

which aims at confining charged particles such as D^+ and T^+ in an adequate magnetic configuration. When the desired fusion reaction takes place, the resulting neutron escapes from the setup due to its electric neutrality, whereas the helium nucleus is still confined and deposits its kinetic energy in the plasma. When the plasma heating by the helium nuclei compensates for all energy losses, which result e.g. from heat transport, particle loss at the edge, bremsstrahlung or line radiation from impurity atoms, one obtains a self-sustaining fusion reaction. Without any external heating, the fusion plasma remains at high temperature and delivers energy in form of the escaping neutrons. The point where the external heating can be switched off is called 'ignition'.

1.2 The Tokamak concept

In a homogeneous magnetic field, charged particles gyrate around the field lines at the Larmor frequency $\omega = \frac{B\,q}{m}$. That way, they are confined in two directions, but can move freely along the third coordinate, i.e. parallel to $\vec{B}$. A cylindrical volume filled with a magnetic field parallel to the cylinder axis can therefore confine a fusion plasma, however, this configuration would lose particles at the ends of the cylinder. The concept of tokamaks and stellarators consists in bending the cylindrical volume to toroidal shape, so that the two critical ends are eliminated. However, in this configuration, the strength of the B-field decays like $1/R$, where R is the distance from the symmetry axis. In this inhomogeneous magnetic field, the gyrating particles feel a force parallel to the torus axis, whose direction depends on the sign of their electric charge. As a result of this drift, an electric field parallel to the torus axis will occur which compensates the force. However, in the presence of this additional electric field, an $\vec{E} \times \vec{B}$ drift occurs and makes the particles move outwards. Therefore, such configuration would be unstable. The solution is to give the magnetic field an additional component in the poloidal direction. This can either be achieved by using a complex non-planar magnetic coil configuration (stellarator) or by driving a toroidal current in the plasma (tokamak). This results in twisted field lines which form nested flux surfaces (see figure 1.3). As particles can move easily along field lines of a flux surface, important plasma parameters like density and temperature are usually constant on each of these surfaces. The plasma current in a tokamak device is generated inductively with

the help of a central transformer coil. As the plasma has non-zero electric resistance, the plasma current decays when the transformer current is kept constant. The resistive losses have to be compensated by continuously ramping the transformer current in one direction. As the transformer coil will reach its current limit at a certain point, a tokamak only allows pulsed operation today. In the future, this problem may be overcome by non-inductive current drive mechanisms. A stellarator, in contrast, is inherently adequate for steady-state operation, but due to the complex coil geometry, its construction is a bigger challenge than the construction of a tokamak. Among today's magnetic confinement fusion experiments, the tokamak concept is the more frequent one.

As the volume of the plasma, in which fusion reactions can take place, grows with the third power of the dimensions of a tokamak, but the surface, through which energy and particles can be lost, only with the second power, building a new device larger than its predecessor is always beneficial for achieving new milestones in energy confinement. Based on today's knowledge, it is expected that a tokamak that achieves ignition will have to have a major radius that is of the order of about 10 meters. Due to financial constraints, such device has not yet been built. Today, the largest existing tokamak is the Joint European Torus (JET) in Great Britain which has a major plasma radius of about 3 meters. The next significant step in size will be made by the International Thermonuclear Experimental Reactor (ITER) with a major radius of more than 6 meters, whose construction in Cadarache/France has recently started. As tritium is radioactive and its handling therefore requires a complex technical setup, most research on tokamaks is done in pure deuterium. Only JET and the Tokamak Fusion Test Reactor (TFTR) in Princeton/USA have been operated with tritium, where JET achieved a peak fusion power of 16.1 MW in the year 1997.

1.3 Aim of this work

Precise knowledge and control of the plasma density is of utmost importance in tokamak operation as on the one hand, the achievement of a high density is essential for obtaining high fusion rates. For a fuel mixture consisting of 50% deuterium and 50% tritium, the reaction rate per unit volume is given by

$$R = \frac{1}{4} n^2 \langle \sigma v \rangle \ ,$$

where n is the density and $\langle \sigma v \rangle$ is the average of the product of cross section and particle velocity. On the other hand, however, exceeding certain density limits makes the plasma discharge unstable and may result in a sudden disruption of the plasma current. Empirically, the so-called Greenwald limit to the average density $\bar{n}$ has been found:

$$\bar{n}[10^{20} m^{-3}] < \frac{I[MA]}{\pi a^2 [m^2]} \ .$$

In this equation, I is the plasma current and a the minor plasma radius. Also the spatial distribution of the plasma density (density profile) is important. On the one hand, a tokamak plasma that contains a given number of particles will provide higher fusion rates when the density is not uniform all over the volume, but concentrated in the hot center, with lower density at the edge. This is due to the temperature dependence of the cross section

σ and the n^2 dependence of the fusion rate. On the other hand, there are some critical spatial distributions of density that make the discharge unstable and therefore have to be avoided.
On ASDEX Upgrade, feedback control of the average density $\bar{n}$ is routinely done by interferometry. One major aim of this work is to demonstrate active feedback control of the shape of the plasma density profile. For this purpose, the density profile has to be continuously calculated by a computer from the measurements of a sub-millimeter interferometer and magnetic probes during the discharge, and this profile has to be used for real-time feedback control. As the output of the interferometer can be affected by measurement errors which cause a significant distortion of the calculated density profile, one major part of this work is the development of a scheme that allows for automatic detection of such measurement errors on a time scale of less than a millisecond. Once the density profile is available in real-time, actuators are to be identified which allow to influence the shape of the density profile, and the underlying physical mechanisms of this response of the density profile shall be explored, based on today's understanding of transport. Finally, the feasibility of active control of the profile shape shall be experimentally demonstrated.

In the following chapter, the basic principles of heat and particle transport in a tokamak plasma will be discussed. Chapter 3 presents the main characteristics of ASDEX Upgrade and introduces the electron cyclotron resonance heating (ECRH) and two plasma diagnostics that will be relevant in the further discussion. Chapter 4 describes the principle of interferometric density measurement and the interferometer setup on ASDEX Upgrade. In chapter 5, the development of new readout electronics for the interferometer, which was carried out within this work, is presented. In addition, the new possibilities provided by this system, especially with respect to real-time detection of measurement errors, are discussed. Based on the line-integrated density measurements along several lines of sight provided by the interferometer, the spatial distribution of density has to be reconstructed. This is especially challenging when the result has to be available in real-time. In chapter 6, a computer algorithm is presented whose numerical complexity is low enough to meet the real-time requirement, but which nevertheless yields results that are in good agreement with the density profiles provided by a more complex algorithm. Chapter 7 gives an overview of the experiments for profile control that have been carried out on ASDEX Upgrade. In chapter 8, the experimental data is analyzed and particle transport studies are carried out with the help of a simple simulation code. Chapter 9 summarizes the results and gives an outlook on future applications of real-time density profile determination.

2 Particle transport in Tokamak plasmas

In most cases, the particle source in tokamak plasma discharges is only peripheral. The most common fueling method is gas puffing from the edge, although also some non-peripheral fueling methods exist, such as neutral beam injection and the injection of frozen hydrogen pellets. Taking only into account diffusive particle transport, i.e. particle fluxes that are driven by density gradients, one would expect that in the absence of particle sources and sinks inside the plasma, a state of equilibrium occurs in which there is no net particle flux and thus no density gradient. Accordingly, the density profile would be flat. However, experiments show that the density profiles observed in tokamaks are regularly peaked in the center, even when the particle source is only peripheral [6]. This shows that the particle transport is not of purely diffusive nature. In contrast, there has to be an additional inward transport mechanism which balances the diffusive outward transport and allows for an equilibrium profile which is centrally peaked.
Empirically, the following ansatz is made for the particle flux $\vec{\Gamma}$ and the heat flux $\vec{q}_{heat}$ [7, 6, 8]:

$$\vec{\Gamma} = -D\vec{\nabla}n_e - C_T n_e \frac{\vec{\nabla}T}{T} + \vec{v}_p n_e \tag{2.1}$$

$$\vec{q}_{heat} = -\chi n_e \vec{\nabla}T + \vec{v}_E n_e T \tag{2.2}$$

In the first equation, the first term contains the diffusion coefficient D and describes diffusive transport, which tries to balance any density gradient. The second term is referred to as thermodiffusion and was introduced due to the observation that also temperature gradients can drive particle transport. The last term is the so-called pinch term, a pure convection term which includes effects that do not depend on density and temperature gradients, such as the previously mentioned inward transport mechanism that is evidently present in discharges with centrally peaked density profile.
The equation for the heat flux contains the heat conductivity χ and a possible heat pinch $\vec{v}_E$, which is often neglected.

2.1 Classical transport

As discussed in section 1.2, the basic idea of magnetic confinement fusion is to make use of the Lorentz force which makes charged particles gyrate around the field lines when they move in a magnetic field and have a velocity component perpendicular to the field lines. That way, the motion of the particles is restricted in two directions, just the velocity component in the direction of the magnetic field remains unaffected. When discussing the trajectory of a particle, one often uses the time-averaged position of the particle during one turn on the gyro-orbit, the so-called guiding center. A cylindrical volume of infinite

length (or one of finite length with perfectly reflecting mirrors at the ends) that is filled with a homogeneous magnetic field parallel to the cylinder axis is able to confine a fusion plasma. Let us assume that some plasma parameters like the temperature and the density are not homogeneous within the volume. Any gradient of temperature and density will quickly balance in the direction parallel to the cylinder axis, as particles can move freely along this coordinate. A gradient perpendicular to the field lines, however, can only be compensated when gyrating particles leave their orbit. This can happen due to Coulomb collisions of particles whose gyro-orbits overlap. As a result of the momentum transfer in the collision, the particles find themselves on different orbits afterwards, where the average displacement per collision is of the order of the gyro-radius. This gives rise to a diffusive particle and energy transport. The diffusion coefficient D in equation 2.1 can be estimated on the basis of a random walk model, where the step size is the gyro-radius r_{gyro} and the time in between two steps is the inverse collision frequency $1/\nu$. This leads to the diffusion coefficient

$$D_{class} \sim r_{gyro}^2 \, \nu \, .$$

For the given cylindrical geometry, this is referred to as 'classical transport'.

So far, a homogeneous magnetic field has been assumed. As this will be relevant in the further discussion, let us now consider a magnetic field whose strength varies along the cylinder axis, which will be labeled as the 'z'-axis. To fulfill the condition $\vec{\nabla} \cdot \vec{B} = 0$, the magnetic field must also have components in the x- and/or y-direction in this case. Here we discuss the simple case that we have rotational symmetry with respect to the z-axis, see figure 2.1. When a particle with mass m gyrates around the z-axis with a velocity $v_\perp = \sqrt{v_x^2 + v_y^2}$ and

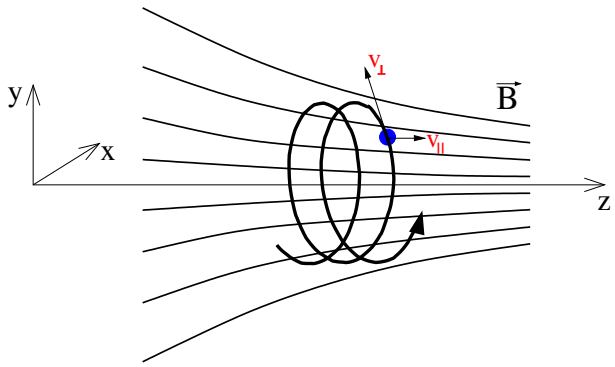

Figure 2.1: *The magnetic mirror effect: A charged particle is moving in a magnetic field whose strength increases along the z-axis. The particle's velocity vector has a component v_z in the z-direction, and its projection to the x-y-plane is labeled $v_\perp$. The configuration is rotationally symmetric with respect to the z-axis.*

has an additional velocity component v_z in the z-direction, then it encounters an increasing strength of the magnetic field. On the one hand, the kinetic energy $E_{kin} = \frac{1}{2}m(v_\perp^2 + v_z^2)$ of the particle is conserved, and on the other hand, the magnetic moment $\mu = \frac{1}{2}mv_\perp^2/B$ is an adiabatic invariant[1], i.e. it is conserved when the change of the strength of the magnetic field occurs on a longer time scale than the gyration of the particle. Inserting the definition

[1] A proof of this can e.g. be found in [9].

of the magnetic moment into the equation for the kinetic energy and solving with respect to v_z yields:

$$v_z = \sqrt{\frac{2E_{kin}}{m} - v_\perp^2} = \sqrt{\frac{2E_{kin}}{m} - \frac{2\mu B}{m}} \tag{2.3}$$

This means that the velocity in the z-direction decreases with increasing field strength and becomes zero at

$$B_{max} = \frac{E_{kin}}{\mu} = \left(1 + \frac{v_z^2}{v_\perp^2}\right) \cdot B \,. \tag{2.4}$$

Depending on the ratio of v_z and $v_\perp$, there is a maximum magnetic field strength up to which the particle can penetrate. Then it is reflected. This is the principle of a magnetic mirror. For completeness, it should be mentioned that the same effect is observed when the magnetic field is not parallel to the z-axis, but has a curvature.
As any real fusion device has finite length, cylindrical approaches need to close their ends with mirrors. For this purpose, the magnetic mirror effect can be used by increasing the field strength at the ends. However, there is a critical ratio of v_z and $v_\perp$ above which particles can escape from the device.

2.2 Neoclassical transport

In a fusion device with toroidal geometry, the strength of the magnetic field is not constant over the whole plasma volume, but varies like $1/R$, where R is the distance from the symmetry axis of the torus. This causes a couple of additional effects, which are referred to as 'neoclassical' transport. As described in section 1.2, the gradient-B drift causes particles to move parallel to the symmetry axis, where the direction depends on the sign of their charge. This charge separation gives rise to an electric field, which in turn causes an $\vec{E} \times \vec{B}$ drift that is directed perpendicular to the symmetry axis. A particle that drifts towards the symmetry axis approaches the plasma center when it is at the outer side of the torus and it moves away from the plasma center when it is at the inner side, compare figure 2.2. That

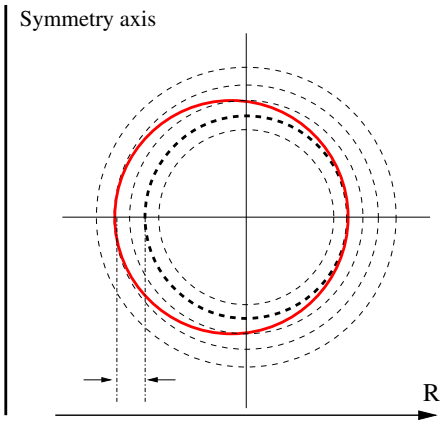

Figure 2.2: *Poloidal projection of the trajectory of the guiding center of a passing particle in a tokamak plasma. During half a turn in the poloidal direction, it is displaced from its original flux surface and returns to it within the next half turn. [7]*

way, there is no net motion when the particle has completed one turn in the poloidal plane, which is the fundamental purpose of the tokamak configuration. Nevertheless, during half a turn in the poloidal direction, the particle is displaced from its flux surface, which results in additional transport perpendicular to the flux surfaces.
Another effect in toroidal geometry is based on the magnetic mirror effect. When a gyrating particle moves along a field line, it periodically moves from regions with lower magnetic field at the outer side of the torus to regions with stronger field at the inner side and back. If the ratio of the velocity components parallel and perpendicular to the field line is below a critical value (see equation 2.4), the particle is reflected before it reaches the innermost point of the flux surface. In this case, the particle gets trapped and its trajectory is a closed curve with the shape that is illustrated in figure 2.3. As the poloidal projection of this

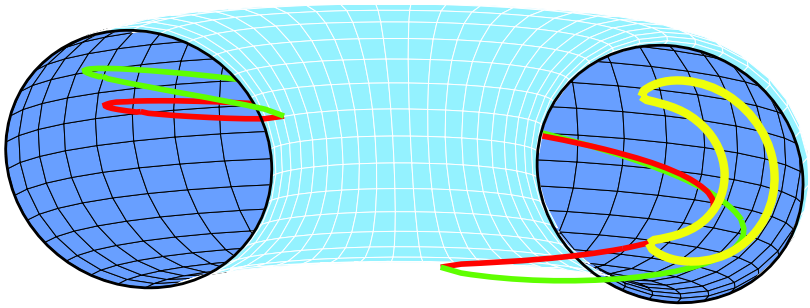

Figure 2.3: *Illustration of the trajectory of the guiding center of a trapped particle in a tokamak. The green and the red curve represent the actual 3-dimensional orbit of the particle, whereby color changes at the points where the particle is reflected. The yellow curve is the projection of the orbit onto the poloidal plane, which has a banana-like shape. [10]*

trajectory looks similar to the shape of a well-known tropical fruit, this is usually referred to as 'banana-orbit'. As this orbit crosses several flux surfaces, it causes an additional transport perpendicular to the magnetic field. The impact of trapped particles on the total transport depends on the mean free path of the particles between two collisions. When it is comparable to or larger than the length of the banana curve, then those particles significantly contribute to the transport and one talks about the 'banana regime'. On the contrary, when the particle suffers from several collisions before it can complete one banana orbit, the situation is called 'Pfirsch-Schlüter regime'. One introduces the collisionality ν to characterize how frequently plasma particles suffer from collisions. The neoclassical diffusion coefficient D can be estimated by assuming that a displacement of the trapped particle by the radial extension w_b of the banana orbit occurs with an effective collision frequency ν_{eff}, which takes into account the fraction of trapped particles. In the banana regime, it can be written as:

$$D_{neoclass} = w_b^2 \, \nu_{eff}$$

This is much larger than the classical diffusion coefficient.

As the plasma in a tokamak has non-zero electric resistance, a toroidal electric field has to be created by sweeping the current in the central transformer in order to maintain a constant plasma current. In the presence of this electric field, trapped particles are accelerated when they are on the one side of the banana orbit and they are slowed down on the other

side. As a result of this, the velocity parallel to the magnetic field lines is different at the two ends of the banana orbit. Consequently, the maximum B-field up to which the particle penetrates before being reflected is also different. This leads to a slight displacement of the banana curve from bounce to bounce, see figure 2.4. Accordingly, the trajectory of the

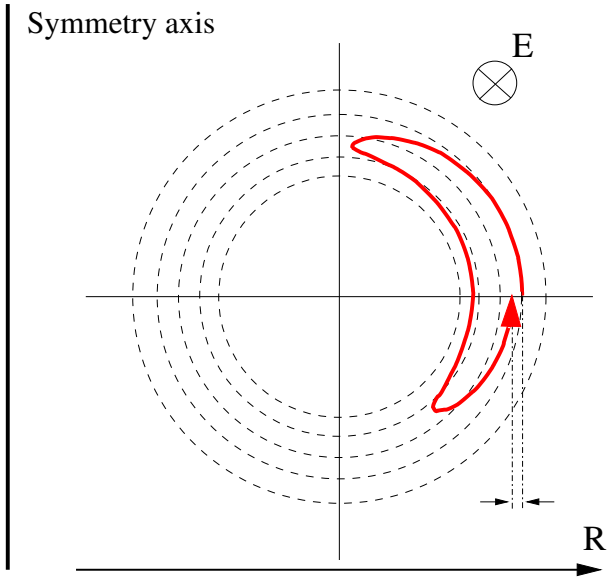

Figure 2.4: *The origin of the Ware-pinch: Due to the toroidal electric field present in a tokamak, the trapped particle is accelerated on the one half of the banana orbit and slowed down on the other. Reflection therefore occurs at slightly different field strengths, i.e. different major radii, which results in an inward displacement of the orbit. [7]*

guiding center of the particle is no longer a closed curve, but moves further and further to the plasma center. This effect, which results in a particle transport that is always directed inward, is called the neoclassical Ware-pinch. It is only important when a high loop voltage is generated by the central transformer.

Experiments have shown that the actually observed transport is mostly much larger than what is expected from purely neoclassical effects.
Regarding the heat transport by ions, the actually observed values exceed the neoclassical prediction typically by a factor of 2 to 10 [11]. Even larger deviation is observed for the electron heat transport, where the actual values are by a factor between 10 and 1000 higher. In contrast, the experimentally observed transport of impurity ions in the plasma has been found to be consistent with neoclassical calculations under certain conditions, compare reference [12]. For other plasma parameters, however, diffusion coefficients are reported in this reference which are up to a factor of 10 above the neoclassical level.
Regarding the particle diffusion coefficient D, the neoclassical prediction for the main particle species (main ions and electrons) is far below the experimental values. The inward convection velocity v_P predicted by neoclassical theory can be consistent with the experiment under certain conditions. This is especially true for the Ware pinch at high collisionality and high loop voltage [13].

2.3 Turbulent transport

Historically, the additional transport that was found in the experiments has been labeled 'anomalous transport'. Further investigations led to the conclusion that transport in tokamaks is dominated by radially extended turbulence eddies. Up to now, no fully self-consistent description of turbulent transport has been found. One approaches the problem from the theoretical side with gyrokinetic computer simulations, which operate on a discrete grid. The power of currently available supercomputers sets an upper limit to the number of particles and time steps to be taken into account. It has been found that turbulence eddies are driven by microinstabilities such as the ion temperature gradient (ITG) or the trapped electron mode (TEM). Those modes occur due to the different mobility of particles along the field lines. Passing electrons are most mobile, ions of same temperature are slower than electrons due to their much larger mass, and trapped electrons have only a minimum amount of mobility.
Figure 2.5 illustrates the origin of the ITG instability. As the temperature is high in the

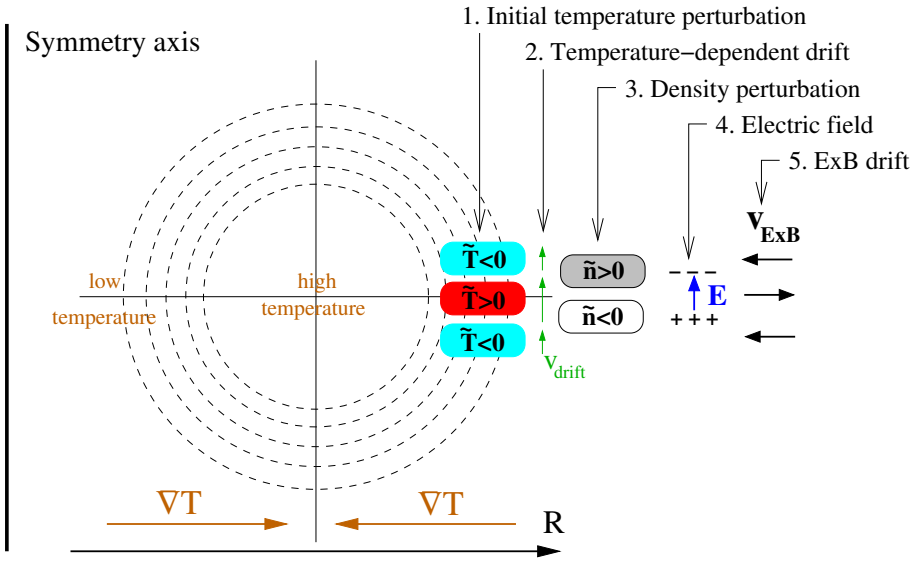

Figure 2.5: *The origin of the ion temperature gradient (ITG) instability. An initial temperature perturbation causes a density perturbation due to temperature-dependent drifts. The adiabatic reaction of the passing electrons results in an electric field which in turn causes an $\vec{E} \times \vec{B}$ drift that amplifies the initial perturbation.*

core and low at the edge, the temperature gradient points towards the plasma center. The gradient of the magnetic field, however, is always directed towards the torus axis, due to the 1/R dependence of the toroidal field strength. We assume an initial temperature perturbation of the ions on the outboard side of the torus. As the gradient-B drift and the curvature drift depend on the particle velocity and thus on the temperature, particles in the hot region drift faster than those in the cold region. This results in a density perturbation of the ions. To maintain the quasi-neutrality of the plasma, the passing electrons as the most mobile species show an instantaneous adiabatic reaction. The force balance parallel to the field lines implies an electrostatic potential, which results in an electric field that in turn causes an $\vec{E} \times \vec{B}$ drift. As the figure illustrates, this $\vec{E} \times \vec{B}$ drift makes the volume

with the initially higher temperature move away from the symmetry axis, i.e. into colder regions. That way, the initial perturbation is amplified on the outboard side of the torus, where temperature gradient and B-field gradient are pointing into the same direction. At the inboard side, however, the temperature gradient has different sign and the $\vec{E} \times \vec{B}$ drift therefore compensates for the initial temperature perturbation. As figure 2.6 illustrates, this instability causes turbulence eddies at the low-field side of the torus. The left part of the figure shows the torus surface. There, it can be seen that the regions of hotter and colder plasma are extended along the field lines. It should be noticed that the mechanism

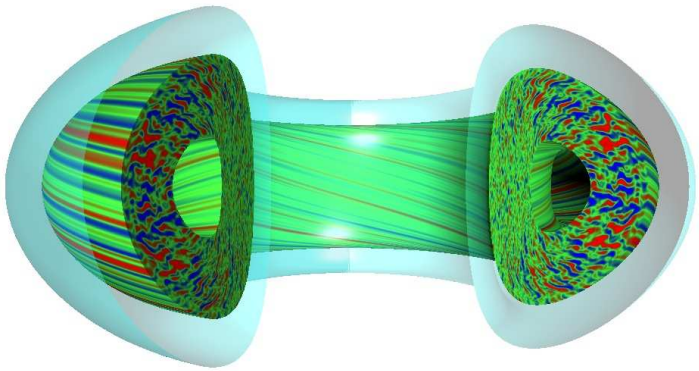

Figure 2.6: *Graphical representation of a turbulence simulation in toroidal geometry. The largest eddies occur on the low-field side. [14]*

discussed so far only results in a heat transport, but as the number of ions moving inwards and outwards is the same, there is not net particle transport yet. Only when trapped particles come into play, which are no longer able to show an adiabatic response, or other effects braking adiabatic electron response, for instance Landau damping or collisions, a phase delay between the perturbation of the electrostatic potential and the density occurs, resulting in a net particle transport.
If there is an initial perturbation of the density of trapped electrons, a mechanism similar to that for the ions exists which causes the so-called trapped-electron mode (TEM) instability. In case of the TEM, the slow motion along the field lines is caused by trapping to the small banana orbits, and not by inertia as in case of the ions. Which of the two modes (ITG or TEM) to be the most unstable depends on plasma parameters such as the gradients and the ratio of electron and ion temperature and the collisionality. The TEM, for example, is stabilized by electron-ion collisions as they result in trapping and de-trapping processes. In many cases, one turbulence type is dominant, but also a coexistence of two equally unstable modes can occur.
Gyrokinetic simulations allow to make a prediction on the transport coefficients D, C_T, $\vec{v}_p$ and χ in equations (2.1) and (2.2). Like for classical and neoclassical transport, an estimation of the diffusion coefficient D can also be made for turbulent transport. Here, an average displacement of a particle by the eddy size r_{eddy} within the decorrelation time τ_{decorr} can be assumed, leading to

$$D_{turb} = \frac{r_{eddy}^2}{\tau_{decorr}} .$$

Empirically, a self-similarity of the temperature profiles in a tokamak plasma has been found. The temperature profile between the magnetic axis and the edge region as a whole scales with the edge temperature, but besides this scaling, the profiles are almost identical. Even when applying local heat sources, the shape of the profile remains almost unchanged. This is often referred to as 'stiffness' of temperature profiles. This behavior is explained by a very large derivative of the heat conductivity χ with respect to the temperature gradient above a certain threshold, see figure 2.7. When the temperature is locally increased by an

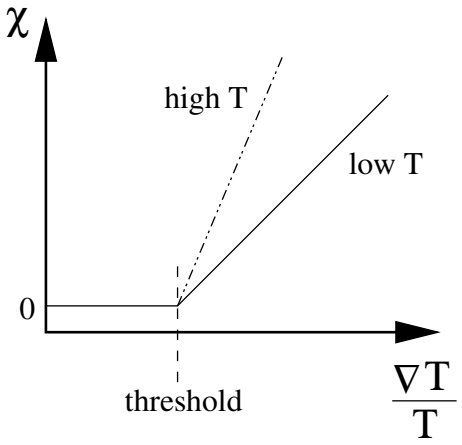

Figure 2.7: *Dependence of the heat transport coefficient χ on the temperature gradient. Above a certain threshold, χ increases with increasing ∇T, with a slope that is proportional to $T^{3/2}$ according to the gyro-Bohm theory. As a result of this, the profiles become stiffer at higher temperature.*

external heating source, this immediately causes a steep increase of the heat conductance. That way, the injected thermal energy is spread over the whole plasma volume, resulting in a global increase of temperature without modification of the shape of the temperature profile. One therefore has to keep in mind that the transport coefficients are a function of the density and temperature gradient, therefore, equations (2.1) and (2.2) cannot be interpreted as a linear relationship.

The density profiles observed in tokamaks are regularly peaked in the center, although the particle source is only peripheral in most cases [6]. This indicates that there has to be a particle influx, as described by the pinch term $\vec{v}_p$, which balances the diffusive outward flux that occurs for a peaked density profile. A candidate for this is the neoclassical Ware pinch, which could actually be identified in some experiments. However, for most plasma conditions, the Ware pinch is much too weak to explain the observed peaking of the density profile. This leads to the conclusion that there has to be some non-neoclassical, i.e. turbulent inward pinch. This has been proven in experiments where peaked profiles have been observed at zero loop voltage, which entirely excludes the occurrence of the Ware pinch [15].
Furthermore, experiments have shown that the particle source, which can be at least partially non-peripheral in case of neutral beam injection into the plasma, has not much impact on the shape of the density profile [6]. The density profile is mainly determined by the ratio of the turbulent diffusion and the turbulent inward pinch.

As the focus of this thesis is on real-time control of the density profile, the question arises how the shape of the profile can be actively influenced. In [16], the impact of central electron heating on the density profile is described. Figure 2.8 illustrates the results for low-confinement mode as well as for high-confinement mode. In this diagram, the ratio of

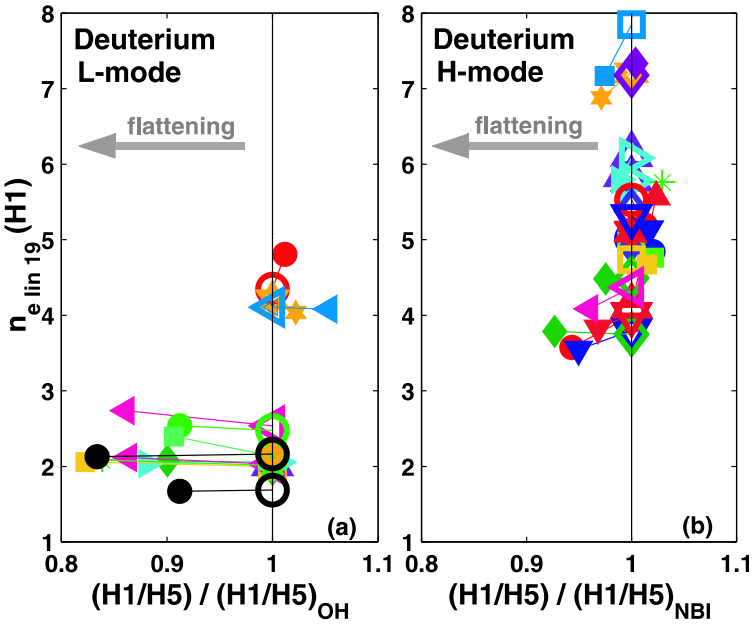

Figure 2.8: *Response of the density profile to central electron heating for L- and H-mode discharges at different densities. On the abscissa, the the ratio of the interferometer channels H-1 and H-5 is plotted, which was normalized to 1 for the case without ECRH (open symbols). Filled symbols represent the case with ECRH. On the ordinate, the line-integrated density for interferometer channel H-1 is shown. [16]*

two channels of the ASDEX Upgrade interferometer is used as peaking parameter. The line of sight of channel H-1 goes almost through the plasma center, whereas H-5 is a peripheral channel (compare figure 4.7 in chapter 4.4). The more peaked the density profile is, the larger the ratio H-1/H-5 becomes. In the diagram, this peaking parameter has been normalized to one for the case without additional electron heating, which is plotted with open symbols. The filled symbols represent the case with central electron heating. On the ordinate, the line-integrated electron density measured by the central interferometer channel is plotted. It can be seen that for low-density L-mode discharges, central electron heating causes a significant flattening of the density profile. This process of reducing the central electron density is commonly referred to as density 'pump-out' in the literature. At higher densities of the order of $4 \cdot 10^{19}\, m^{-2}$, this effect can no longer be observed. There is even a slight tendency of increased peaking in the presence of central electron heating. In H-mode discharges, a flattening effect is reported for low densities, which vanishes when increasing the density to about $4.5 \cdot 10^{19}\, m^{-2}$. At high density ($7 - 8 \cdot 10^{19}\, m^{-2}$), there is a tendency of flattening again.
According to the detailed analysis presented in [16], those discharges that exhibit a density flattening are dominated by a TEM instability. In such case, the thermodiffusion coefficient C_T in equation (2.1) is large and has positive sign. For the discharges which did not show

density flattening, however, the most unstable mode was found to have an ITG character [16].
In [17], it is reported that in H-mode discharges also the opposite effect of ECRH, namely an increase of the density peaking, can occur under certain conditions. In general, density peaking in H-mode decreases with increasing collisionality, as figure 2.9 illustrates. If no stronger effect such as thermodiffusion is present, one expects that electron heating reduces the collisionality and thus increases the density peaking.

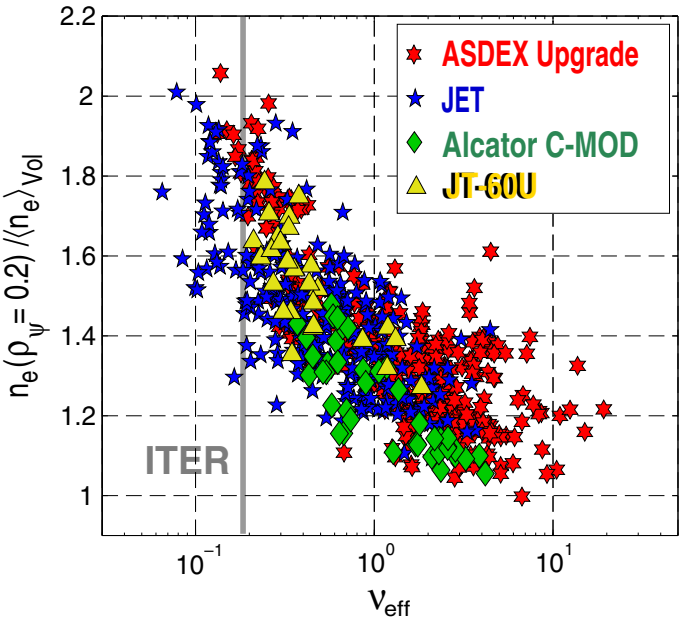

Figure 2.9: *Density peaking as a function of the effective collisionality* ν_{eff}. *[6]*

3 Experimental setup - The ASDEX Upgrade experiment

In this chapter, the important prerequisites for carrying out the experiments for this thesis will be presented. The vacuum vessel of a fusion experiment is usually surrounded by several additional heating systems and by a large number of plasma diagnostics. In the first section of this chapter, the machine characteristics of ASDEX Upgrade will be presented and the divertor concept with the resulting flux surface geometry will be introduced. The second section picks out one additional heating scheme that is relevant for density profile control, namely the electron cyclotron resonance heating, and the third and fourth section briefly introduce two diagnostics, the electron cyclotron emission radiometer and lithium beam impact excitation spectroscopy. The most important diagnostic for this study, however, which is the interferometer, deserves to be described in much more detail in an individual chapter.

3.1 ASDEX Upgrade - A divertor tokamak

The ASDEX Upgrade[1] experiment, on which the experimental studies for this thesis have been carried out, is located in Garching near Munich and started operation in the year 1991. With a major radius of 1.65 m and a minor radius of 0.5 m, ASDEX Upgrade has roughly half the size of JET. The name ASDEX stands for AxiSymmetric Divertor EXperiment and emphasizes the fact that this tokamak is equipped with a divertor. In contrast to the limiter configuration, where the last flux surface of the (usually circular) plasma touches a component of the vessel that is named 'limiter', the divertor configuration forms an X-point (see figure 3.1) by accordingly applying currents in vertical field coils outside the vessel. The flux surface which goes through the X-point is called separatrix, which is by definition the last closed flux surface. All flux surfaces inside it are closed, whereas the outer ones are open and intersect target plates in the lower part of the vessel, the so-called 'divertor'. The plasma region outside the separatrix is called the scrape-off layer. As the pressure along the field lines in the scrape-off layer is conserved, the particles that hit the divertor plates can have lower temperature, but higher density compared to those hitting the limiter. On the one hand, this reduces the erosion of the material and helps to significantly reduce the amount of impurity influx into the plasma, and on the other hand, it allows for efficient pumping of the exhausted particles after their neutralization

[1] Although the word 'Upgrade' may suggest that this was just an enhancement of the predecessor experiment ASDEX, it is in fact a completely new machine that does not share any components with the old experiment, which continued operation in China under the name HL-2A.

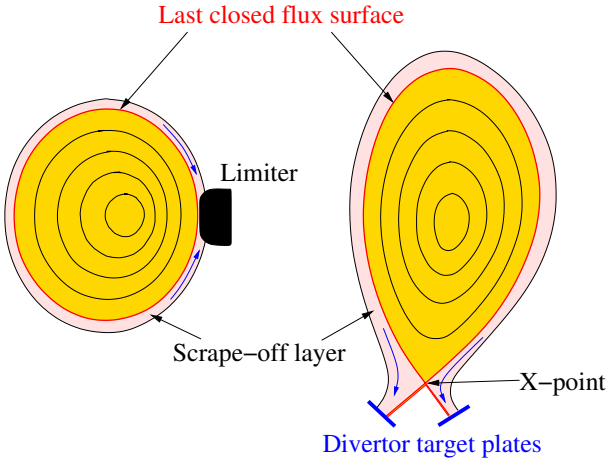

Figure 3.1: *Comparison of limiter configuration (left) and divertor configuration (right) [10].*

in the divertor. On the predecessor experiment ASDEX, the high-confinement mode (H-mode) was discovered, which is characterized by the occurrence of a transport barrier at the plasma edge and therefore provides an improved particle and energy confinement. Accordingly, plasma scenarios without this edge barrier are named low-confinement mode, or in short L-mode. A transition from L-mode to H-mode is characterized by an increase of the edge temperature and edge density and therefore by a flattening of the density profile. The condition for equilibrium in a tokamak is that the force due to the plasma pressure is balanced by the magnetic force, i.e.

$$\vec{\nabla} p \;=\; \vec{j} \times \vec{B}\,.$$

As the cross product $\vec{j} \times \vec{B}$ yields a vector that is perpendicular to $\vec{j}$ and $\vec{B}$, the pressure gradient is perpendicular to the magnetic field lines and to the current density vector and thus perpendicular to the magnetic flux surfaces. Accordingly, the pressure is constant on flux surfaces. From the above force balance equation, the so-called Grad-Shafranov equation can be derived, which is a differential equation for the poloidal flux function Ψ. This function is defined via

$$\frac{1}{R}\frac{\partial \Psi}{\partial R} = B_z \quad \text{and} \quad \frac{1}{R}\frac{\partial \Psi}{\partial z} = -B_R\,, \tag{3.1}$$

where R is the distance from the symmetry axis of the torus and z is a coordinate parallel to the symmetry axis. Evidently, the flux function Ψ defined like this, which is constant on flux surfaces, is arbitrary to an additive constant. A commonly used flux surface label is the normalized poloidal flux radius ρ_{pol}, which is defined via

$$\rho_{pol} \;=\; \sqrt{\frac{\Psi - \Psi_a}{\Psi_s - \Psi_a}}\,. \tag{3.2}$$

In this equation, Ψ_a is the value of the flux function at the magnetic axis and Ψ_s is its value at the separatrix. That way, we have $\rho_{pol} = 0$ in the plasma center, $\rho_{pol} = 1$ at the

separatrix and $\rho_{pol} > 1$ in the scrape-off layer.
By taking the measurements of magnetic pick-up coils, which are located on the inner vessel wall at different poloidal and toroidal positions, and solving the Grad-Shafranov equation, Ψ as a function of the geometric coordinates R and z can be reconstructed.
Especially for the characterization of magneto-hydrodynamic instabilities, the so-called safety factor q of a flux surface plays an important role, which is defined as

$$q = \frac{1}{2\pi} \oint \frac{1}{R} \frac{B_{toroidal}}{B_{poloidal}} ds \ ,$$

where integration is performed along the poloidal cross section of the flux surface. In simple words, the safety factor gives the number of turns in toroidal direction that a field line needs to perform one turn in poloidal direction. Instabilities can occur at locations in the plasma where the safety factor is a rational number, i.e. $q = m/n$ with small numbers $m, n \in \mathbb{N}$. This condition means that any field line on the flux surface is closed in itself after a very limited number of turns in the toroidal direction, which favors the occurrence of instabilities. An example of such an instability can be found in appendix A.1.

To achieve the high temperatures that are required for nuclear fusion, several heating schemes are applied on present-day experiments. As every tokamak is equipped with a central transformer coil that is used to inductively drive the plasma current, ohmic plasma heating is always possible. Due to the electric resistance of the plasma, the plasma current can only be maintained by continuously ramping the current in the transformer. As a result of the ohmic losses, power is deposited in the plasma. Ohmic heating is efficient at low plasma temperatures, where its electric resistance is high. With increasing temperature, however, the resistance decreases and ohmic heating becomes inefficient. For this reason, additional heating systems are required to obtain the desired temperatures. One method is neutral beam injection (NBI). This is basically a particle accelerator that produces a beam of hydrogen ions with a kinetic energy of 60-93 keV in case of ASDEX Upgrade. In a subsequent stage, this beam is neutralized and sent into the plasma vessel. When the energetic particles enter the plasma, they get ionized and deposit their kinetic energy in the plasma. With a total power of 20 MW, NBI is the main heating scheme on ASDEX Upgrade. The next section presents another heating scheme, which will be relevant for the control of density profile.

3.2 The electron cyclotron resonance heating (ECRH)

An alternative approach to plasma heating is the use of electromagnetic waves. When such a wave propagates through a plasma, its electric field accelerates the charged particles which can then heat the plasma via collisions. However, the collisional absorption is proportional to $T_e^{-3/2}$ [9], as the mean free path of the particles increases with increasing temperature. At temperatures relevant for fusion, waves of arbitrarily chosen frequency are therefore hardly absorbed in the plasma. But in a magnetized fusion plasma, resonant heating schemes can be successfully applied. The basic idea behind this is to send electromagnetic waves into the plasma whose frequency is equal to (or a multiple of) the gyro-frequency of plasma electrons or ions. That way, the particles can continuously gain energy with every gyration around the magnetic field lines. The matching condition for the frequency has two important consequences: On the one hand, the gyro-frequency is

different for electrons and ions, so each species requires an individual frequency and can therefore be heated individually. One distinguishes between the ion cyclotron resonance heating (ICRH) and the electron cyclotron resonance heating (ECRH). On the other hand, the gyro-frequency depends on the magnetic field strength, which is not constant over the plasma volume. That way, radio frequency heating allows for very localized energy deposition in the plasma. In the following, only the ECRH system will be discussed in detail, as this heating scheme is relevant for the control of the density profile.
For a magnetic flux density of 2.5 Tesla, the gyro-frequency of electrons is about 70 GHz. The electron cyclotron resonance heating therefore operates in the microwave range. The absorption of electromagnetic waves in a magnetized plasma is a complex issue. Absorption is also possible at higher harmonics of the gyro-frequency and depends on the polarization of the wave relatively to the magnetic field. The standard ECRH heating scheme on ASDEX Upgrade is second harmonic heating in extraordinary[2] polarization, which provides complete absorption of the microwave beam. As will be shown in section 4.3 of chapter 4, the propagation of microwaves in a typical ASDEX Upgrade plasma is nontrivial as beam refraction and possibly even reflection at the cut-off density can occur. These difficulties are the more severe the lower the frequency is, therefore, operating at 140 GHz is also preferable from this point of view.
The ASDEX Upgrade ECRH system operates at a standard frequency of 140 GHz produced by gyrotron tubes. A newer part of the system is also capable of operating at 105 GHz, but as those new gyrotrons were not available when the experiments for this thesis were carried out, only the old system is described here. It consists of four gyrotrons with a nominal output power of 500 kW each [18], which are grouped in two pairs. Each pair can only be switched on and of as a whole and must not exceed an on-time of 2 seconds per discharge. The microwaves are sent to the plasma vessel via waveguides, where an adjustable mirror acts as beam launcher. Power deposition occurs at the point where the microwave beam reaches the radius at which the magnetic field is in resonance, see figure 3.2. Due to refraction, the beam does not propagate along a straight line in the plasma in the general case, therefore, ray-tracing calculations are required to predict the location of power deposition.

3.3 The electron cyclotron emission (ECE) radiometer

The electron cyclotron emission radiometer allows for the measurement of the electron temperature of a fusion plasma. Its operating principle is in some sense just a reversal of the electron cyclotron resonance heating scheme, as it is based on the gyration of electrons around the field lines. Such a gyrating electron is an accelerated charge and therefore emits electromagnetic radiation at the cyclotron frequency and at its lower harmonics. As the cyclotron frequency depends on the strength of the magnetic field, which varies with the distance from the torus axis, frequency-selective radiometry of this emission allows for a spatially resolved measurement. If the plasma is optically thick for the wavelength under consideration, i.e. when absorption and re-emission of radiation is dominant compared to transmission through the plasma, which is fulfilled for the ECE frequency range in a tokamak in most cases, then the plasma behaves like a blackbody radiator and the intensity of this emission is a function of the electron temperature only, but not of the plasma density. That way, measuring the intensity of the electron cyclotron emission in a narrow frequency

[2] $\vec{E}_{wave} \perp \vec{B}_{toroidal}$

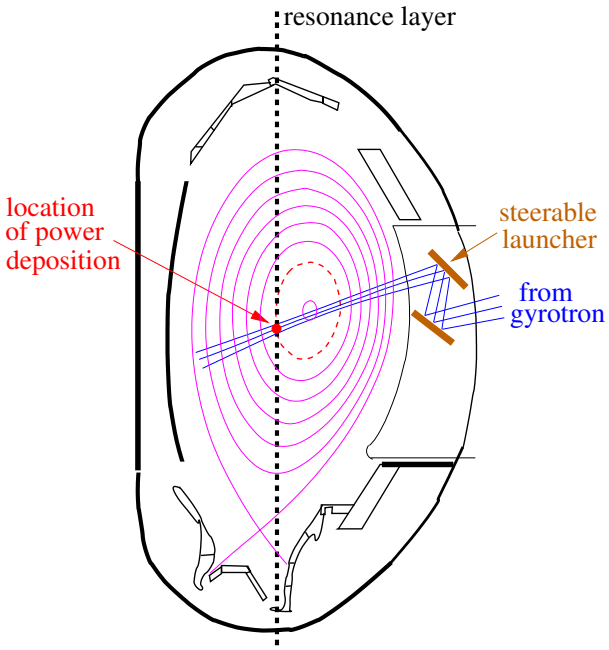

Figure 3.2: *Schematic drawing of the ECRH launcher and the Gaussian ECRH beam in the plasma. Power deposition occurs at the intersection of beam and resonance layer.*

window provides the electron temperature at the point where the line of sight of the antenna intersects the major radius at which the magnetic field strength is resonant for the chosen frequency. The ECE diagnostic on ASDEX Upgrade has a total of 60 channels [19] and thus provides a local temperature measurement at 60 different points in the plasma.

3.4 Lithium beam impact excitation spectroscopy

This diagnostic probes the plasma with a beam of neutral alkali atoms. For routine operation, lithium atoms are used. Despite of the fact that the diagnostic has been operated with the heavier alkali metal sodium in some cases, it will be referred to as 'lithium beam' diagnostic in the further discussion. With several lines of sight, the light emission along the beam is detected in a defined spectral range (usually the Li I line at 670.8 nm is chosen, corresponding to the $2p \rightarrow 2s$ transition of the Li atom). That way, it is possible to measure the local density of the first excited state of the lithium atom at the point where the line of sight intersects the trajectory of the particle beam. By solving a set of differential equations which describe the occupation numbers of the excited states of the lithium atom by taking into account processes such as charge exchange, ionization, excitation and de-excitation due to the interaction with the surrounding plasma, it is possible to calculate the local electron density and temperature. Due to beam attenuation, this measurement is restricted to the plasma edge. It only provides data on the scrape-off layer and the first few centimeters inside the separatrix.

4 Interferometric density measurement

There are several ways of measuring the density of a fusion plasma which have their specific advantages and disadvantages. For example, the use of Langmuir probes is restricted to the cold edge plasma. Also lithium beam impact excitation spectroscopy is limited to the edge region of the plasma, it can not measure far inside the separatrix. Detecting the plasma bremsstrahlung emission allows for density measurement, but requires knowledge of electron temperature and Z_{eff}. Thomson scattering provides a localized density measurement in any desired plasma region, but does not deliver results continuously as short laser pulses have to be sent into the plasma and the repetition rate of the lasers is limited.
Optical interferometry provides a line-integrated measurement of the electron density along a given line of sight through plasma, which is continuous, independent of other plasma parameters and rather accurate. For this reason, the density signals for feedback control are taken from the interferometer. First of all, the basics of light-plasma interaction will be discussed.

4.1 Optical properties of plasmas

The interaction between an electromagnetic wave, such as a laser beam, and the plasma can be described with the help of Maxwell's equations, which are given in SI units by:

$$\vec{\nabla} \cdot \vec{E} \;=\; \frac{\rho}{\epsilon_0} \tag{4.1}$$

$$\vec{\nabla} \cdot \vec{B} \;=\; 0 \tag{4.2}$$

$$\vec{\nabla} \times \vec{E} \;=\; -\frac{\partial \vec{B}}{\partial t} \tag{4.3}$$

$$\vec{\nabla} \times \vec{B} \;=\; \mu_0 \, \vec{j} \;+\; \frac{1}{c^2} \, \frac{\partial \vec{E}}{\partial t} \tag{4.4}$$

Taking the curl of the third equation, using the identity $\vec{\nabla} \times (\vec{\nabla} \times \vec{E}) \;=\; \vec{\nabla}(\vec{\nabla} \cdot \vec{E}) \;-\; \vec{\nabla}^2 \vec{E}$ on the left hand side and inserting the fourth equation on the right hand side yields:

$$\vec{\nabla}(\vec{\nabla} \cdot \vec{E}) \;-\; \vec{\nabla}^2 \vec{E} \;=\; -\mu_0 \, \frac{\partial \vec{j}}{\partial t} \;-\; \frac{1}{c^2} \, \frac{\partial^2 \vec{E}}{\partial t^2} \, .$$

The plasma can be described as a space that is homogeneously filled with ions and electrons whose electric charge just compensates, so the net charge vanishes on the scale length of interest, i.e. $\rho = 0$. Moreover, at the frequencies relevant for interferometry, the ions can be assumed to be fixed at their positions due to their large mass and resulting low mobility,

whereas the much lighter electrons move in the presence of an electric field that is caused by an electromagnetic wave propagating through the plasma. The field exerts the force $\vec{F} = -e\vec{E}$ on the electrons, resulting in an acceleration $\partial\vec{v}/\partial t = -e\vec{E}/m_e$, where e is the elementary charge and m_e the electron mass. The time derivative of the current density $\vec{j}$ is therefore given by $\frac{\partial\vec{j}}{\partial t} = \frac{\partial}{\partial t}(-e\, n_e\, \vec{v}) = \frac{e^2\, n_e}{m_e}\, \vec{E}$, where n_e is the number of electrons per volume. The previous equation can therefore be written as

$$-\vec{\nabla}^2\vec{E} = -\frac{\mu_0\, e^2\, n_e}{m_e}\, \vec{E} - \frac{1}{c^2}\, \frac{\partial^2\vec{E}}{\partial t^2}\,.$$

Inserting the ansatz $\vec{E}(\vec{x},t) = \vec{E}_0\, e^{i\,(\vec{k}\cdot\vec{x}\,-\,\omega t)}$ of a plane wave into this equation yields:

$$k^2 = -\frac{\mu_0\, e^2\, n_e}{m_e} + \frac{\omega^2}{c^2}\,.$$

As $\mu_0\epsilon_0 = 1/c^2$, the vacuum magnetic permeability μ_0 can be eliminated from this equation and the angular frequency ω of the electromagnetic wave can be written as

$$\omega = \sqrt{c^2\, k^2 + \frac{e^2\, n_e}{\epsilon_0\, m_e}}\,.$$

When the electrons in a plasma are displaced relatively to the ions, an electric field appears which causes a restoring force that acts on the electrons. The result is a harmonic oscillation of the electrons around their equilibrium position at the so-called plasma frequency $\omega_p = \sqrt{\frac{e^2 n_e}{\epsilon_0 m_e}}$. By introducing ω_p, the above equation can be simplified:

$$\omega = \sqrt{c^2\, k^2 + \omega_p^2}\,.$$

The phase velocity of an electromagnetic wave in a plasma is given by

$$v_{ph} = \frac{\omega}{k} = \frac{\omega}{\frac{1}{c}\sqrt{\omega^2 - \omega_p^2}} = \frac{c}{\sqrt{1 - \frac{\omega_p^2}{\omega^2}}}\,,$$

and the group velocity by the partial derivative

$$v_{gr} = \frac{\partial\omega}{\partial k} = \frac{c^2\, k}{\sqrt{c^2\, k^2 + \omega_p^2}} = c\sqrt{1 - \frac{\omega_p^2}{\omega^2}}\,.$$

The refractive index n of a plasma is defined via

$$n = \frac{c}{v_{ph}} = \sqrt{1 - \frac{\omega_p^2}{\omega^2}}\,,$$

which is less than 1. In this property, the optical behavior of a plasma differs from usual optical media like glass which have a refractive index $n > 1$. As a consequence of this, a typical fusion plasma with convex cross section has the effect of a dispersing lens on light (compare figure 4.1), in contrast to a glass lens with the same shape, which would act as a collecting lens. Optical density measurement is based on the above equation for the

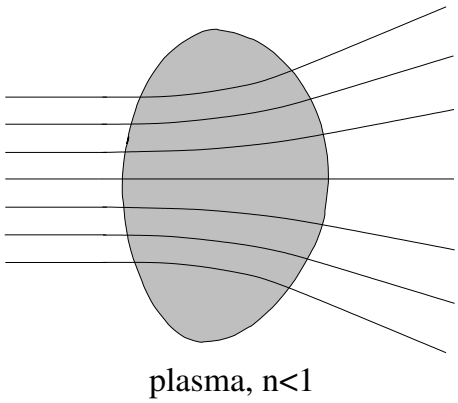

Figure 4.1: *Trajectory of light beams in a fusion plasma with convex shape. The illustration shows the separatrix section in a poloidal plane. The plasma is assumed to be inhomogeneous with high density in the center and low density at the edge, so refraction does not take place on the boundary only, but all over the plasma volume.*

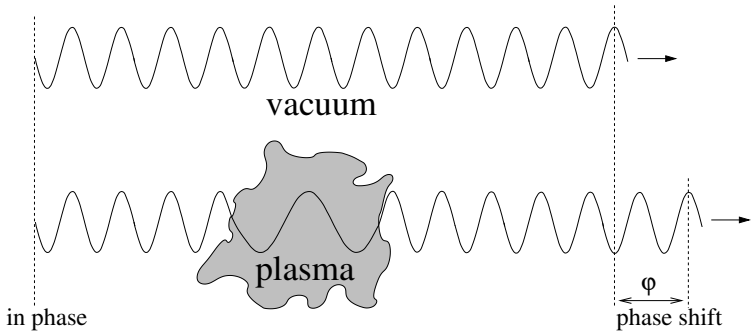

Figure 4.2: *The principle of plasma interferometry: For two infinitely long, continuous waves, 12 subsequent periods are shown. Both waves are in phase before one of them enters the plasma. The wavelength is greater in the plasma, therefore, the corresponding wave has leading phase after crossing the plasma.*

refractive index. A continuous wave (cw) laser is sent through the plasma. As the wavelength is greater in the plasma, the beam experiences a phase shift relatively to a beam that propagates in a vacuum, compare figure 4.2.
In the so-far discussion, no presence of an external magnetic field was assumed. For magnetically confined fusion plasmas, this assumption is not fulfilled. An external magnetic field changes the optical properties, as it makes the plasma birefringent. The above equation for the refractive index still holds for the case that the electric field vector of the wave is parallel to the external magnetic field, which is referred to as 'ordinary' polarization. This direction of polarization is chosen on the ASDEX Upgrade interferometer. For the extraordinary polarization ($\vec{E}_{wave} \perp \vec{B}_{toroidal}$), the refractive index is different as gyration of the electrons around the field lines plays a role. The birefringence of the plasma can be used for density measurement as well in so-called polarimeters. For example, such technique is used on JET [20]. However, as there is no polarimeter on ASDEX Upgrade, this will not be further discussed here.

4.2 The Mach-Zehnder-type heterodyne interferometer

If a laser beam passes through the plasma along a straight path of geometrical length L_{geom} and the electron density along this path depends on position and is given by $n_e(x)$, then the optical path length is

$$L_{opt} = \int_0^{L_{geom}} \frac{c}{v_{ph}(x)}\,dx = \int_0^{L_{geom}} \sqrt{1 - \frac{\omega_p^2(x)}{\omega^2}}\,dx = \int_0^{L_{geom}} \sqrt{1 - \frac{e^2\,n_e(x)}{\epsilon_0\,m_e\,\omega^2}}\,dx\,.$$

Using the Taylor series $\sqrt{1-x} = 1 - \frac{x}{2} + \mathcal{O}(x^2)$, which is appropriate as long as the angular frequency ω is much greater than the plasma frequency ω_p, this can be written as

$$L_{opt} = \int_0^{L_{geom}} \left(1 - n_e(x)\,\frac{e^2}{2\,\epsilon_0\,m_e\,\omega^2}\right) dx\,.$$

By introducing the classical electron radius[1] $r_e = \frac{e^2}{4\pi\,\epsilon_0\,m_e\,c^2} \approx 2.82 \cdot 10^{-15}\,\mathrm{m}$ and the vacuum wavelength $\lambda_0 = \frac{2\pi\,c}{\omega}$ of the laser, this result can finally be written as:

$$L_{opt} = L_{geom} - \frac{r_e\,\lambda_0^2}{2\pi} \int_0^{L_{geom}} n_e(x)\,dx \tag{4.5}$$

In principle, the line-integrated plasma electron density can be measured by sending a coherent light beam through the plasma and measuring its phase when it exits the plasma vessel. As the plasma density increases, the optical path through the plasma decreases according to equation (4.5) and the phase at the output changes.
If a laser beam is split and one component sent through the plasma and the other through a vacuum, then the two components have a phase shift φ afterwards that is given by:

$$\varphi = 2\pi\,\frac{L_{geom} - L_{opt}}{\lambda_0} = \lambda_0\,r_e \int_0^{L_{geom}} n_e(x)\,dx \tag{4.6}$$

This result means that the phase shift of the light beam due to the interaction with the plasma is proportional to λ_0. Therefore, especially lasers with long wavelength are suitable for density measurements. For wavelength selection, however, some further aspects have to be taken into account, which will be discussed later. Once the phase shift has been measured, the line-integrated electron density can be easily calculated without knowledge of any other plasma parameter.
Like on most other fusion experiments, a Mach-Zehnder type interferometer is used on ASDEX Upgrade to measure the phase shift which the light beam experiences when passing through the plasma. The basic principle of this type of interferometer is illustrated in figure 4.3. A laser beam is split into three components, using two beam splitters. One beam passes through the plasma (probe beam), the second acts as a reference beam and propagates outside the plasma vessel. The desired density information can be obtained from the phase

[1] r_e is defined as the radius of a sphere capacitor whose electrostatic energy $E = \frac{1}{2}\,Q^2/C$ is equal to the half rest energy of an electron when it carries one elementary charge, i.e. $Q = e$.

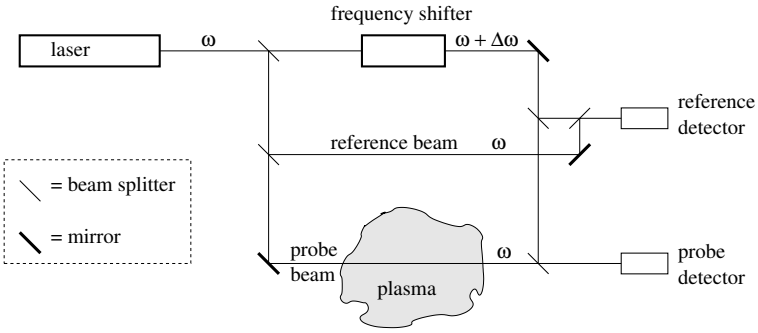

Figure 4.3: *Schematic diagram of the Mach-Zehnder interferometer [9].*

difference between probe and reference beam. However, as optical frequencies are of the order of $10^{12} - 10^{14}$ Hz, there is no detector available that can resolve the oscillation of the electric field, so it is not possible to send both beams to detectors and measure the phase difference of their output signals. This problem is solved via the heterodyne principle. The frequency of the third beam is slightly shifted by $\Delta\omega$. After that, the beam is split and combined with the probe and reference beams. Superposition of two light waves with frequencies ω and $\omega + \Delta\omega$ results in a beat signal:

$$\sin(\omega t) + \sin((\omega + \Delta\omega) t) = 2 \cdot \sin\left(\frac{2\omega + \Delta\omega}{2} t\right) \cdot \cos\left(\frac{\Delta\omega}{2} t\right) \tag{4.7}$$

This signal can be characterized as a fast oscillation whose amplitude slowly increases and decreases, following the cosine envelope function. The detector is insensitive to the fast optical frequency $(2\omega + \Delta\omega)/2$, but can detect the slow modulation of the signal. Although the argument of the cosine contains the angular frequency $\Delta\omega/2$, a $\Delta\omega$ beat signal will appear at the output of the detector, as the detected intensity is proportional to the square of the amplitude and $(\cos x)^2$ is a function with 1π-periodicity. If this situation is true for the reference beam, the detector for the probe beam (that has an additional phase φ), will receive the beat signal

$$\sin(\omega t + \varphi) + \sin((\omega + \Delta\omega) t) = 2 \cdot \sin\left(\frac{2\omega + \Delta\omega}{2} t + \frac{\varphi}{2}\right) \cdot \cos\left(\frac{\Delta\omega}{2} t - \frac{\varphi}{2}\right) . \tag{4.8}$$

Evidently, the phase shift φ of the probe beam becomes manifest in a phase shift $\varphi/2$ in the argument of the low-frequency envelope function of the beat signal (see figure 4.4). Comparing the phase of the two beat signals at the output of the two detectors allows for plasma density determination. One has to be aware of the minus sign in the argument of the cosine on the right hand side: Increasing plasma density results in a leading phase of the probing beam, but assuming a positive frequency shift $\Delta\omega$ (i.e. a 'blue-shift'), the situation is just the other way round for the beat signals. There, the probing signal is delayed relatively to the reference signal when plasma density increases.
The calculations so far are based on the assumption that the combined beams have the same amplitude. In practice, this assumption is usually not fulfilled. If there are different amplitudes A_1 and A_2, the result is

$$A_1 \cdot \sin(\omega t + \varphi) + A_2 \cdot \sin((\omega + \Delta\omega) t) = (A_1 - A_2) \cdot \sin(\omega t + \varphi) +$$

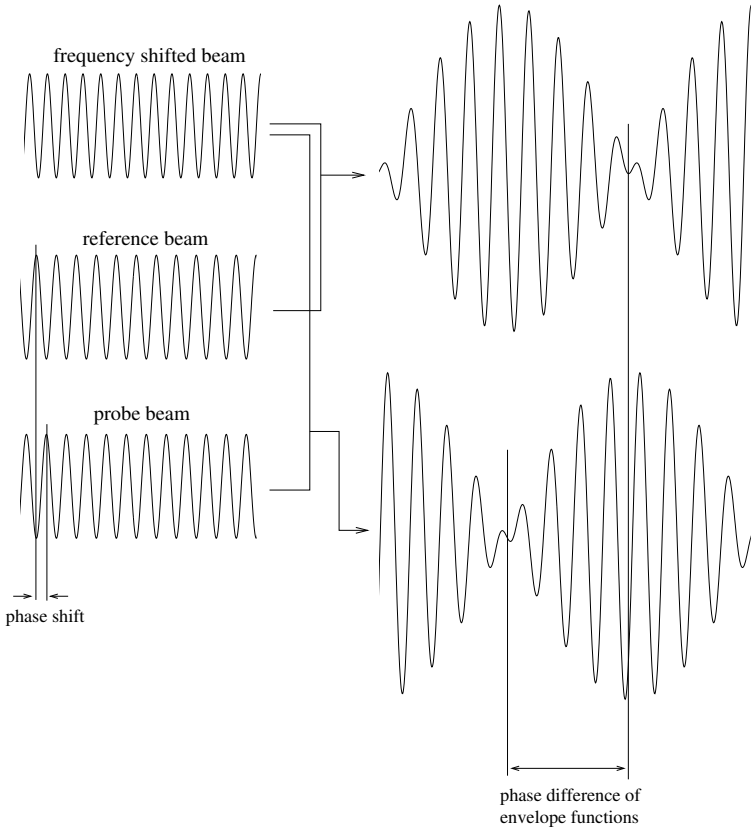

Figure 4.4: *Illustration of the heterodyne principle.*

$$+ 2A_2 \cdot \sin\left(\frac{2\omega + \Delta\omega}{2}t + \frac{\varphi}{2}\right) \cdot \cos\left(\frac{\Delta\omega}{2}t - \frac{\varphi}{2}\right) , \tag{4.9}$$

which means that an additional term at the optical frequency appears. At the output of the detector, this just causes a constant offset voltage but does not affect the detection of the phase shift of the beat signal.
Already at this point, a principal weakness of the interferometry method becomes apparent: Due to the π-periodicity of the function $(\cos\ x)^2$, there is no way to distinguish a phase difference $\varphi + n \cdot 2\pi$, $n \in \mathbb{Z}$ from a phase difference φ. So the line-integrated electron density measured this way is arbitrary to an integer multiple of $n_{e\,2\pi}$ (the amount of density that corresponds to a phase shift of the probe beam of 2π). This ambiguity becomes relevant when the laser wavelength is chosen in a way that typical line-integrated electron densities in the fusion device are greater than $n_{e\,2\pi}$. This difficulty can be overcome by using a multiradian phase detection system as long as the measurement starts with the tokamak evacuated (i.e. at zero electron density) and all changes of density occur sufficiently slowly so that all transitions from one period of the beat signal to the next can be counted. This makes an interferometric density measurement history-dependent, as the true density can be provided only when the density evolution has been continuously monitored since the beginning of the plasma discharge. If a rapid density change cannot be followed due to lim-

ited time resolution of the readout electronics, if electric noise disturbs the readout system or if the signal is temporarily lost due to beam deflection in the plasma, the measurement only provides electron density information modulo $n_{e\,2\pi}$, which is in general not useful, especially for real-time control. If the calculated density suddenly becomes affected by an error that is a multiple of $n_{e\,2\pi}$, this is often referred to as a "fringe jump". The use of this expression has historic reasons, it originates from a time when first fusion devices were built and plasma density was measured by counting interference fringes manually. Since these days, the "fringe" has often been used as a unit for plasma density that can also be found in the literature. If the measured density does not return to zero, but to a (positive or negative) multiple of $n_{e\,2\pi}$ after the plasma discharge, this is evidence for the occurrence of (at least one) fringe jump.

As interferometric measurements require a long coherence length of the light beam, a laser is required as the light source. Moreover, one beam component has to be shifted in its frequency by a small amount $\Delta\omega$ in order to apply the heterodyne principle. Shifting the frequency afterwards could be avoided by using two lasers with slightly different cavity length that emit radiation with slightly different frequency, compare reference [21]. However, on ASDEX Upgrade a single laser in combination with an adjustable external frequency shifter is used. All frequency shift systems are based on the Doppler effect, whereby the laser beam is reflected off or diffracted on a moving mirror or grating respectively. There are two different techniques for frequency shifting. One type is a blazed optical grating, which is bent and covers the outer surface of a rotating cylindrical disc [22]. When the

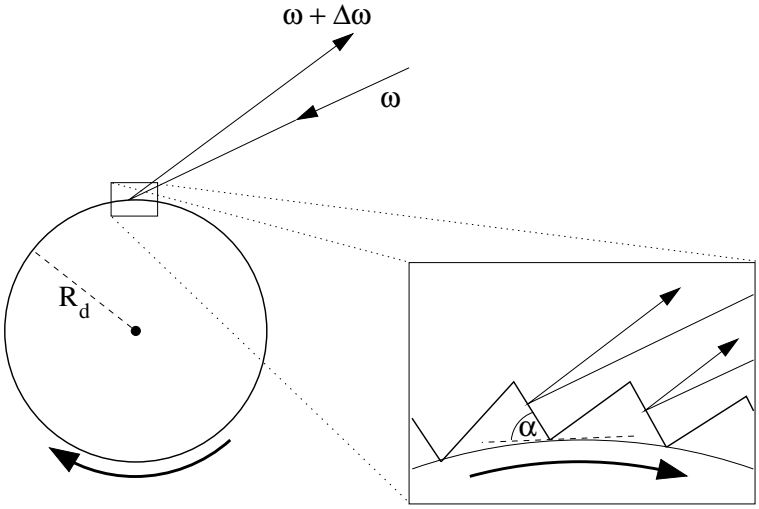

Figure 4.5: *Frequency shift of laser light using a rotating grating.*

laser is focused on the blazed grating on the rotating disc, the photons are reflected from the mirrored surface which has a fixed velocity

$$v = 2\pi\, R_d\, F_d\, \sin\alpha\,,$$

where α is the blaze angle, R_d the radius of the disc (see figure 4.5) and F_d the number of turns per second of the disc. The frequency ω‘ of the reflected light is given by

$$\omega' = \omega \cdot \sqrt{\frac{c + 2\,v}{c - 2\,v}}\,,$$

where ω is the incoming laser frequency. First order Taylor expansion yields

$$\Delta\omega \;=\; \omega' - \omega = \omega \;\frac{4\pi\; R_d\; F_d\; \sin\alpha}{c}\;. \tag{4.10}$$

Hence the frequency shift $\Delta\omega$ is proportional to the rotational speed of the disc and thus can be altered easily. Due to the presence of strong magnetic fields around the torus, no electric motor can be used to drive the grating on ASDEX Upgrade. Instead, a pneumatically driven motor is used whose speed of rotation is controlled via an adjustable valve in the gas supply line.
The other technique for frequency shifting is an acousto-optic modulator (AOM), which is described in appendix A.2.

4.3 Wavelength selection for fusion plasma interferometry

As the phase shift φ that a beam experiences when passing through a plasma is proportional to λ, it is desirable to use long wavelengths in order to obtain good density resolution with a given phase resolution of the detection system. However, there are upper limits to the probing wavelength. On the one hand, the angular frequency $\omega = \frac{2\pi c}{\lambda}$ of the electromagnetic wave must not be lower than the electron plasma frequency $\omega_p = \sqrt{\frac{n_e e^2}{\epsilon_0 m_e}}$ as otherwise, the wave could not propagate through the plasma, but would be reflected. On the other hand, one has to take beam deflection into account. As a fusion plasma is an inhomogeneous optical medium with high electron density in the center and low density at the edge, a laser beam will be deflected as illustrated in figure 4.1. From the eiconal equation in geometrical optics, the so-called ray equation can be derived:

$$\frac{d}{ds}\left[n \cdot \frac{d\vec{r}}{ds}\right] \;=\; \vec{\nabla} n$$

This equation describes the propagation of light in inhomogeneous optical media, where $r:\ [0;L] \longrightarrow \mathbb{R}^3\ ,\quad s \longmapsto \vec{r}(s)$ is a path in the 3-dimensional space which describes the beam path and is parameterized by the path length. The latter condition means that the geometrical length along the path between two points $\vec{r}(s)$ and $\vec{r}(s+\Delta s)$ is given by Δs. This is equivalent to

$$\left|\frac{d\vec{r}(s)}{ds}\right| = 1\ ,$$

which means that the tangential vector that is obtained by differentiating $\vec{r}(s)$ with respect to s always has the absolute value 1, i.e. is a unit vector. The scalar field $n:\mathbb{R}^3 \longrightarrow \mathbb{R}\ ,\quad \vec{r} \longmapsto n(\vec{r})$ describes the local refractive index of the medium. As we have identified the expression $\frac{d\vec{r}(s)}{ds}$ as the unit vector along the direction of light propagation at the point $\vec{r}(s)$, the ray equation can be described in words as follows:
The change of the product 'local refractive index times unit vector of beam direction' is given by the gradient of the refractive index. So the light beam is deflected towards increasing optical density.
For a given distribution of the refractive index $n(\vec{r})$, the ray equation is a differential equation that is fulfilled by the actual beam trajectory $\vec{r}(s)$. Solving this equation can be rather difficult, especially for the plasma density distribution in a tokamak. To illustrate the λ dependence of the deflection angle, the simple example presented in figure 4.6 can be

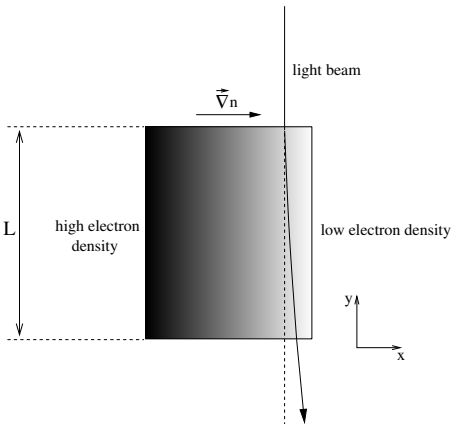

Figure 4.6: *Simple example of light deflection in a plasma with one-dimensional density gradient.*

used. A light beam enters a plasma-filled volume perpendicular to the density gradient. The deflection will be assumed to be so small that the density gradient is still perpendicular to the direction of beam propagation in good approximation when the beam leaves the volume after a distance L. The unit vector along the direction of beam propagation will be labeled $\vec{e}_i$ before the beam enters the plasma and $\vec{e}_f$ afterwards. With the approximations made and for refractive indices close to 1, the ray equation can be integrated, resulting in

$$\vec{e}_f \; - \; \vec{e}_i \; \approx \; \int_0^L \vec{\nabla} n \, ds \; = \; L \frac{\partial n}{\partial x} \vec{e}_x \; .$$

In case of a linear electron density gradient in the x-direction, i.e. $n_e(x) = -K \cdot x$, and with the Taylor approximation $n \approx 1 - n_e \frac{e^2}{2\,\epsilon_0\, m_e\, \omega^2}$ that was made previously, the deflection angle is approximately given by

$$\alpha \approx L \cdot K \frac{e^2}{2\,\epsilon_0\, m_e\, \omega^2} = L \cdot K \frac{e^2}{8\pi^2\, \epsilon_0\, m_e\, c^2}\, \lambda^2 \; = \; \frac{LKr_e}{2\pi}\, \lambda^2 \; .$$

This is just a crude approximation for a simple geometry, a more detailed discussion for tokamak-relevant density distributions can for example be found in [23]. However, it can be seen that the beam deflection effect is proportional to the square of the wavelength. Due to the limited diameter of vessel ports and detectors, deflection can result in signal loss. Therefore, this also sets an upper limit to the probing wavelength which is usually more restrictive than the limit due to the plasma frequency. For small fusion experiments with minor plasma radii of the order of 10 cm, microwaves are suitable for interferometry. With growing size of the fusion experiment, however, the maximum tolerable angle of beam deflection decreases, as the size of the diagnostic ports and the sensitive area of the detectors usually remains constant, whereas the path length of the beam inside the plasma vessel grows. On larger experiments like ASDEX Upgrade or JET, the longest wavelength that can be used is in the sub-millimeter region. On next-step devices like ITER, infrared light will have to be used.
Whereas for interferometry, a wavelength can be chosen at which beam deflection is not critical, the electron cyclotron resonance heating has to operate in the microwave range

as the wave frequency is determined by the gyro-frequency of the electrons. Therefore, the heating beam suffers from significant deflection in the plasma and so-called ray-tracing codes have to be used to predict the location of power deposition. They calculate the trajectory of the heating beam in the fusion plasma with its inhomogeneous density by numerically solving equations like the previously introduced ray equation.

As discussed, problems due to beam refraction in interferometry can be avoided by going towards shorter wavelengths, however, the price paid for this is an increased sensitivity to mechanical vibrations. Whereas the phase shift due to the interaction with the plasma electrons is proportional to λ, a change ΔL of the geometric path length will result in a phase shift of $2\pi\Delta L/\lambda$, i.e. is proportional to $1/\lambda$. When going towards shorter wavelengths, the mechanical effects become dominant at a certain point. Despite of possible efforts towards mechanical decoupling of the interferometer from the plasma vessel, a vibration level of the order of several micrometers can hardly be avoided. For this reason, a compensation interferometer that operates at two different wavelengths simultaneously along a given line of sight has to be used in case of short probing wavelengths. Then, there are two phase shifts measured, and two unknown parameters (plasma density and mechanic path variation ΔL), so the problem can be analytically solved. This is discussed in more detail in appendix A.2.

The problem of fringe jumps is in general more significant for long wavelengths. For short wavelengths, the maximum plasma density achieved in the experiment can cause a phase shift of the probing beam of less than 2π. A fringe jump will then result in a measured density that is either negative or extremely high, so the error is evident and can be corrected easily.
The following table summarizes the specific advantages and disadvantages of different wavelength regions for a fusion device with the dimensions of ASDEX Upgrade, i.e. with chord lengths through the plasma of the order of 1 meter and line-integrated electron densities up to about $10^{20}\,m^{-2}$. For the calculation of the lateral deflection, a linear decay of density from the plasma core to the edge was assumed.

	microwaves	sub-millimeter waves	infrared light	visible light
typical wavelength	several mm	100-350 μm	10 μm	400-800 nm
max. φ in plasma	200 fringes	20 fringes	1 fringe	0.05 fringes
φ due to $\Delta L = 10\,\mu$m	0.002 fringes	0.05 fringes	1 fringe	20 fringes
lateral deflection	50 cm	5 mm	10 μm	50 nm
useful for density measurement	no (deflection)	yes	yes	no (small φ)
need for compensation wavelength	-	no	yes	-

As one can see, microwaves are not suitable due to strong deflection. Either an interferometer with sub-millimeter waves can be used, or a far-infrared interferometer with a second wavelength for vibration compensation. As the following chapter will illustrate, both systems are in use on ASDEX Upgrade.

4.4 The interferometer setup on ASDEX Upgrade

The ASDEX Upgrade interferometer has 5 horizontal and 3 vertical channels (see figure 4.7). Three of the horizontal channels, which are labeled as H1 - H3, are parallel to the

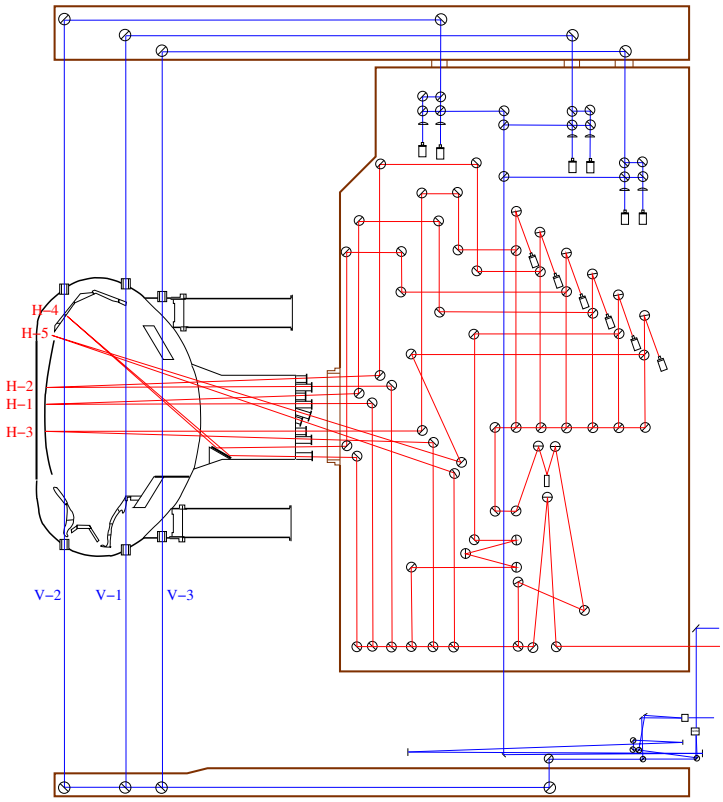

Figure 4.7: *The 5 horizontal and 3 vertical lines of sight of the ASDEX Upgrade interferometer. The drawing shows a cross section of the torus and the interferometer C-frame. Beam trajectories belonging to the DCN system are drawn in red, and those of the $CO_2/HeNe$ system in blue. The DCN channels are labeled H-1 to H-5 and the $CO_2/HeNe$ channels V-1 to V-3.*

midplane of the torus, whereas the lines of sight of H4 and H5 cross the plasma in a sloped way. As discussed before, sub-millimeter waves and far-infrared light are appropriate for interferometry on a tokamak of the size of ASDEX Upgrade. The advantage of sub-millimeter waves is the weak influence of mechanical vibrations, so no second wavelength for compensation has to be installed. The beam deflection due to density gradients in the plasma is still less than 1 cm according to the crude estimation made in the previous chapter, where a linear density gradient from the plasma center to the edge was assumed. In practice, local density gradients can be stronger and deflection by several cm is possible. As the optical path from the laser to the detectors is of the order of several 10 meters, small beam divergence is essential. The divergence of a Gaussian beam is defined as the half opening angle and given by

$$\Theta = \frac{\lambda}{\pi w_0} ,$$

where w_0 is the Gaussian beam waist. In order to have a divergence in the milliradian range, the waist of a sub-millimeter beam has to be of the order of a few centimeters. The deflection of the beam is therefore of the order of its lateral dimension and enough power will reach the detectors in most cases.
In the past, only one single sub-millimeter wavelength has been used for both, horizontal and vertical channels. Meanwhile, there are different systems: A DCN interferometer with five horizontal channels, and a vertical two-color $CO_2/HeNe$ interferometer with 3 lines of sight. As the calculation of density profiles within this thesis work will only rely on the measurements of the DCN interferometer, only this system is discussed in detail here. A detailed discussion of the $CO_2/HeNe$ interferometer can be found in appendix A.2. At the end of this chapter, just the basic properties of the $CO_2/HeNe$ system are briefly summarized.

For the horizontal lines of sight, a deuterium cyanide laser is used as the light source. This is a very rare type of terahertz laser whose main application is the use on fusion devices. The active medium of this laser is the deuterated prussic acid molecule (DCN) in gaseous state. Laser emission is a result of transitions between rotational and vibrational states of the DCN molecule. Figure 4.8 shows an energy level diagram, where the transition wavelengths $\lambda_1, \lambda_2, \lambda_3$ and λ_4 are 189.95, 190.01, 194.70 and 194.76 μm [24]. In this level diagram, J denotes the rotational quantum number and the other 3 figures are the vibrational quantum numbers. Figure 4.8 also illustrates the 3 corresponding vibrational states of the linear DCN molecule. Actually, there are four vibrational degrees of freedom as the molecule can perform two different, but degenerated bending oscillations. Only one of them is shown in the figure, for the other one, the atoms would oscillate perpendicular to the drawing plane. A linear combination of these two bending oscillations with some phase shift can result in an angular momentum with respect to the molecule axis. The superscript next to the second quantum number denotes this angular momentum in units of $\hbar$.

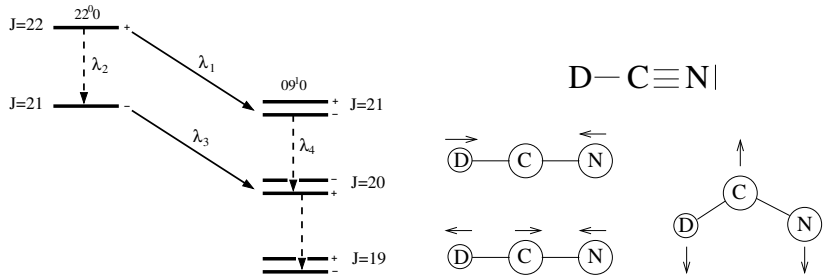

Figure 4.8: *Energy level scheme (from [24], left) and vibrational states of the DCN molecule (right).*

The laser is located outside the biological shield around the experiment to allow for access for maintenance at any time. It consists of a 3 meter long glass tube that is kept at a constant temperature of 130 degree centigrade. This is achieved by putting the laser tube concentrically into a second, larger glass tube and flushing the space in between with accordingly heated silicone oil. Inside the laser tube, a gas discharge in a nitrogen/helium gas mixture at a pressure of a few millibar is ignited by applying a DC voltage of typically 3 kV. In this state, the system does not yet emit laser radiation. Only about 1 minute before an

ASDEX Upgrade discharge starts, deuterated methane gas (CD_4) is added and allows for the production of DCN molecules. As CD_4 is very expensive and causes carbon deposition inside the laser tube, the use of CD_4 is restricted to a short time interval. Nevertheless, when some hundred minutes of operation with CD_4 have been accumulated, it is necessary to open the laser tube and remove the carbon layers that mainly deposit around the electrodes. Due to this property, DCN lasers are only useful for short-pulse experiments and very unlikely to be used on next-step fusion devices or power plants. Sustaining the gas discharge in N_2/He between plasma discharges is necessary to keep the laser in thermal equilibrium. The length of the resonator is stabilized by 3 long quartz rods with central borehole through which cooling water is pumped in order to keep the quartz material at constant temperature. At the one end of the laser tube, there is a metallic mirror which can be moved with an electric motor and a micrometer screw, allowing for an adjustment of the resonator length. At the output side of the laser, there is a quartz plate on which a

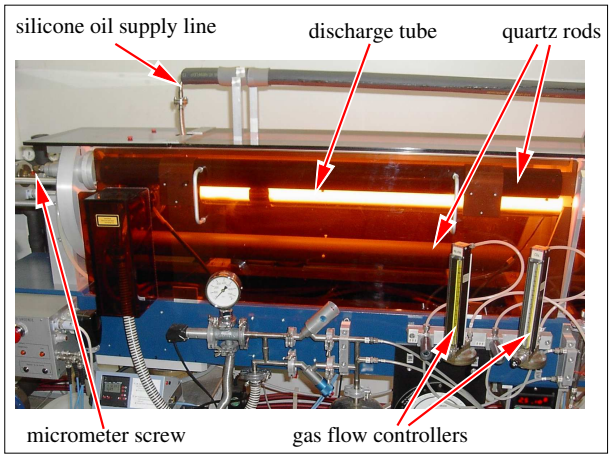

Figure 4.9: *A photograph of the DCN laser in operation. There are two gas supply lines for He/N_2 and CD_4. The latter can be opened and closed by a solenoid valve.*

strip grating has been deposited. It does not only act as a semi-transparent output coupler mirror, but also defines the direction of polarization of the laser beam. In order to remotely monitor the laser output power, the beam is first sent to a beam splitter with about 99% of transmission. The split off component with about 1% of intensity goes through a mechanical chopper and then to a pyroelectric detector. The remaining laser beam enters the torus hall via a transmission line and is finally split inside the interferometer box. One component is frequency-shifted by a rotating grating, the other not. Both beams are then split into 6 components each, one of them acts as reference beam. The other 5 components of the unshifted beam enter the plasma vessel and cross the plasma along different chords (see figure 4.7). As all the space inside the inner column of the tokamak is required for the transformer, there is no space left for optical components. Therefore, mirrors are attached to the inner wall of the plasma vessel (compare figure 4.10) so that the beams are reflected, cross the plasma again and leave the vessel at the outer side. Each beam is then combined with a frequency-shifted beam component in a beam-splitter and sent to a pyroelectric detector. The same is done with the reference beam. The entire interferometer system is continuously flushed with dry air, as air humidity strongly absorbs electromagnetic radiation in the sub-millimeter wavelength range.

Figure 4.10: *A photograph of an in-vessel mirror at the inner column of the ASDEX Upgrade plasma vessel. The diameter of the mirror is about 5 cm. It is surrounded by the tungsten-coated first wall carbon tiles.*

Once the phase shift φ_{DCN} has been measured, the line-integrated electron density can be calculated via

$$\int n_e(x)\,dx \;=\; \frac{\varphi_{DCN}}{2 \cdot 195\,\mu m \cdot 2.82 \cdot 10^{-15}\,m} \;=\; \frac{\varphi_{DCN}}{2\pi} \cdot 0.572 \cdot 10^{19}\,\frac{e^-}{m^2}\,.$$

The factor '2' in the denominator is due to the fact that the beam crosses the plasma twice. The wavelength that is used for density measurement is 195 μm and accordingly, a phase shift of 2π corresponds to $0.572 \cdot 10^{19}\frac{e^-}{m^2}$, which is referred to as one 'fringe'. The 190 μm radiation that is potentially emitted by the laser is suppressed by the subsequent optical components in the beam path [25]. The beam splitters in the DCN interferometer of ASDEX Upgrade are planar quartz plates that are mounted at an angle of 45 degree and act like a Fabry-Perot etalon. Their thickness has been calculated to provide the desired intensity ratio of transmitted and reflected beam at a wavelength of 195 μm.
The readout electronics for the DCN system is described in a separate chapter. As the development of a new generation of phase counters is a major part of this thesis, the properties of the previous readout hardware deserve to be discussed in much detail in the next chapter.

The vertical $CO_2/HeNe$ interferometer is described in detail in appendix A.2. It has 3 lines of sight, which are labeled V-1, V-2 and V-3 (see figure 4.7). However, not more than two of them can be operated simultaneously. Either channels V-1 and V-2 are active, or only channel V-3. The big advantage of the $CO_2/HeNe$ interferometer compared to the DCN system is its insensitivity to strong density gradients in the plasma, as beam refraction does not play a role at the given wavelengths. In addition, it provides a higher temporal resolution. However, its main disadvantage is the high noise level of the output signals, and the low number of lines of sight. Therefore, the measurements by the DCN interferometer are usually preferred whenever they are available. The limitations of the DCN system are illustrated in the next chapter.

5 Development of new readout electronics for the DCN system

As discussed in the previous chapter, the plasma densities that are achieved on ASDEX Upgrade correspond to a phase shift of up to $20 \times 2\pi$ for the DCN system. This makes interferometry history-dependent, as only the phase shift modulo 2π can be measured at any time, but not the integer multiples of 2π. In some situations, counting errors, so-called 'fringe jumps', can occur. This results in incorrect density signals and also affects all data that is calculated from the line-integrated densities, such as density profiles. In addition, all feedback control algorithms that use the plasma density as input are endangered to send inadequate commands to the actuators. For offline analysis, the measured density time traces can be viewed and corrected manually, if required. However, as the focus of this work is on real-time calculation of density profiles and their use in feedback control, it was important to find a fully automatic protection mechanism against fringe jumps. This was achieved by an upgrade of the interferometer readout electronics. First of all, the previously existing readout system and its properties will be described. After this, the design of the new electronics and the experimental results will be presented.

5.1 Status before the upgrade

5.1.1 The old readout electronics

In the interferometer frame in the torus hall, there are 6 pyroelectric detectors for the DCN wavelength, one of them detecting the reference beam, and five of them the probe beams that correspond to the 5 lines of sight (compare figure 4.7 in section 4.4). The detector signals are pre-amplified in the torus hall and then sent to the readout system in the control room via coaxial cables. The beat signal frequency is determined by the angular frequency of the rotating grating, which can be controlled by adjusting the pressure air flow rate to the pneumatic motor that drives the grating. The frequency is usually set to about 10 kHz, whereby a certain amount of fluctuation is unavoidable as the frequency is determined by a mechanical system. Also operation at 20 kHz is possible, but not done very often as this results in increased wear of the bearings of the grating. In the control room, the signals go through accordingly adjusted bandpass filters first in order to reject lower and higher frequency noise. The passband for the reference signal is narrow (about ± 1 kHz), as its frequency is strictly proportional to the angular velocity of the grating, whereas a much larger bandwidth has to be allowed for the probing signals as any change of the phase temporarily compresses or expands the wave train and therefore corresponds to a temporary frequency shift. Phase comparison is finally done by 5 multiradian phase

counter modules which are based on the principle that was proposed in [26]. Each module receives the reference signal and one of the probing signals. Inside these modules, there is a transformer and some additional circuitry for galvanic isolation, as well as a further bandpass filter and amplifier. Then, a comparator transforms the almost sinusoidal analog plasma and reference signals into TTL compatible digital signals. The subsequent digital circuit involves a phase-locked loop (PLL), the modules will therefore be referred to as 'DCNPLL' modules in the further discussion. A schematic drawing of the circuit is shown in figure 5.1. A phase comparator and a voltage controlled oscillator, which are both located

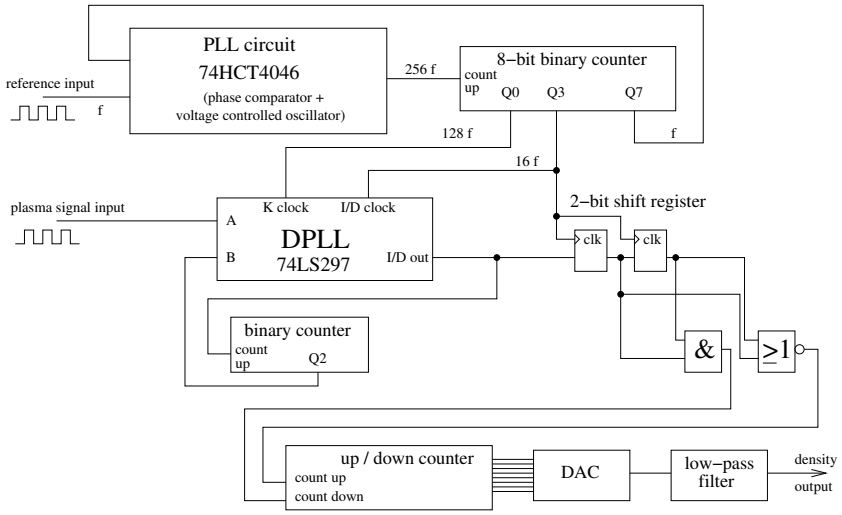

Figure 5.1: *Schematic drawing of the digital part of the DCNPLL modules. [26]*

inside a 74HCT4046 IC, are used to generate a square wave signal that has 256 times the frequency of the reference signal. An 8-bit counter that is used for frequency division and the phase comparator circuit guarantee that both signals are strictly in phase, i.e. each 256^{th} rising edge of the square wave signal exactly coincides with the rising edge of the reference signal. From the corresponding terminals of the 8-bit counter, signals can be obtained that have 128 and 16 times the frequency of the reference signal. A digital phase locked loop circuit (type 74LS297) is supplied with these two frequencies and with the plasma signal. This circuit produces an output signal (I/D out) that has eight times the frequency of the reference signal and whose phase is kept constant relatively to the plasma signal. If the phase of the plasma signal drifts due to density changes, this is achieved by either adding or omitting pulses in the I/D out signal (see figure 5.2). Two subsequent states of the I/D out signal are stored in a 2-bit shift register. If density is constant, there is a strict alternation of 'low' and 'high' states. However, if density decreases, there are two subsequent 'high' states, and if it increases, there are two 'low' states. An AND and a NOR gate are used to detect these two situations, their output causes a binary counter to count down or up. The counter reading is sent to a digital-to-analog-converter (DAC) that produces an analog density signal. A subsequent 4 kHz low-pass filter rejects noise from the digital side of the DAC which would otherwise be present in the output signal. The phase resolution of this circuit is 1/16 fringe.
As mentioned earlier, for the DCN wavelength of 195 μm beam deflection by strong local density gradients in the plasma is a critical issue. If deflection becomes larger than the beam

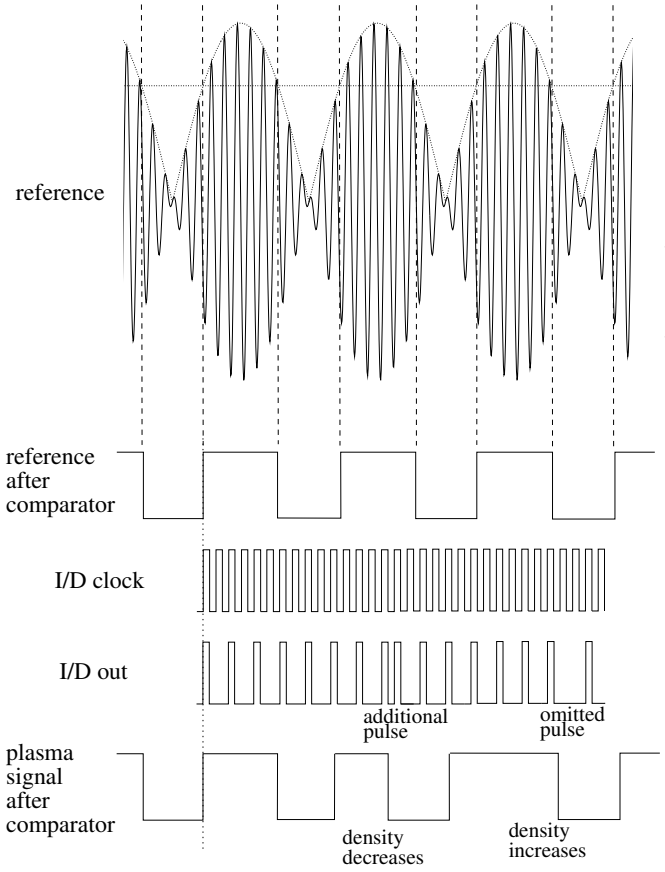

Figure 5.2: *Principle of the DCNPLL modules: An optical beat signal reaches the detector, which, however, is not sensitive to fast optical oscillations of the order of* 10^{12} *Hz. Only the slow variation of the envelope function (illustrated by the dotted* $|\cos(\Delta\omega\, t/2)|$ *function) is detected. After the comparator, there is a TTL signal whose 'high' periods coincide with the beat pulses. The I/D clock signal has 16 times the beat frequency (not so in the drawing, for convenience), the I/D out signal 8 times. The latter has a 1/4 duty cycle. If plasma density decreases, the probing signal is compressed, if it increases, the signal is expanded (It is just the other way round for the light wave itself, but the minus sign in front of* $\varphi/2$ *on the right hand side of equation (4.8) reverses the situation for the beat signal). The DPLL circuit accounts for this by inserting an additional pulse or omitting one, respectively.*

waist, the power arriving at the detector may drop so far that the probe signal after the comparator is just constant. Such signal loss would cause the PLL circuit to permanently insert or omit pulses and as a consequence, the counter to count down or up very quickly, which means that the analog density output signal would drift away rapidly. To avoid such extreme behavior, additional circuitry has been implemented that automatically detects a loss of the plasma signal and locks the counter. When the signal returns, the counter is enabled again after an adjustable time interval. But nevertheless, one has to be aware that during the period of signal loss, no information on the actual density evolution is available, and even when the counter is locked, there is a large probability of losing fringes.
The pre-amplified detector signals are not only fed into the DCNPLL modules, but also

into envelope modules whose DC output voltage is proportional to the peak-to-peak voltage of the beat signal. This allows for a monitoring of the signal amplitude. The output of the DCNPLL phase counters and the envelope modules is sent to an analog-to-digital converter (ADC) that digitizes the data at a sampling rate of 10 kHz. The ADC output is stored locally in a CAMAC memory module during the discharge and transferred to the ASDEX Upgrade database afterwards. For density feedback control, however, the density signal has to be available in real-time. For this purpose, the output of the DCNPLL modules is in addition fed into a second ADC with lower sampling rate which is directly connected to the discharge control system.

5.1.2 Examples of fringe jumps

Figure 5.3 shows the density time trace for channel H-1 for discharge #23301 as recorded by the DCNPLL phase counter. The duration of the discharge is about 4 seconds, data acquisition started shortly before the gas in the vessel was ionized, so at t = 0, the electron density is equal to zero. In this discharge, no fringe jumps occur, therefore, the density

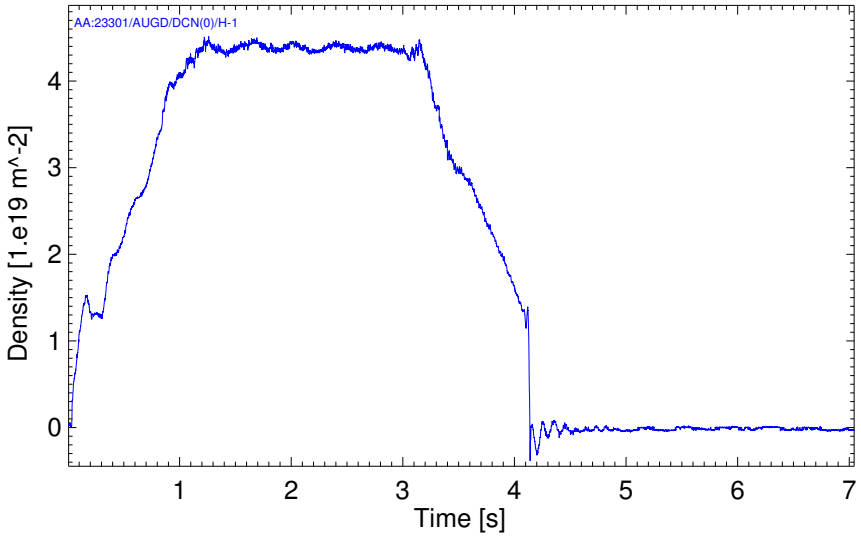

Figure 5.3: *Time trace of interferometer channel H-1 for ASDEX Upgrade discharge #23301 as recorded by the DCNPLL phase counter.*

signal returns to zero after the end of the discharge. In this example, the discharge enters the ramp-down phase, but shortly before its regular termination, it ends very suddenly in a small disruption of the plasma current at t = 4.1 s. This causes electromagnetic forces to act on the vacuum vessel and results in mechanic vibrations also of the in-vessel mirrors. As there is no second wavelength for compensation, a small oscillation of the signal around the zero line is observed right after the disruption. So mirror displacement effects are present in the density signal, however, their impact is not significant, the signal fluctuation due to such effects is much less than one fringe.
The above example illustrates the ideal case where one has a reliable density signal for

the full acquisition time, despite of the minor disruption. In contrast to the $CO_2/HeNe$ interferometer, for which fringe jumps do only result from electronic cross-talk, but not from plasma events, the DCN system is sensitive to certain plasma configurations. This mainly results from two aspects: On the one hand, beam deflection can occur when there are strong local density gradients in the plasma, which causes a drop of the laser power arriving at the detector and can make interferometry temporarily impossible. On the other hand, the beat frequency is just 10 kHz. If density changes by an amount that corresponds to half a fringe or more within 100 μs, there is a high risk of counting errors. There are some discharge scenarios that do typically result in fringe loss:

- **Disruptions**
  A disruption of the plasma current results in a sudden loss of confinement and rapid recombination of electrons and ions. As a result of this, the density drops to zero rapidly. In some cases, e.g. when quencher gases are injected for disruption mitigation, it can also happen that the density temporarily rises by a remarkable amount before it drops to zero. Such rapid density changes are not only critical to the interferometer as they may exceed the time resolution of the involved electronics, but they can also be correlated with strong density gradients that deflect the beam. Figure 5.4 shows an example of fringe loss in a disruption where the density signal ends up at +3 fringes after the discharge. Also the signal amplitude is shown, it can be seen that it

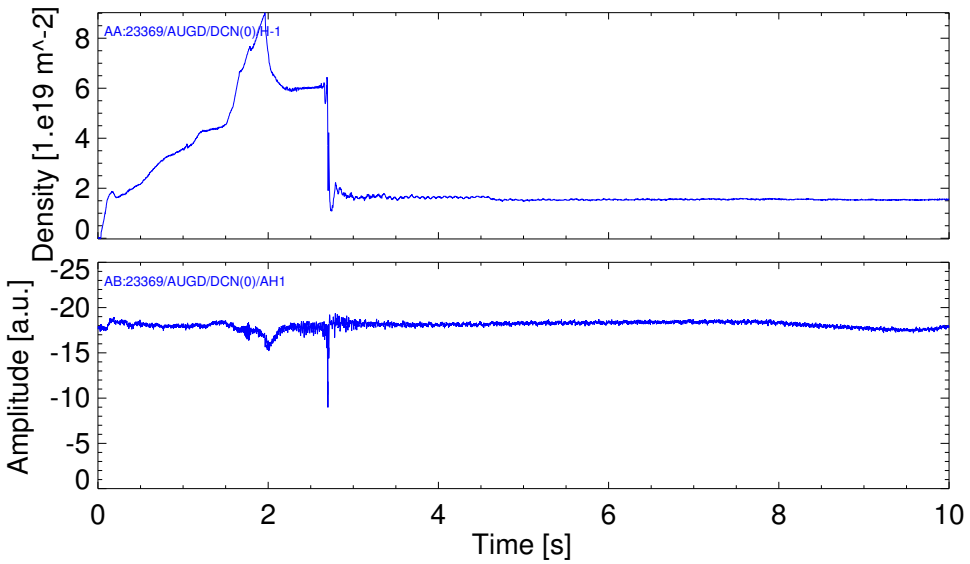

Figure 5.4: *Example of fringe loss during disruption in discharge #23369. The H-1 density signal does not return to zero after the end of the discharge. The amplitude signal strongly drops during the disruption event.*

clearly drops during the disruption. For real-time control, fringe loss in a disruption is not critical as in case of its occurrence, the discharge is over anyway and a wrong signal to plasma actuators will no longer have any effect. However, it restricts the

ability to measure the density during the disruption and study the disruption process itself.

- **Pellet injection**
  When pellets of frozen deuterium are injected into the plasma, the density locally increases rapidly due to the gas sublimating from the pellet surface. After that, a slow decay of density towards its previous value can be observed. As a result of this, the typical density time trace in case of pellet injection has sawtooth-like shape. The density fluctuation caused by small pellets can usually be resolved properly by the DCNPLL phase counters, but when going towards larger pellets, the probability for the phase counter to correctly follow the rising edge of the pellet signature decreases. The density decay phase, in contrast, does not cause any difficulties. Accordingly, large pellets make the phase counter register just a series of periods with falling density, whereas the rising edges in between are overlooked. The result can be seen in figure 5.5, where the time traces for 3 interferometer channels are shown for a discharge with pellets. As pellets enter the plasma at the separatrix and lose mass

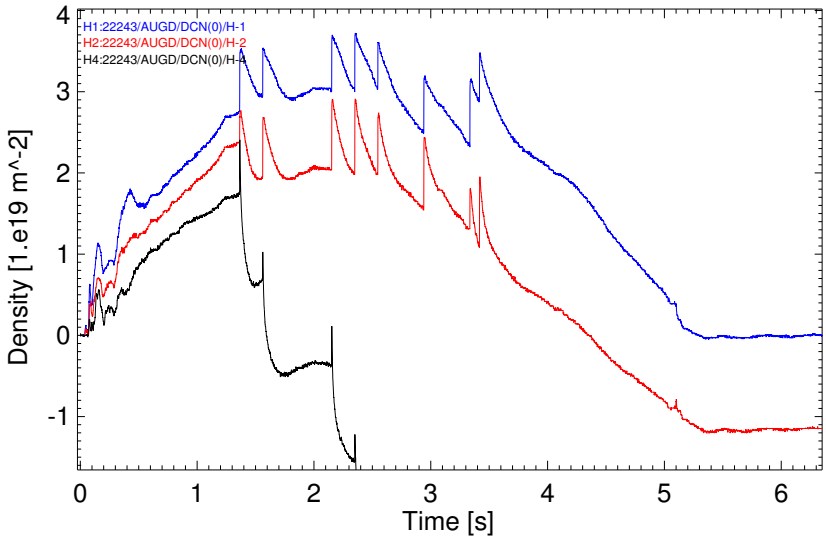

Figure 5.5: *Example of fringe loss during pellet injection in discharge #22243. The core channel H-1 (blue curve) is not affected by fringe loss at the given pellet size, H-2 (red) loses some fringes (e.g. 1 or possibly 2 fringes as the first pellet arrives) and H-4 (black) rapidly drifts away towards negative values.*

on the way to the core, the outer channels are more strongly affected by pellets than the central probing chords. Whereas the core channel H-1 returns to zero at the end of the discharge and is therefore supposed to represent the actual density evolution, the channel H-2 ends up at a negative density, which indicates that some rising edges have not been properly resolved. The H-4 density signal, however, rapidly drifts away towards negative values as almost all rising edges are overlooked by the phase counter. Due to this property of the DCNPLL modules (which affects all 5 channels at a certain pellet size), it is usually not possible to perform discharges with pellet

injection in density feedback mode as the faulty density signal would result in a much too wide opening of the gas inlet valves. But also in density feed-forward mode, fringe jumps can result in premature termination of the discharge as most heating systems are equipped with a low-density interlock.

- **Magnetohydrodynamic (MHD) activity**
  There is a large number of magnetohydrodynamic phenomena that can temporarily cause considerable density gradients in the plasma that deflect the DCN beam. As an example that mainly affects the core interferometer channel, the sawtooth instability will be shown later. An example where density gradients due to MHD activity make sub-millimeter interferometry difficult or even impossible all over the plasma volume is shown in figure 5.6, which shows the density time traces and the H-1 signal amplitude for discharge #24137. In this discharge, the gas inlet rate was continuously increased to explore the behavior at the density limit. When reaching the limit (around t = 2 s in this case), one typically observes a q=2/1 tearing mode which is accompanied by toroidally coupled q=1/1, q=3/1 and q=4/1 modes [27]. The corresponding strong density gradients at several radii make the laser power at the detector drop. As a result of this, the DCN interferometer can no longer make any useful measurement and erratic behavior of the time traces is observed.

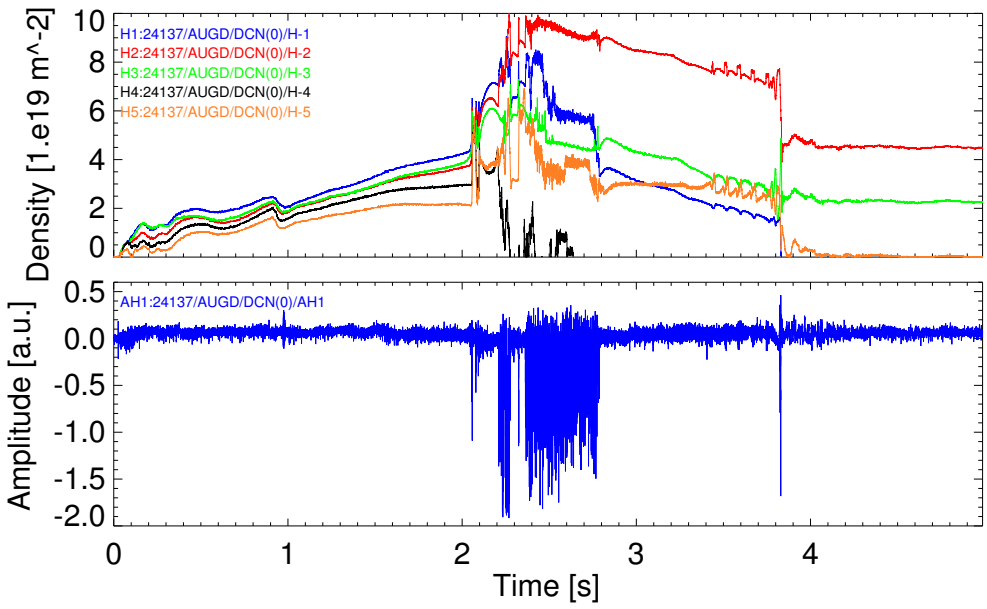

Figure 5.6: *Density time traces for all 5 DCN channels and signal amplitude of H-1 for ASDEX Upgrade discharge #24137.*

To sum up, mainly rapid changes of density and beam deflection due to local density gradients cause fringe loss. Whereas disruptions do anyway terminate the discharge and pellets

are actively injected into the plasma, so that one knows in advance that the density measurement may be affected and can e.g. switch the control system to feed-forward mode, fringe jumps due to MHD activity can hardly be predicted and are therefore most critical for real-time control.

An important feature of the DCNPLL system is the fact that the maximum phase change per time is limited (as the I/D out signal can only have a limited number of additional or omitted pulses within a given time interval), making the phase counter less sensitive to perturbations like electric noise.
However, the DCNPLL phase counters have a disadvantage regarding the possible amplitudes of fringe jumps. From the interferometric principle, it is evident that there is an unavoidable 2π ambiguity in density measurement. When a phase detector really measures the phase difference between plasma and reference signal, a fringe jump can only cause an error in phase measurement that is an integer multiple of 2π. The PLL circuit inside the DCNPLL modules, however, is just supplied with a square wave signal that has 16 times the frequency of the reference signal, but it does not receive the reference signal itself. This property also allows for phase jumps that are non-integer multiples of 2π, which causes an additional uncertainty. An event of this kind will be referred to as 'fractional fringe jump' in the further discussion. Such jumps will be difficult to correct afterwards, as the usual procedure of adding or subtracting integer multiples of $n_{e\,2\pi}$ will fail.
By looking into the ASDEX Upgrade database, it has been found that the majority of fringe jumps of the DCNPLL phase counters has an amplitude that is an integer multiple of 2π. Only a small number of fractional fringe jumps has been discovered. One example is shown in figure 5.7. If the density signal misses the zero line after the discharge by an amount

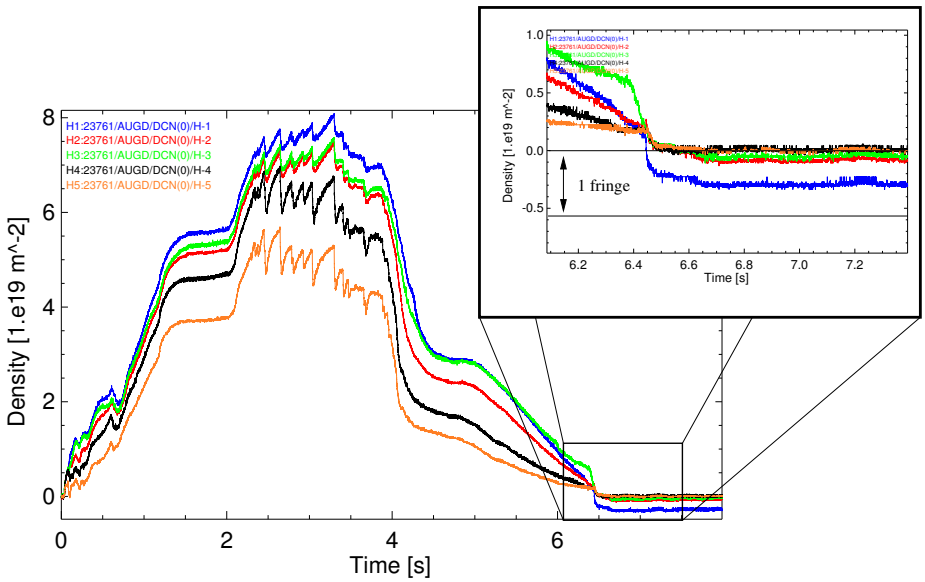

Figure 5.7: *An example of a fractional fringe jump by the DCNPLL phase counter for H-1. All 5 time traces start from the zero line at $t = 0\,s$. After the end of the discharge, however, the H-1 signal misses the zero line by about half a fringe.*

that is not an integer multiple of a fringe, this could also be due to mechanical variations of the path length. In this example, however, the channels H-2 and H-3 do not show a significant deviation from the zero line. As their lines of sight are parallel to that of H-1 and the in-vessel mirror for H-1 is located in between the other two mirrors, a mechanical reason such as vessel displacement relatively to the interferometer frame can be excluded, as it would also affect H-2 and H-3.
In the laboratory, fractional fringe jumps could be reproducibly generated with the DCNPLL modules by feeding a 10 kHz square wave signal twice into the phase counter, as reference and plasma signal as well, which results in a constant density output. When the plasma signal is switched off manually for a short period and then enabled again (which triggers the previously mentioned counter lock circuit), the output value differs from the previous one by about half a fringe.

5.2 Motivation for the electronics upgrade

When a density signal shall be used for real-time control, for example for the purpose of calculating and controlling density profiles, which will be described in the further course of this thesis, then it is important that fringe jumps can be recognized by a computer algorithm. If a jump occurs, correction may be attempted, for example by using another interferometer channel as reference. If this is not possible, the signal must no longer be used for feedback control and some alternative control scheme has to be applied. In such case, profile calculation has to be aborted, whereas feedback control on one of the DCN channels can be continued as long as not all 5 channels have been affected by fringe jumps. As soon as the last DCN channel has suffered from fringe loss, it is possible to use the density signals from the CO_2 interferometer for control. However, having only the output signal of the DCNPLL phase counters available, there is no unambiguous criterion for fringe jump detection. Using the time derivative of the density signal as criterion is not promising as in some cases (like overlooked pellets or edge localized modes), not the presence, but the absence of a large time derivative is characteristic of a fringe jump. The primary motivation for developing a new phase counter was to provide a system which, in the normal case, generates a stable density signal without fringe jumps, but which also provides a clear indication that fringes have been lost if the plasma conditions become difficult for interferometry. But there are also some further aspects about the DCNPLL modules which are unsatisfying:

- The DCNPLL phase counters can produce fringe jumps that are non-integer multiples of $n_{e\,2\pi}$. So in general, fringe jump correction in steps of $n_{e\,2\pi}$ is not fully sufficient.
- The response of the DCNPLL counters to rapid changes of density is not satisfying, especially in case of pellet injection as the sudden density rise during pellet ablation can not be resolved in many cases. As those rising edges are often overlooked by the phase counters, the density signal has the tendency to drift away towards negative values in such cases.
- The DCNPLL modules are equipped with a 4 kHz low-pass filter at the output side, which is required to suppress electric cross-talk from the digital side of the DAC

circuit. This filter also suppresses genuine fast oscillations of density in the multi-kilohertz range and makes fast changes of density appear delayed on the output. The delay is of the order of some hundred microseconds, which is not a critical issue for real-time control applications, but makes offline analysis at that high temporal resolution impossible, especially when the interferometer signal is compared to data from other diagnostics and conclusions shall be drawn from the relative time at which the different diagnostics detect some event in the plasma.

5.3 Design of the digital circuitry

For the development of new phase detectors, one important design criterion was fixed early: The counting of the fractions of a fringe (i.e. φ *modulo* 2π) and full fringes (i.e. an integer k so that $\varphi \in [k \cdot 2\pi; (k+1) \cdot 2\pi[$) should be separated. Whereas the number of fractional fringes immediately recovers from any perturbation, e.g. due to beam deflection, and can therefore be assumed to be always reliable, the number of full fringes may be affected by counting errors and therefore require for correction.
In addition, as it was evident that fringe jump detection and density profile calculation would have to be performed by a computer, it was desirable to build a phase counter with digital output so that no analog-to-digital converter (ADC) is required to read the data into a computer.
The signal path for the digital phase counter is identical to that of the DCNPLL modules until the comparators. After an individual set of comparators, the square wave plasma and reference signals are fed into the new electronics.
A summary of the following discussion of the circuit design can also be found in [28].

5.3.1 Counter for integer multiples of a fringe

Setting up a system that counts the number of full fringes is possible with a simple up-down binary counter (see figure 5.8). It counts up on a rising edge of the reference signal and

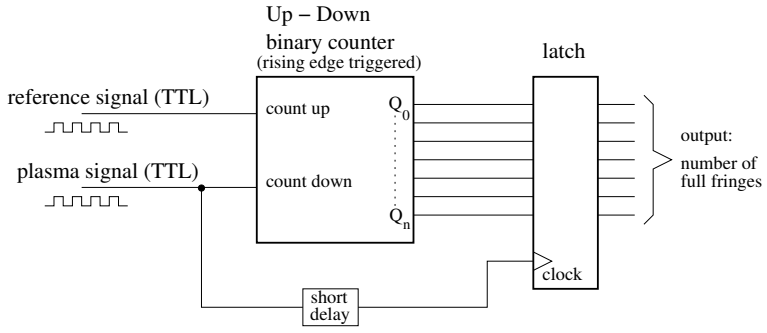

Figure 5.8: *A simple circuit that counts the number of full fringes.*

down on a rising edge of the plasma signal. If the number k of full fringes is constant, the counter reading always switches between the states k and k+1. If the number increases to k+1, the counter oscillates between k+1 and k+2, etc. So reading the output of the counter at a defined moment, e.g. right after it has received the rising edge of the plasma signal,

provides the number of full fringes (see figure 5.9). This was practically implemented by an additional 8-bit latch that receives a clock signal very short time after the rising edge of the plasma signal. As the binary counter is equipped with a preload function, is can be set to a defined value shortly before the plasma discharge starts.

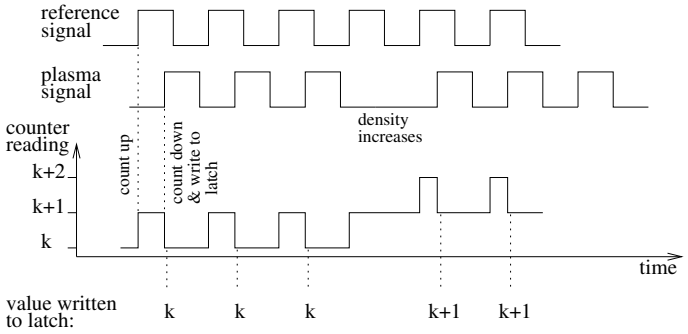

Figure 5.9: *Timing diagram of the circuit in figure 5.8.*

5.3.2 Counter for fractions of a fringe

The design of the fractional fringe counting stage is similar (see figure 5.10). Here, a phase-

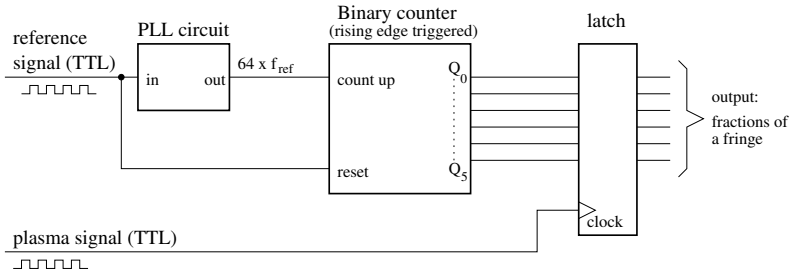

Figure 5.10: *A circuit that counts the fractions of a fringe in units of 1/64 fringe.*

locked loop circuit is used to generate a square wave signal that has 64 times the frequency of the reference signal. This is achieved by using an HCT4046 series IC and a 6-bit binary counter. This signal with a frequency of about 640 kHz, which will be referred to as 'clock signal' in the further discussion of the circuit, is fed into a 6-bit binary counter where it acts as 'count up' input. On a rising edge of the reference signal, the counter is set to zero. So if one plotted the counter reading versus time, the result would be a sawtooth-like structure: The value increases step by step from 0 to 63 and returns to 0 when the rising edge of the reference signal occurs (figure 5.11 illustrates the first counting steps). On a rising edge of the plasma signal, the counter reading is transferred into a latch. The content of the latch therefore is a binary number that represents the fractional phase shift φ *modulo* 2π in units of 1/64 fringe.

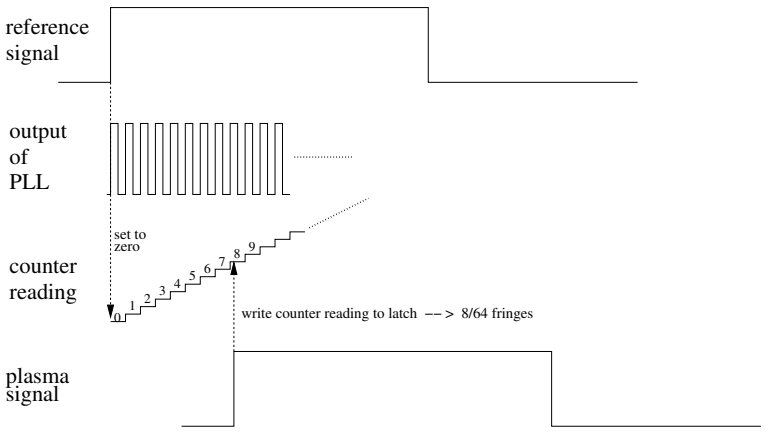

Figure 5.11: *Timing diagram of the circuit in figure 5.10. Pulse widths are not to scale.*

5.3.3 Complete circuit

The actual setup (see figure 5.12) is slightly more complicated than in the previous schematic description, as one has to take into account the gate delay of real TTL logic circuits. On

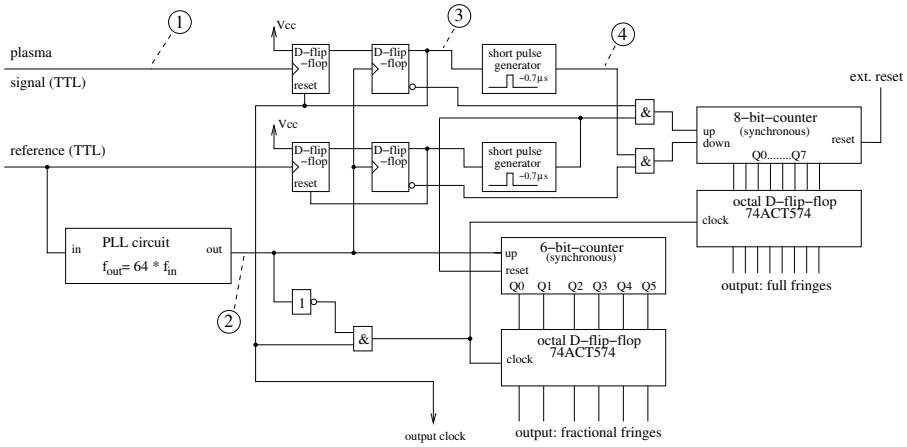

Figure 5.12: *Logic diagram of the digital phase counter. The numbers 1-4 refer to the signal timing diagram in figure 5.13.*

the one hand, the up-down-counter for the number of full fringes may show undefined behavior when the 'count up' and 'count down' signals arrive almost simultaneously, i.e. when plasma and reference signal are in phase. In order to avoid this situation, the rising edges of plasma and reference signal are delayed until the next rising edge of the clock signal (see figure 5.13). A similar procedure ("synchronized signal generator") is described in [29]. That way, the problem is discretized, the phase difference between plasma and reference signal can only change in discrete steps of 1/64 period and the question of simultaneity is simple to answer: Either the signals come precisely simultaneously, or there is a time offset of at least one clock cycle. In the case of simultaneity, the counter would receive 'count up' and 'count down' signals at the same time. This has to be avoided, as such case is not defined in the device specifications, so both pulses are suppressed in that case by a mutual

veto system that is built up with two AND gates: A rising edge of the plasma signal blocks the 'count up' signal during the same clock cycle, and vice versa.

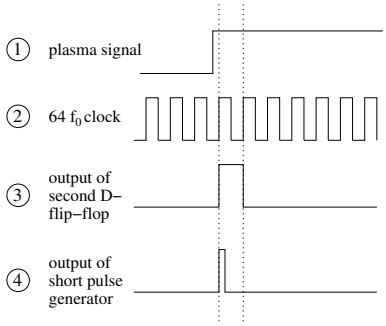

Figure 5.13: *Signal synchronization to the clock cycle. The relative timing of 4 signals given in figure 5.12 is shown.*

On the other hand, the occurrence of a rising edge of the plasma signal does not only make the counter for full fringes count down, but also has to generate a clock signal for the subsequent latch after a short delay. The required delay circuit was implemented with the help of a NOT and an AND gate and makes the clock signal for the flip-flops arrive half a clock period later.

5.4 Hardware implementations

5.4.1 The prototype

To achieve quick construction, the first prototype of the phase counter was built on a multi-purpose circuit board and all components were wired by hand. Figure 5.14 shows a photograph of the prototype device. The prototype had only 1 input channel and usually

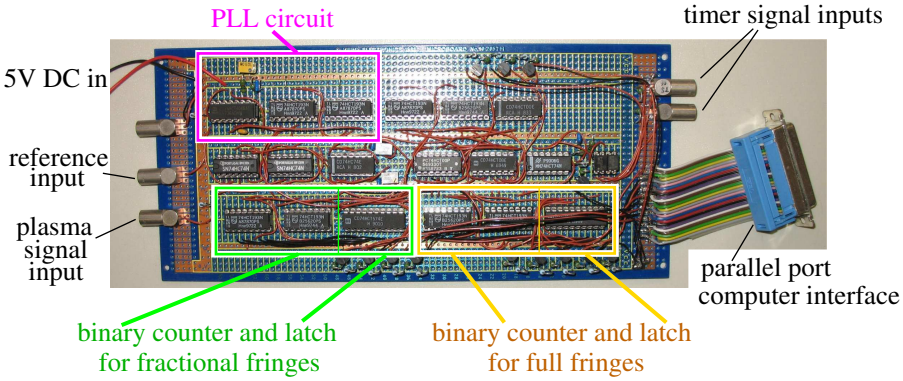

Figure 5.14: *A photograph of the prototype phase counter. On the left, the device receives reference and plasma signal from an external comparator. The two wires in the top left corner are for 5 V DC input. On the right hand side, the device receives two timer signals. Moreover, there is a 25-pin SUB-D connector that represents the computer interface.*

recorded the H-1 signal in parallel to the existing readout system. Data acquisition was performed via the parallel port of a personal computer. This port operates at the TTL-levels 0 V for logic 'low' and 5 V for logic 'high'. When both, the parallel port data register (8 bits) and the status register (5 bits) are used as inputs, a maximum of 13 TTL input lines are available. One of them was used for a timer signal and the remaining 12 lines were used to read data from the phase counter.
A principal weakness of the procedure of directly connecting the output of the phase counter to the computer port becomes apparent when the output of the counter changes just during a read process. In this case, the electric potentials at the output are not properly defined and one possibly gets a mixture of some bits from the old value and some from the new one. During the prototype phase, this was avoided by reading at a sampling rate that is several times higher than the counter update rate of 10 kHz. A value read from the parallel port was only accepted when it occurred at least twice in two subsequent read cycles.
With this prototype device, the general properties of the circuit were explored in the 2007 experimental campaign of ASDEX Upgrade and improvements were done until stable operation was achieved. For routine data acquisition, however, a 5-channel phase counter is required.

5.4.2 The printed circuit version

Following to the prototype, a printed circuit 5-channel phase counter was designed and built. As the phase-locked loop stage is supplied with the reference signal, which is the same for all 5 interferometer channels, this part had to be built only once. All the other components of the circuit, however, are implemented five times on the circuit board. With a total of 62 ICs on it, the board has dimensions of 21x21 cm (see figure 5.15). The input signals come via coaxial cables, the output is made available on a 75-pin connector in the center of the board. For each channel, there are 6 bits for the fractions of a fringe, 8 bits for the integer multiples and one clock bit (compare figure 5.12). The output timing is illustrated in figure 5.16: When a new density value is available (this is the case when a rising edge of the corresponding plasma signal arrives), the clock bit at the output goes to 'high'. About half a microsecond later, the other 14 output bits change their value. Again about 0.5 μs later, the clock bit returns to 'low'. This update process happens asynchronously for the 5 channels. The update frequency is given by the beat frequency (about 10 kHz) when density is constant. If density increases, the frequency is reduced, when it decreases, the frequency is higher.

To read the output data into the computer, a multiplexer with additional latch was built so that the 5 channels could be read one after the other. On a falling edge of the output clock, the multiplexer transfers the 14 density bits into its own latch and sets an internal index bit to 'high'. This index bit indicates that a new measurement has arrived in the latch. As long as it is high, no further input is accepted. This happens individually for all 5 channels. The computer does a continuous polling of the 5 channels. If the index bit is high, the computer reads the data bits and resets the index bit. If it is low, however, it just switches to the next channel.
First, data acquisition was done via the parallel port again, but later, a multi-purpose PCI-card with 32bit input and 32 bit output registers was used. With the printed circuit version, data acquisition was done from October 2007 to November 2008.
With both, the prototype and the printed circuit phase counter, an unintended behavior

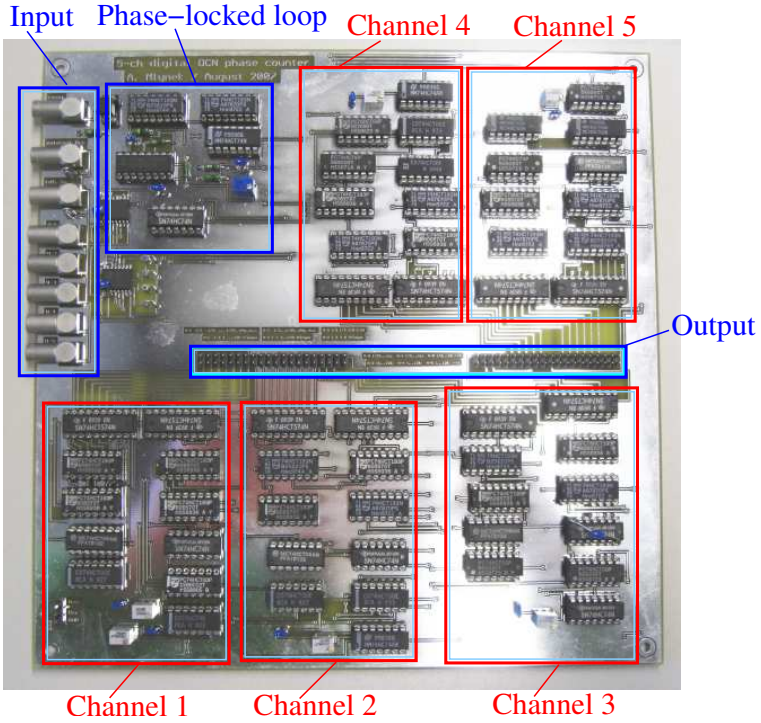

Figure 5.15: *A photograph of the printed circuit 5-channel phase counter.*

was observed when probe and reference signal were almost in phase, i.e. at the transition from one period to the next. This is illustrated in figure 5.17. In such case, there is some probability for the occurrence of a negative spike in the signal with an amplitude of 1 fringe. Having a closer look at the data in such region, one observes that in case of increasing density, the counter for the fractions of a fringe returns from 63 to 0 already one or two time steps before the counter for the full fringes counts up. In case of decreasing density, the counter for full fringes counts down before the one for fractions switches from 0 to 63. Therefore, the spikes have always negative sign. During the one year of operation of the printed circuit version of the phase counter, these noise spikes were removed by a real-time algorithm on the readout computer, which was simple to achieve due to the very characteristic signature of the spikes. They only occur when the density is around a full fringe and always go 1 fringe in the negative direction. Time traces from the printed-circuit device that are presented in the further discussion have undergone this noise removal algorithm.

After some investigation, the reason for this behavior could be identified: It is due to the fact that a phase-locked loop circuit never operates perfectly. In principle, each 64th rising edge of the clock signal should precisely coincide with a rising edge of the reference signal. In reality, however, there is always a slight jitter due to which it comes slightly before or after the edge of the reference signal. In case it comes before it, it may happen that there are 64 clock pulses between two rising edges of the reference signal. When plasma and reference signal are almost in phase, the counter for the fractions can therefore receive a further 'count up' pulse when the counter reading is 63 already. This causes an overflow from 63 to 0, which becomes apparent as a negative spike in the output signal. The likelihood for the occurrence of such situation can be significantly reduced by inverting the clock signal.

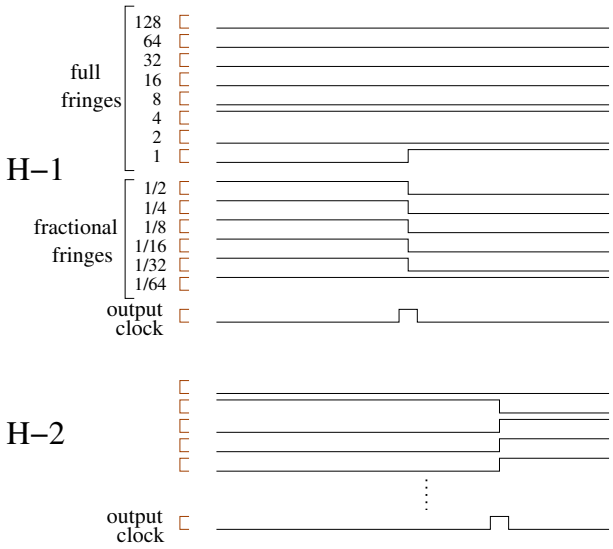

Figure 5.16: *Output timing of the 5-channel phase counter: When a new measurement of the phase shift is available, the output clock bit goes high first. About 0.5 µs later, the new result appears at the output. After further 0.5 µs, the output clock bit returns to low level. Each of the 5 channels has an individual timing.*

Then, a jitter of the PLL loop output only shows effect if it is more than half a period long. However, the better solution is to configure the counter for the fractions in a way that it accepts no further 'count up' pulses when the counter reading is 63, which means that it cannot overflow any more. This reliably removes all the spikes from the signal. This solution was implemented on the CPLD version of the phase counter, which is described in the next section.

5.4.3 The CPLD version

For feedback control applications, it was desirable to have a digital DCN phase counter that is compatible with the new standard for data acquisition hardware on ASDEX Upgrade, which is described in detail in [30]. For all diagnostics which are based on this system, a hardware and software framework for real-time communication with the control system is available. The new hardware standard is a backplane bus system, it is basically a 16-bit wide chain of D-type flip-flops (2x 74HCT574) with a tri-state output. The input of each chip in the chain is connected to the output of the previous chip and to the plug-in card. By switching the outputs of the flip-flops to high-impedance mode and enabling the output of the plug-in modules, the data from all modules can be loaded into the flip-flops simultaneously. Then, by disabling the outputs of the modules and activating the outputs of the flip-flops, the data can be successively moved forward in the flip-flop chain, like on a conveyor belt: With each clock pulse sent to the flip-flops, every chip loads the output of its predecessor in the chain. On the output side of the last IC in the chain, the results sent by the plug-in modules are picked up one after the other by a serializer card which sends them to a computer via optical fiber.
Due to the limited space on the standardized plug-in cards for this system and in order to allow for future modifications of the phase counter without rebuilding the hardware, the

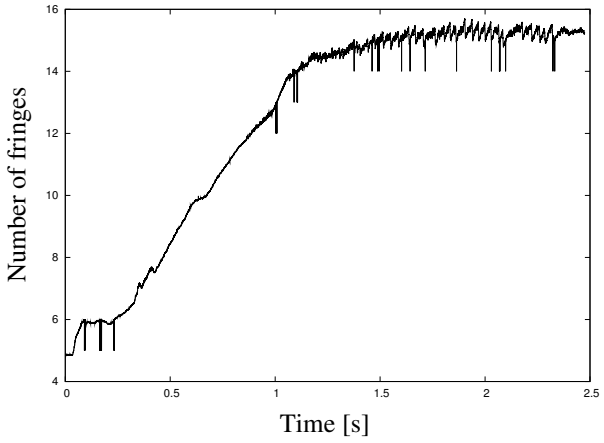

Figure 5.17: *Output of the printed-circuit phase counter during ASDEX Upgrade discharge #22990 for channel H-2. When the density crosses an integer multiple of a fringe, there is some probability of having a short spike with an amplitude of one fringe into the negative direction.*

circuit was implemented on a complex programmable logic device (CPLD) instead of using discrete ICs. This device is equipped with an interface for in-system-programming, so the internal circuitry can be modified without soldering. Just the phase-locked loop circuit is built up from discrete components located next to the CPLD.

The phase counter modules use 15 out of the 16 available output bits: 8 represent the number of full fringes, 6 the number of fractional fringes, and one acts as an update bit: It is set to 'high' level when a rising edge of the plasma signal arrives, i.e. when a new result appears on the output of the phase counter, and it is set to 'low' when the plug-in modules are read out via the backplane. The readout timing is a critical issue as the frequency at which the output of the phase counter is updated is given by the beat frequency of the detector signals and thus by the angular velocity of the rotating optical grating. This frequency is of the order of 10 kHz, but can vary by a few hundred Hertz as it is determined by a mechanical system. Therefore, reading at a fixed sampling rate of 10 kHz is not possible. Depending on the actual beat frequency, some samples would get lost, some would be read twice. This problem was solved by oversampling: The sampling rate is a multiple of 10 kHz, so that each output value of the phase counters is read several times. The update bit then indicates whether the current value is new or just a repetition of the previous one. For a sampling rate of 50 kHz, which is the usual setting, the update bit will therefore be found to be 'high' in each 5th sample on average. Oversampling is also beneficial for offline studies with high temporal resolution, as it reduces the timing uncertainty: When a new value (i.e. update bit 'high') is found at the output of the phase counter, one can only conclude that the update occurred between the current and the previous sample, but has no information on the exact time. At 50 kHz, this corresponds to an uncertainty of only 20 μs, which can be further reduced by increasing the readout frequency, if required.

Figure 5.18: *A photograph of the CPLD based phase counter in front of the crate with the backplane bus system.*

5.5 Data acquisition and interpretation

One second before the plasma discharge starts, the phase counters receive a reset signal from the discharge control system which sets the counters for full fringes to a defined value. Usually, this value is set greater than zero in order to allow for some fringe jumps in the negative direction without causing a counter overflow. After this, the data from the phase counters is read for a short time, usually about 100 ms, and the average is calculated. This defines the zero line of density measurement. The phase shift modulo 2π between probing and reference beam is usually not zero at the beginning of the discharge. It depends on the geometric path length of the probing beam and therefore changes whenever optical components are readjusted. When the plasma discharge starts, this zero level has to be subtracted from all values that are measured.
There are two different ways of calculating the density from the acquired data. The simplest approach is to add the number of full fringes and 1/64 times the number of fractional fringes, subtract the zero level and multiply the result by the amount of density that corresponds to one fringe ($0.572 \cdot 10^{19}\, m^{-2}$). The second way is to completely ignore the number of full fringes and use the information on fractional fringes only. Then the transitions from one period to the other have to be reconstructed by software. Initially, the number of full fringes is set to zero. If the number of fractions decreases by more than 32/64 in one time step, the number of full fringes is incremented by one. Accordingly, it is decremented by one if the number of fractions increases by more than 32/64 in one step. This method is based on the assumption that the phase change between two samples is usually less than half a fringe.
Thus, there are now three different density signals available per interferometer channel: The full output of the digital phase counter (which will be labeled 'H1full'-'H5full'), the density signal that is calculated from the output of fractional fringes only ('H1fract'-'H5fract'), and

the signal from the old DCNPLL modules, which are still operated in parallel.

5.6 Comparison of old and new density signals

As there are now 3 different density signals available per channel, comparative studies have been performed. None of these density signals can be regarded as 'perfect', as all of them can be affected by fringe jumps under certain conditions. The signal that is based on fractional fringes only, for example, will regularly lose fringes when the phase changes by more than half a fringe within 100 μs. If the beam is deflected due to density gradients in the plasma and misses the detector (which becomes apparent in a drop of the signal amplitude), no information on density at all can be obtained from the detector signal temporarily and fringe loss is unavoidable.
In the absence of perturbations, one expects that all three signals agree. The two signals from the digital phase counter do precisely agree, as the number of fractions is the same for both, i.e. they can only differ by integer multiples of a fringe. The DCNPLL signal, however, can deviate from that to a certain extent. When comparing the signals, two main aspects become evident (see figure 5.19):

- The absolute scaling is not identical. The density measured by the DCNPLL modules is about half a percent lower than the result provided by the digital phase counters. This amount of deviation is not the same for all discharges, but subject to fluctuations. This indicates the the DCNPLL modules do not precisely meet their calibration specification of 100 millivolts per fringe. In the output stage, they are equipped with potentiometers for offset and amplifier gain adjustment. The observed deviation is attributable to an imprecise gain setting or to a slight drift of the actual amplifier gain with time. Also scale errors of the subsequent ADCs are a possible explanation. The digital phase counters avoid such error sources.

- Quick changes of density appear with a delay of the order of 300 μs on the DCNPLL signal. This is due to the 4 kHz low-pass filter at the output of the modules. It has been made sure that both signals obtain their time stamps from the same timer system, so that different time bases can be excluded as reason.

A further effect of the low-pass filter appears on channel H-1 in discharge #23878 (see figure 5.20). In the given time interval, a sawtooth instability (see appendix A.1) in the core plasma occurs. A rotating island around the q=1 surface periodically crosses the line of sight of the interferometer channel H-1. This causes a periodic oscillation of the line-integrated density at a frequency of about 2 kHz. This oscillation can hardly be seen on the DCNPLL signal, as its amplitude is strongly reduced compared to the new electronics. Figure 5.21 illustrates the relative location of the q=1 surface, the lines of sight H-1 and H-3 of the DCN interferometer, the lines of sight of the soft X-ray diagnostic and the location that corresponds to channel 60 of the electron cyclotron emission radiometer. The toroidal location of interferometer and soft X-ray diagnostic is the same, whereas the toroidal location of the ECE diagnostic differs by about 45 degree. Figure 5.22 shows the time traces for these diagnostics, namely channels H-1 and H-3 of the DCN interferometer as measured by the new electronics, channels 51, 52 and 57 of the soft X-ray diagnostic and channel 60 of the ECE radiometer. Channels 51 and 52 of the soft X-ray diagnostic, ECE channel 60 and the DCN H-1 signal oscillate in phase. The soft X-ray channel 57 oscillates at the

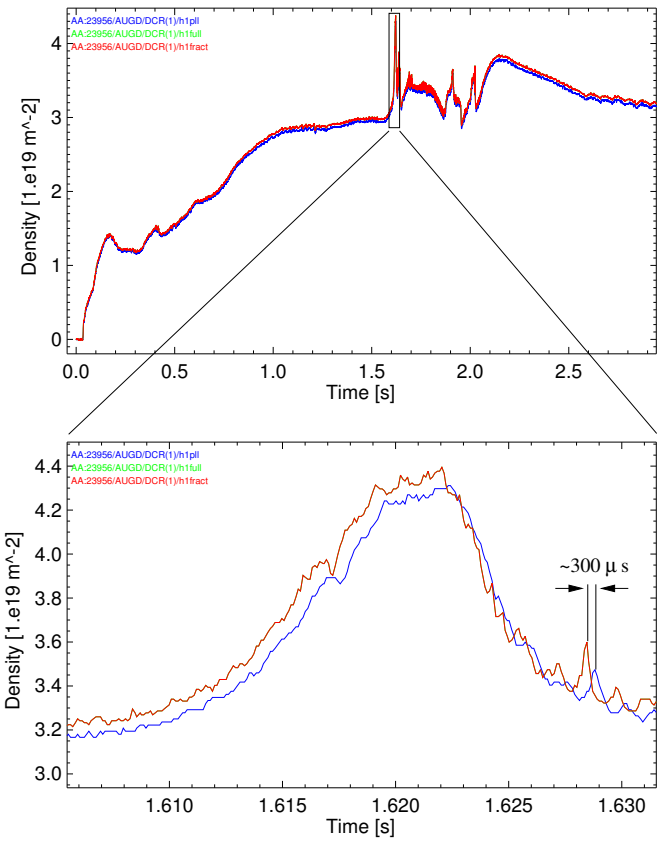

Figure 5.19: *Comparison of H-1 signals from digital phase counter (red) and DCNPLL phase counter (blue) for discharge #23956. The two digital signals ('H1full' and 'H1fract') agree, therefore, the third curve is hidden behind the red one.*

same frequency, but has a phase shift of half a period, and interferometer channel H-3 does not show significant oscillation. This gives a consistent picture of a rotating island, as the line of sight of H-3 is located outside the q = 1 surface, line 57 of the soft X-ray diagnostic intersects it in the lower part and all the other diagnostics probe the upper part of the q = 1 surface. This illustrates that the fast response of the digital phase counter opens up new possibilities in studying MHD phenomena in the multi-kHz frequency range. In the output of the new phase counters, density oscillations in this frequency range have been observed in many other discharges, especially on the central channels and often during the ramp-down phase of the discharge. In some cases, there is no evident correlation to events like a sawtooth instability. However, within the scope of this thesis, it was not possible to investigate this in more detail.

The sawtooth instability nicely illustrates how plasma conditions can make interferometry in the sub-millimeter wavelength range temporarily impossible: There is a very localized, small-scale object with high density in the plasma, namely the rotating mode. On the one hand, it causes a significant change of density within short time when crossing the line of sight of the interferometer, which is critical for the density measurement, and on the other

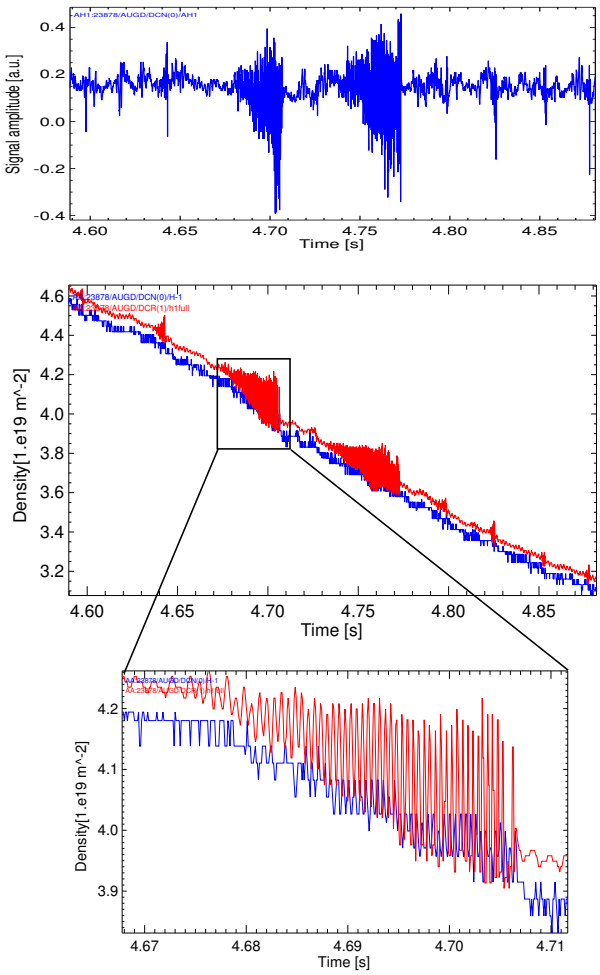

Figure 5.20: *Precursor oscillations of a sawtooth crash in discharge #23878. The uppermost box shows the signal amplitude at the output of the H-1 detector. In the other two boxes, a comparison of the H-1 density signals from the digital phase counter (red) and the DCNPLL phase counter (blue) is shown.*

hand, it acts like a dispersing lens on the laser beam, which causes a rapid modulation of the amount of laser power that reaches the detector (see upper box in figure 5.20). As the plasma anyway deflects the beam a little, it is not perfectly centered on the detector and the local lens effect can temporarily also result in an increase of the arriving power. In the presented case of the sawtooth instability, the size of the mode is still moderate and therefore, no fringe jumps occur. However, in case of larger modes, interferometric density measurement can become impossible and the actual density evolution most likely cannot be extracted from the detector output signals any more, no matter how sophisticated the signal processing may be.

In the presence of perturbations, it may happen that only one or two signals suffer from fringe jumps, or that all three are affected. However, in the latter case, the likelihood for

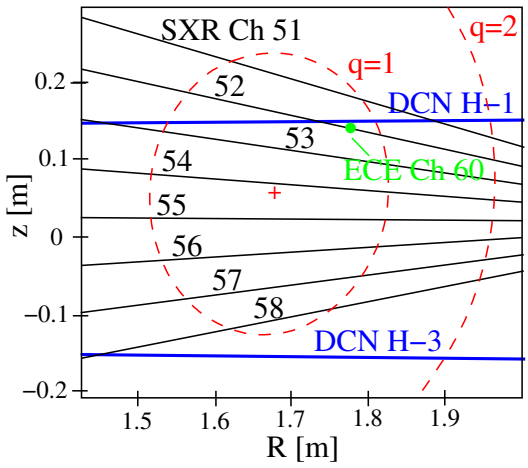

Figure 5.21: *Location of the q=1 surface, the lines of sight of DCN interferometer and soft X-ray diagnostic and the location of channel 60 of the ECE radiometer for discharge #23878 at t=4.7s.*

all three signals to lose the same number of fringes at the same time is small. The much more probable case in which all three signals lose a different number of fringes is illustrated in figure 5.23. All three signals fail to return to the zero line at the and of the discharge. The signal 'H1full' loses 8 fringes, the signal 'H1fract' 5 fringes and the DCNPLL signal about 1.5 fringes (as discussed earlier, counting errors by fractions of 2π can occur on the DCNPLL system).
Figure 5.24 shows two further examples of fringe jumps. Due to the different operating principle of the phase counters, the response to perturbations is different in most cases. Therefore, simple comparison of the 3 different density signals that are now available per channel is a very powerful tool for signal validation. As long as all 3 signals agree within a defined error band, the signal can be regarded as reliable. This error band has to be less than one fringe on the one hand, but must be greater than zero on the other hand to account for differences that result from the slightly different scaling of the DCNPLL signal, the different resolution (the digital system can perform 4 steps of 1/64 fringe while the DCNPLL signal is constant) and the slower response of the DCNPLL system to rapid changes of density. Usually, half a fringe is an adequate choice for the maximum tolerable difference. When all 3 signals are consistent within this limit, the signal can be labeled as valid. The likelihood of overlooking fringe jumps with this validation procedure is rather low. Within 841 ASDEX Upgrade discharges that were analyzed in detail and provide 4205 density time traces, only 21 cases have been found in which all 3 signals jump by the same number of fringes at the same time. However, 17 out of those 21 overlooked fringe jumps occurred in a disruption. Accordingly, only in 4 cases a validated density signal has been found to be incorrect due to fringe jumps during the useful flat-top phase of a plasma discharge.
For all control applications that sensitively depend on a correct density signal, it is therefore desirable to use only signals that have passed this validation algorithm. Also for the calculation of density profiles, which will be described in the next chapter, only validated density signals will be used. In the discharge scenarios that were used for the experiments for this thesis, the frequency of occurrence of fringe jumps was moderate, so one could afford to

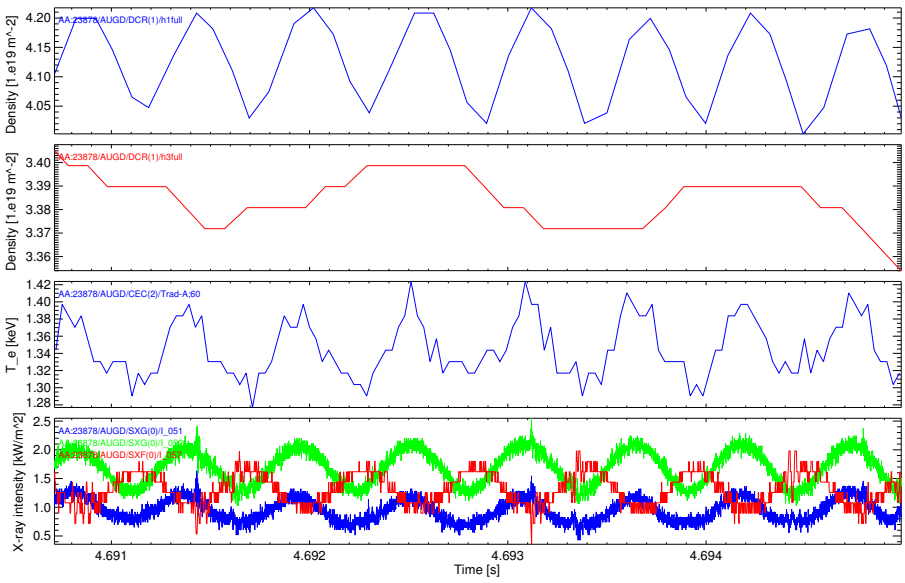

Figure 5.22: *Time traces from different diagnostics for discharge #23878 during a saw-tooth precursor (from top to bottom): DCN channels H-1 and H-3, ECE channel 60 and three soft X-ray channels (Ch 51 in blue, 52 in green and 57 in red).*

give up a discharge and repeat it if one of the interferometer channels did no longer fulfill the validation criterion. For future real-time applications, which aim at discharge scenarios with higher MHD activity and therefore higher risk of encountering fringe jumps, it may be necessary to implement real-time correction strategies which allow to continue with the feedback program after a fringe jump. On the one hand, the stability of the new phase counters in presence of MHD activity could most probably be increased by implementing the techniques described in reference [31]. There, the comparator that converts the almost sinusoidal plasma and reference signals into TTL signals, is equipped with two thresholds which both have to be crossed within a defined time window. This allows to avoid spurious rising edges due to fluctuations of the signal amplitude, which are characteristic of phases with MHD activity. In addition, the time difference between the arrival of rising edges in the plasma signal is monitored and required to be within a plausible time window. If it is outside it, an automatic phase correction is performed. The latter technique could be implemented on ASDEX Upgrade without modifying the hardware, as the information on the time of arrival of rising edges in the plasma signal is still present in the output of the digital phase counter in form of the update bit. The implementation would therefore only require software modifications. On the other hand, real-time fringe jump correction may be done by using neighboring DCN channels or a channel of the vertical CO_2 interferometer as reference. However, as the experiments relevant for this work could be carried out without such correction strategies, no additional effort was invested into their implementation.

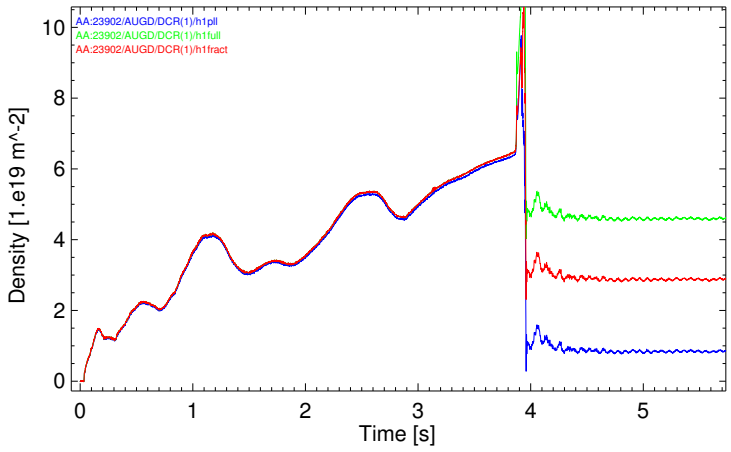

Figure 5.23: *Fringe loss during disruption in discharge #23902. The blue curve represents the DCNPLL signal. The green ('H1full') and the red signal ('H1fract') were obtained from the digital phase counter.*

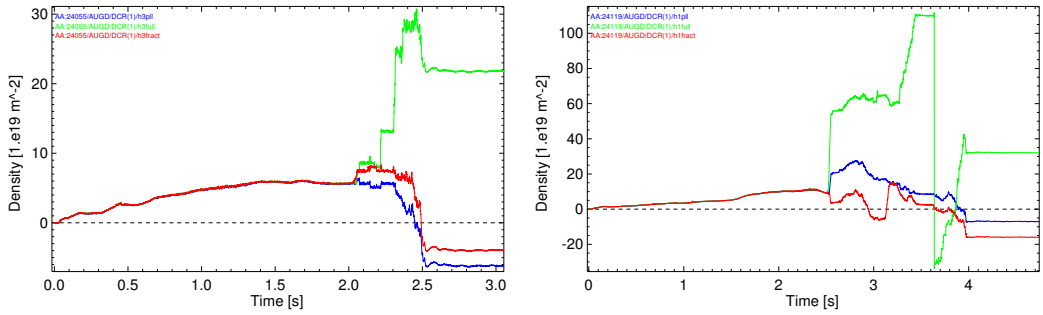

Figure 5.24: *Two examples of fringe loss due to MHD activity. Left: Discharge #24055, channel H-1. Right: #24119, channel H-3. After the onset of the perturbation, the three phase detection schemes show different behavior. In the second case, the counter for full fringes (green curve) of the digital device produces so many counting errors in the positive direction that a counter overflow occurs. This results in a large jump towards negative density.*

6 Reconstruction of the density profile

The interferometer provides a measurement of the line-integrated electron density along several lines of sight. The aim is to reconstruct the local electron density at any point in the two-dimensional (poloidal) cross section of the plasma. The general problem therefore is to reconstruct the structure of some n-dimensional object when only (n-1)-dimensional projections of the structure can be measured. An example of this can also be found in medicine: A computer tomograph is used to explore the (3-dimensional) internal structure of the patient's body. The tomograph consists of an X-ray source and a detector array which rotate around the patient. The intensity that arrives on a detector pixel depends on the line integral of the X-ray attenuation coefficient between source and detector pixel. By rotating source and detector array, projections along a large number of different angles are obtained. This allows for reconstruction of the spatial distribution of the X-ray attenuation coefficient, and that way, of the kind of biological tissue. This reconstruction technique is often referred to as 'tomographic inversion'.

6.1 Assumption of constant density on flux surfaces

In case of fusion plasma interferometry, the number of lines of sight is limited, as each line of sight usually requires at least one individual vessel port. An exception are so-called scanning interferometers (compare ref. [32]), which, however, are presently only found on smaller fusion devices. In addition, it is not possible to rotate the plasma relatively to the interferometer setup, so the projection angle cannot be altered. The reconstruction of the plasma density profile therefore has to operate with a very limited number of lines of sight. In contrast to the medical application mentioned above, where much more lines of sight are available so that the structure can be determined from the measured data with good resolution, density profile reconstruction is not possible without making additional assumptions. As particle transport along field lines is by orders of magnitude larger than perpendicular to them (compare chapter 2), the plasma density is usually assumed to be constant on flux surfaces. For this reason, a reconstruction of the density profile does not only require the line-integrated density measurements from the interferometer as input, but also information on the location of the flux surfaces. The magnetic equilibrium is provided by a diagnostic which relies on the measurements by pickup coils that are located on the inner vessel wall, see chapter 3. From these measurements, the poloidal magnetic flux function Ψ can be calculated by numerically solving the Grad-Shafranov equation. This is done routinely in off-line data analysis [33], however, for real-time application, it presently still consumes too much computing power. Therefore, a quicker, but less precise solution via functional parameterization is available on ASDEX Upgrade, which provides a 69×39 matrix that contains the values of the poloidal flux Ψ [34]. It corresponds to a rectangular

grid based on 39 radial and 69 vertical positions with a spacing of 4 cm (see figure 6.1), where each matrix element refers to one grid point. Also the value Ψ_a of the flux function

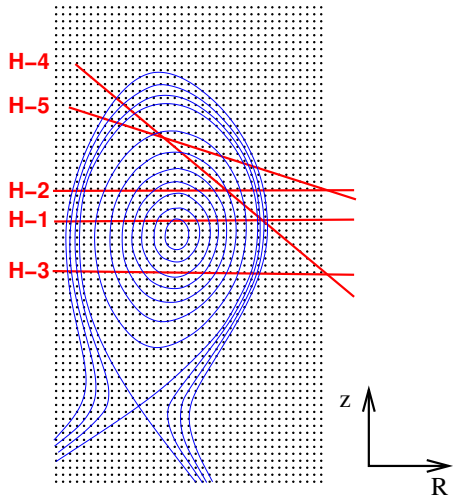

Figure 6.1: *An illustration of the discrete* 69×39 *grid on which the value of the flux function* Ψ *is calculated via functional parameterization in real-time. In addition, the lines of sight of the DCN interferometer are shown, and some flux surfaces, which have been calculated by linear interpolation between the grid points.*

at the magnetic axis, the value Ψ_s at the separatrix and the value Ψ_{lim} at the limiter are provided by this diagnostic.
Due to the assumption of constant density on flux surfaces, the reconstructed density profile is a function that depends on only one scalar parameter, which has to be some flux surface label. Commonly, the normalized poloidal flux radius ρ_{pol} (see equation 3.2 in chapter 3) is used for this purpose. Accordingly, the function that describes the density profile will be labeled $n_e(\rho_{pol})$.
Combining the measurements of the horizontal DCN interferometer and the two vertical lines of sight V-1 and V-2 of the $CO_2/HeNe$ interferometer could provide a total of 7 lines of sight. However, in [35] it is reported that channel V-2 registers densities in excess of those expected from core and scrape-off layer parameters, which originates from particle recycling at the vessel wall at the inner, lower divertor baffle. This prevents one from using this interferometer channel for profile calculation. The remaining channel V-1 could in principle be used, but due to the high noise level of the $CO_2/HeNe$ interferometer, one would have to average the V-1 density over several milliseconds, which deteriorates the temporal resolution. Despite of such averaging, the noise level still remains higher than that of the DCN system. The price paid for one additional line of sight would therefore be an increased level of spurious fluctuation of the resulting density profile. For this reason, only the measurements of the DCN interferometer will be used for profile calculation.
Having the line-integrated electron densities along 5 lines of sight and the ρ_{pol} matrix available, the challenge is now to find an algorithm that reconstructs the electron density $n_e(\rho_{pol})$ and is fast enough to be used in real-time with the presently available computer processors. Here, the following method will be applied: The density profile is parameterized by a set of basis functions, involving a set of unknown coefficients. Then, based on the given magnetic configuration, the five line integrals are calculated as a function of those

coefficients. Finally, the calculated line integrals are compared to the actual measurements by the interferometer and the profile coefficients are determined. The following sections describe these three major steps in detail.

6.2 Parameterization of the density profile

The approach for profile calculation that is presented here is based on a parameterization of the density profile $n_e(\rho_{pol})$ as a linear combination of a set of basis functions. Taking into account the given magnetic equilibrium, the line-integrated densities along the 5 lines of sight of the interferometer are then calculated as a function of the coefficients. The calculated line-integrals are finally compared to the actual measurements and the profile coefficients are determined in a way to provide best consistency.
There are some restrictions to the choice of the basis functions, which become apparent when discussing the properties of the density profile $n_e(\rho_{pol})$:

6.2.1 Behavior at the magnetic axis

One has to take into account that n_e can be written as a function of the geometric coordinates R and z by inserting $\rho_{pol}(R,z)$ as an implicit function. The resulting function $n_e(R,z)$ must be differentiable everywhere inside the separatrix, so the gradient with respect to the cartesian coordinates R and z has to be well-defined and any directional derivative inside the separatrix must be defined and continuous. This is especially valid for the magnetic axis. The poloidal magnetic flux function $\Psi(R,z)$ is known to be differentiable, so it is helpful to write the electron density n_e as a function of Ψ:

$$n_e(\rho_{pol}(R,z)) \;=\; n_e\left(\sqrt{\frac{\Psi(R,z)-\Psi_a}{\Psi_s-\Psi_a}}\right)$$

According to the chain rule, the derivative with respect to R is given by

$$\frac{\partial n_e}{\partial R} \;=\; n_e'\left(\sqrt{\frac{\Psi(R,z)-\Psi_a}{\Psi_s-\Psi_a}}\right)\cdot\frac{\sqrt{\Psi_s-\Psi_a}}{2\sqrt{\Psi(R,z)-\Psi_a}}\cdot\frac{1}{\Psi_s-\Psi_a}\cdot\frac{\partial\Psi(R,z)}{\partial R}\,.$$

As the expression $\sqrt{\Psi(R,z)-\Psi_a}$ appears in the denominator, there is the possibility of having a discontinuity or even singularity at $\Psi=\Psi_a$, i.e. at the magnetic axis. However, as Ψ has a local extremum at the axis (the corresponding coordinates will be referred to as R_a and z_a), its derivative will vanish there, so the last factor in the above equation also goes to zero in the limit $(R,z)\to(R_a,z_a)$. In order to check whether a discontinuity or singularity actually occurs, a closer look at $\Psi(R,z)$ is required. The Taylor series of Ψ around the magnetic axis contains the constant Ψ_a (this is, by definition, its value at the axis), but the terms that are linear in $(R-R_a)$ and $(z-z_a)$ vanish as Ψ has a local extremum at the axis. The question now is whether there will in general appear terms proportional to $(R-R_a)^2$ and $(z-z_a)^2$. When substituting the definition of Ψ (equation (3.1)) into Ampere's law $\vec{\nabla}\times\vec{B}=\mu_0\vec{j}$ and solving with respect to the toroidal component j_ϕ of the current density, one obtains

$$-\mu_0 R j_\phi \;=\; R\frac{\partial}{\partial R}\frac{1}{R}\frac{\partial\Psi}{\partial R}\;+\;\frac{\partial^2\Psi}{\partial z^2}\,.$$

When inserting the simple test function $\Psi(R,z) = (R-R_a)^m \cdot (z-z_a)^n + \Psi_a$, which contains a general prototype of all terms that can appear in the Taylor series, the right-hand side becomes

$$(z-z_a)^n \left(m(m-1)(R-R_a)^{m-2} - \frac{1}{R} m (R-R_a)^{m-1} \right) + n(n-1)(z-z_a)^{n-2}(R-R_a)^m \; .$$

In order to allow for a non-zero current density at the magnetic axis (which is the usual case in a tokamak, the somewhat exotic exception of a current hole may be neglected here), there have to be terms with $m = 2,\ n = 0$ or $m = 0,\ n = 2$. The third possibility, which would be $m = 1,\ n = 0$, is excluded by the existence of a local extremum of Ψ at the magnetic axis. Thus, in general, there are square terms in the Taylor series of $\Psi(R,z)$ at the magnetic axis.
With this knowledge, a very simple example of $\Psi(R,z)$ can be used:

$$\Psi(R,z) = (R-R_a)^2 + (z-z_a)^2 + \Psi_a \; .$$

For simplicity, we only focus on the directional derivative along $z = z_a$, then the equation for the derivative of n_e becomes:

$$\frac{\partial n_e}{\partial R} \;=\; n_e' \left(\frac{|R-R_a|}{\sqrt{\Psi_s - \Psi_a}} \right) \cdot \frac{\sqrt{\Psi_s - \Psi_a}}{2|R-R_a|} \cdot \frac{1}{\Psi_s - \Psi_a} \cdot 2(R-R_a) \; .$$

The expression besides n_e' goes to $+(\Psi_s - \Psi_a)^{-1/2}$ in the limit $R \to R_a+$ and to $-(\Psi_s - \Psi_a)^{-1/2}$ in the limit $R \to R_a-$, so there is a discontinuity at $R = R_a$. The whole expression is only continuous at the magnetic axis when $n_e'(\rho)$ is equal to zero at $\rho = 0$. Therefore, any function that is used to parameterize $n_e(\rho)$ must have zero derivative at zero.

6.2.2 Behavior at the separatrix

As the separatrix is the last closed flux surface by definition, particles that move from a $\rho_{pol} < 1$ region to a $\rho_{pol} > 1$ region due to perpendicular transport are no longer confined, but move to the divertor baffles and are rapidly removed out of the system. Due to this particle sink, the density profile drops rapidly in the scrape-off layer. When considering an orthonormal basis $\{\hat{e}_\rho,\ \hat{e}_\xi,\ \hat{e}_\zeta\}$, where $\hat{e}_\rho$ is perpendicular to the flux surfaces and $\hat{e}_\xi$ and e_ζ are two linearly independent vectors which span the flux surface, and taking into account only diffusive particle transport (i.e. the first term in equation (2.1) in chapter 2), then the particle flux $\vec{\Gamma}$ is given by

$$\vec{\Gamma} \;=\; -D\frac{\partial n_e}{\partial \rho}\hat{e}_\rho - D\frac{\partial n_e}{\partial \xi}\hat{e}_\xi - D\frac{\partial n_e}{\partial \zeta}\hat{e}_\zeta \; .$$

Accordingly, the absolute value of the particle flux is given by

$$\left|\vec{\Gamma}\right| \;=\; D\left(\left|\frac{\partial n_e}{\partial \rho}\right| \;+\; \left|\frac{\partial n_e}{\partial \xi}\right| \;+\; \left|\frac{\partial n_e}{\partial \zeta}\right| \right) \; .$$

Inside the separatrix, we have $\left|\frac{\partial n_e}{\partial \xi}\right| + \left|\frac{\partial n_e}{\partial \zeta}\right| = 0$, as the density is constant on flux surfaces, outside the separatrix, however, this expression is greater than zero due to the particle sink. As the particle flux through the separatrix is conserved, this requires a discontinuity of $\frac{\partial n_e}{\partial \rho}$, i.e. of the density profile, at the separatrix. Algorithms for profile calculation which do not

use any input data from edge diagnostics, such as reflectometry or lithium beam impact excitation spectroscopy, do therefore usually allow for a discontinuity of the first and all higher derivatives of $n_e(\rho_{pol})$ at $\rho_{pol} = 1$. This will also be done here. Accordingly, $n_e(\rho_{pol})$ will be assumed to be a smooth function inside the separatrix, i.e. to be several times continuously differentiable in the interval $[0, 1[$, and to be a smooth function in the scrape-off layer, where it is assumed to be monotonously decreasing. At the separatrix ($\rho_{pol} = 1$), however, the density profile is continuous, but not necessarily differentiable. With this assumption, it is not possible to expand $n_e(\rho_{pol})$ into a Taylor series for the whole range of ρ_{pol} values (which is usually something like [0,1.1] or [0,1.2]). Taylor expansion is only possible in 2 sections, namely $0 \leq \rho_{pol} \leq 1$ and $\rho_{pol} \geq 1$. Typically, two different functions will be used to describe ρ_{pol} in these two sections. The only matching condition is that their value at $\rho_{pol} = 1$ agrees, but all derivatives can be discontinuous at this point. The density in the scrape-off layer will be assumed to drop to zero at the limiter position, which will be labeled ρ_{lim}.

As the algorithm for real-time density profile calculation does not have access to a direct measurement of the edge density, and as the scrape-off layer does not contribute much to the measured line integrals, no attempt will be made to extract information on the density decay in the scrape-off layer from the interferometer data, i.e. no additional free parameter will appear in the parameterization of $n_e(\rho_{pol})$ which exclusively affects the scrape-off layer. In contrast, a fixed density decay function $g(\rho_{pol})$ will be used which fulfills $g(1) = 1$, is monotonously decreasing and whose decay length is calculated from ρ_{lim}, i.e. from magnetic measurements only.
The following parameterization of $n_e(\rho_{pol})$ will be used:

$$n_e(\rho_{pol}) = \begin{cases} \sum_{k=1}^{M} a_k \, f_k(\rho_{pol}) & if \;\; \rho_{pol} \leq 1 \\ g(\rho_{pol}) \cdot \sum_{k=1}^{M} a_k \, f_k(1) & if \;\; 1 < \rho_{pol} \leq \rho_{lim} \\ 0 & if \;\; \rho_{pol} > \rho_{lim} \end{cases} \tag{6.1}$$

The density profile is thus assumed to be a linear combination of M basis functions $f_1, \ldots, f_M$ with coefficients $a_1, \ldots, a_M$ in the main plasma, where each basis function has to fulfill the condition $f_k'(0) = 0 \quad \forall\, k = 1, \ldots, M$.
As the next step, the 5 line-integrated densities will be calculated as a function of the M coefficients $a_1, \ldots, a_M$ for a given magnetic equilibrium.

6.3 Discretization of the line integral

As illustrated in figure 6.1, the value of the normalized poloidal flux radius ρ_{pol} is given on a discrete 69×39 grid. Using the positions of the grid points and the DCN beam coordinates, the first step is to calculate a set of ρ_{pol} values that correspond to equidistant points on each line of sight of the interferometer. This is done via linear interpolation between the corresponding data points above and below the line of sight (see figure 6.2). The resulting

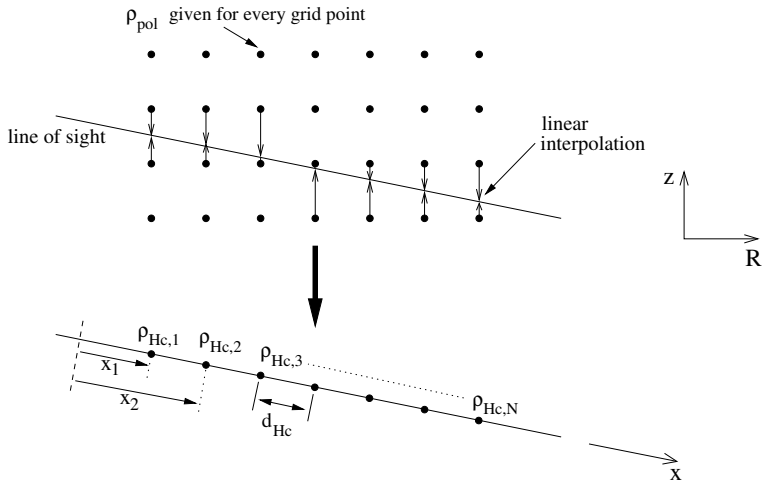

Figure 6.2: *The poloidal flux is calculated for equidistant points along the line of sight via linear interpolation.*

values will be referred to as $\rho_{Hc,i}$, where the first index $c \in \{1, 2, \ldots, 5\}$ indicates the interferometer channel H-1 to H-5 and the second index $i \in \{1, \ldots, N\}$ increases along the line of sight. A spatial coordinate x along the line of sight is introduced whose point of origin is located at an arbitrary position outside the plasma vessel. The x-values that correspond to the intersections with the vertical grid lines will be referred to as $x_1, \ldots, x_N$. The distance between the points will be labeled d_{Hc} in the further discussion. Evidently, we have $x_{i+1} = x_i + d_{Hc}$. Based on this discrete set of points on the line of sight, the line-integrals have to be calculated for the given parameterization of $n_e(\rho_{pol})$. Basically, there are two methods.

6.3.1 Discrete summation

One approach is to assume that ρ_{pol} is constant between two points and its value is equal to the arithmetic mean $(\rho_{Hc,i} + \rho_{Hc,i+1})/2$ of the two neighboring points. Then, the line integral can be discretized by

$$\int_{Hc} n_e(\rho_{pol}(x))\, dx \;\doteq\; d_{Hc} \sum_{i=1}^{N-1} n_e\left(\frac{\rho_{Hc,i} + \rho_{Hc,i+1}}{2}\right), \tag{6.2}$$

where the variable of integration x is the coordinate along the line of sight and the integral subscript Hc denotes that integration is performed along the line of sight of the c^{th} interferometer channel. This method is appropriate when n_e does not change much on the scale length of d_{Hc}.
In the next step, equation (6.1) shall be inserted into (6.2). This is not trivial as the function $n_e(\rho_{pol})$ is defined in sections. The $\rho_{pol} > \rho_{lim}$ section does not contribute to the line integral as the density is equal to zero in this region according to the ansatz. The two remaining sections, however, require individual treatment. For easier illustration, we

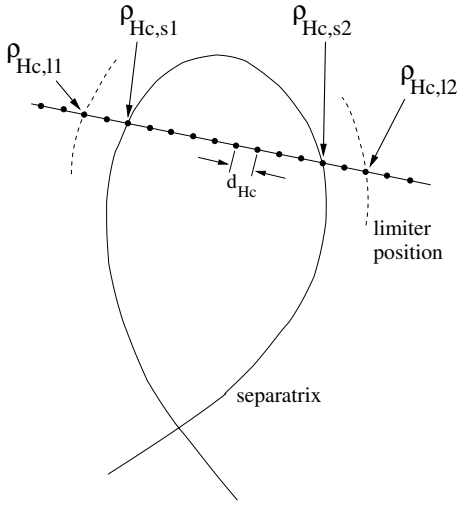

Figure 6.3: *The regions $\rho_{pol} \leq 1$, $1 < \rho_{pol} \leq \rho_{lim}$ and $\rho_{pol} > \rho_{lim}$ have to be distinguished. For simplicity, we assume that the intersection between the line of sight and the separatrix/limiter position coincides with grid lines of the ρ_{pol} grid. The corresponding indices are labeled $s1/s2$ and $l1/l2$, respectively.*

assume that the coordinates of the points where the line of sight intersects the separatrix and the limiter position, coincide with the grid lines of the 69×39 grid (see figure 6.3). In this case, two indices $s1$ and $s2$ exist, so that $\rho_{Hc,s1} = 1$ and $\rho_{Hc,s2} = 1$, and two indices $l1$, $l2$ with $\rho_{Hc,l1} = \rho_{Hc,l2} = \rho_{lim}$. In practice, this is usually not fulfilled, so a further step of linear interpolation is required to determine the intersections with separatrix and limiter.
But with this simplification, equation (6.1) can be inserted into (6.2), yielding:

$$\int_{Hc} n_e(\rho_{pol}(x))\,dx = \int_{\rho_{pol}\leq 1} n_e(\rho_{pol}(x))\,dx + \int_{1<\rho_{pol}\leq\rho_{lim}} n_e(\rho_{pol}(x))\,dx \doteq$$

$$\doteq d_{Hc} \sum_{i=s1}^{s2-1} \sum_{k=1}^{M} a_k\, f_k\left(\frac{\rho_{Hc,i}+\rho_{Hc,i+1}}{2}\right) +$$

$$+ d_{Hc}\left(\sum_{i=l1}^{s1-1} g\left(\frac{\rho_{Hc,i}+\rho_{Hc,i+1}}{2}\right) + \sum_{i=s2}^{l2-1} g\left(\frac{\rho_{Hc,i}+\rho_{Hc,i+1}}{2}\right)\right) \sum_{k=1}^{M} a_k\, f_k(1)$$

By introducing the expression

$$\beta_{Hc,k} := d_{Hc}\left(\sum_{i=s1}^{s2-1} f_k\left(\frac{\rho_{Hc,i}+\rho_{Hc,i+1}}{2}\right) + f_k(1)\sum_{i=l1}^{s1-1} g\left(\frac{\rho_{Hc,i}+\rho_{Hc,i+1}}{2}\right) + \right.$$

$$\left. + f_k(1)\sum_{i=s2}^{l2-1} g\left(\frac{\rho_{Hc,i}+\rho_{Hc,i+1}}{2}\right)\right), \qquad (6.3)$$

this result simplifies to:

$$\int_{Hc} n_e(\rho_{pol}(x))\, dx \;=\; \sum_{k=1}^{M} a_k\, \beta_{Hc,k}\;. \tag{6.4}$$

6.3.2 Linear interpolation

Alternatively, $\rho_{pol}(x)$ can be assumed to be linear between $x = x_i$ and $x = x_{i+1}$, i.e. for every interval $[x_i, x_{i+1}]$ two numbers m_i and t_i exist[1] so that

$$\rho_{pol}(x)|_{x_i \le x \le x_{i+1}} \;=\; m_i x + t_i\;. \tag{6.5}$$

Then, the discretization of the integral is

$$\int_{Hc} n_e(\rho_{pol}(x))\, dx \;\doteq\; \sum_{i=1}^{N-1} \int_{x_i}^{x_{i+1}} n_e(m_i x + t_i)\, dx \;=\; \sum_{i=1}^{N-1} \frac{1}{m_i} \int_{\rho_{Hc,i}}^{\rho_{Hc,i+1}} n_e(\rho)\, d\rho\;, \tag{6.6}$$

where the substitution $\rho = m_i x + t_i$ was made. In the case $\rho_{Hc,i} \;=\; \rho_{Hc,i+1}$, which can occur when ρ_{pol} has its minimum between the two points, the coefficient m_i is equal to zero and this method fails. Already when m_i is only close to zero, this procedure may become numerically unstable. In a computer algorithm, this situation has to be detected automatically and the previously described method of discrete summation has to be applied instead.
Inserting equation (6.1) into (6.6) yields the same result (equation (6.4)) as in the case before, just the definition of $\beta_{Hc,k}$ has to be replaced by

$$\begin{aligned}\beta_{Hc,k} \;:=\; \sum_{i=s1}^{s2-1} \frac{1}{m_i} \int_{\rho_{Hc,i}}^{\rho_{Hc,i+1}} f_k(\rho)\, d\rho \;+\; \Bigg(\sum_{i=l1}^{s1-1} \frac{1}{m_i} \int_{\rho_{Hc,i}}^{\rho_{Hc,i+1}} g(\rho)\, d\rho \;+ \\ + \sum_{i=s2}^{l2-1} \int_{\rho_{Hc,i}}^{\rho_{Hc,i+1}} g(\rho)\, d\rho \Bigg) \cdot f_k(1)\;.\end{aligned} \tag{6.7}$$

It should be noticed that the $\beta_{Hc,k}$'s can be calculated from the data of the magnetic diagnostic alone. Therefore, equation (6.4) gives the desired interrelation between the magnetic data, the density profile coefficients $a_1, \ldots, a_M$ and the line-integrals measured by the interferometer. The remaining problem is to solve this equation system with respect to $a_1, \ldots, a_M$.

6.4 Calculation of the profile coefficients

Two different methods of solving equation (6.4) will be discussed. The line integrals measured by the DCN interferometer will be labeled L_{Hc}, $c \in \{1, ..., 5\}$.

[1] One easily finds that $m_i = \frac{\rho_{Hc,i+1} - \rho_{Hc,i}}{d_{Hc}}$ and $t_i = \rho_{Hc,i} - x_i \cdot \frac{\rho_{Hc,i+1} - \rho_{Hc,i}}{d_{Hc}}$.

6.4.1 Direct analytical solution

For real-time application, it is desirable to have an algorithm that does not consume much computing power. Therefore, the direct analytical solution of the problem is the first option to be tested. In order to have a unique solution, the number of free parameters has to be equal to the number of measured values. The analytical solution does not take into account measurement errors, so the measured line integrals L_{Hc} are set equal to the left-hand side of equation (6.4), i.e.:

$$L_{Hc} = \sum_{k=1}^{M} a_k \, \beta_{Hc,k} \; .$$

As there are 5 lines of sight, a unique analytical solution requires that the number of basis functions is also 5. In that case, the $\beta_{Hc,k}$'s form a 5×5 matrix and the equation system looks like this:

$$\begin{pmatrix} L_{H1} \\ L_{H2} \\ L_{H3} \\ L_{H4} \\ L_{H5} \end{pmatrix} = \begin{pmatrix} \beta_{H1,1} & \beta_{H1,2} & \beta_{H1,3} & \beta_{H1,4} & \beta_{H1,5} \\ \beta_{H2,1} & \beta_{H2,2} & \beta_{H2,3} & \beta_{H2,4} & \beta_{H2,5} \\ \beta_{H3,1} & \beta_{H3,2} & \beta_{H3,3} & \beta_{H3,4} & \beta_{H3,5} \\ \beta_{H4,1} & \beta_{H4,2} & \beta_{H4,3} & \beta_{H4,4} & \beta_{H4,5} \\ \beta_{H5,1} & \beta_{H5,2} & \beta_{H5,3} & \beta_{H5,4} & \beta_{H5,5} \end{pmatrix} \cdot \begin{pmatrix} a_1 \\ a_2 \\ a_3 \\ a_4 \\ a_5 \end{pmatrix} \tag{6.8}$$

To calculate the vector that contains the coefficients a_k, one only has to invert the matrix and multiply it by the vector with the 5 measured DCN line integrals. As the inversion of a 5×5 matrix and a matrix-vector-multiplication do not require much computing power, this approach is a candidate for real-time application.
However, one has to be aware that for the given DCN configuration, the lines of sight of the channels H-2 and H-3 are situated almost symmetrically around the magnetic axis (compare figure 6.1), so the line-integrated densities measured by them are usually very similar. Therefore, the attempt to extract information from both, H-2 and H-3, individually would make the result unstable as any small difference between these channels would have strong impact on the calculated profile. From the numerical point of view, this is equivalent to a poor condition number of the matrix. This problem can be avoided by using only the sum of L_{H2} and L_{H3} as input parameter. Accordingly, the number of basis functions has to be reduced to 4 in that case to have a unique solution:

$$\begin{pmatrix} L_{H1} \\ L_{H2} + L_{H3} \\ L_{H4} \\ L_{H5} \end{pmatrix} = \begin{pmatrix} \beta_{H1,1} & \beta_{H1,2} & \beta_{H1,3} & \beta_{H1,4} \\ \beta_{H2,1} + \beta_{H3,1} & \beta_{H2,2} + \beta_{H3,2} & \beta_{H2,3} + \beta_{H3,3} & \beta_{H2,4} + \beta_{H3,4} \\ \beta_{H4,1} & \beta_{H4,2} & \beta_{H4,3} & \beta_{H4,4} \\ \beta_{H5,1} & \beta_{H5,2} & \beta_{H5,3} & \beta_{H5,4} \end{pmatrix} \cdot \begin{pmatrix} a_1 \\ a_2 \\ a_3 \\ a_4 \end{pmatrix}$$

Of course, further reduction of the number of free parameters to 3 or 2 is possible.

6.4.2 Least squares approximation

In contrast to the analytical solution, which precisely reproduces the measured line integrals, this approach includes stochastic measurement errors ϵ_c with standard deviation σ_c and

delivers a density profile that is best consistent with the measurements. The measured line integrals are again labeled L_{Hc}, $c \in \{1, ..., 5\}$. Then we have

$$L_{Hc} \;=\; \int\limits_{Hc} n_e(\rho_{pol}(x))\; dx \;+\; \epsilon_c \;. \tag{6.9}$$

Inserting equation (6.4) for the integral and solving with respect to ϵ_c yields:

$$\epsilon_c \;=\; L_{Hc} \;-\; \sum_{k=1}^{M} a_k\, \beta_{Hc,k} \;.$$

Now, χ^2 is defined as the sum of the squares of the errors, normalized to the standard deviation:

$$\chi^2 \;=\; \sum_{c=1}^{5} \frac{\left(L_{Hc} \;-\; \sum\limits_{k=1}^{M} a_k\, \beta_{Hc,k}\right)^2}{\sigma_c^2} \tag{6.10}$$

The profile that agrees best with the measurements minimizes this χ^2. A necessary condition for that requires the partial derivatives with respect to the profile parameters to vanish, i.e.

$$\frac{\partial \chi^2}{\partial a_j} \;=\; 2 \sum_{c=1}^{5} \frac{\left(L_{Hc} \;-\; \sum\limits_{k=1}^{M} a_k\, \beta_{Hc,k}\right)(-\beta_{Hc,j})}{\sigma_c^2} \;\stackrel{!}{=}\; 0 \quad \forall j \in \{1, \ldots, M\} \tag{6.11}$$

There are M unknown coefficients and M equations, independent of the actual number of interferometer channels. So it is possible to have less than 5 basis functions and use all 5 measured line-integrals individually, in contrast to the analytical solution, where the sum of some channels has to be used.
It is helpful to introduce matrix notation again. The 5-vector $\vec{l}$ and the M-vector $\vec{a}$ are defined as

$$(\vec{l})_c = L_{Hc} \quad \text{and} \quad (\vec{a})_k = a_k \;.$$

Moreover, the $5 \times M$ matrix B and the $M \times 5$ matrix Γ are defined as

$$(B)_{c\,k} \;=\; \beta_{Hc,k} \quad \text{and} \quad (\Gamma)_{j\,c} = \frac{\beta_{Hc,j}}{\sigma_c^2} \;.$$

Then, all M equations in (6.11) can be put into one matrix-vector-equation:

$$\Gamma \cdot \left(\vec{l} \;-\; B \cdot \vec{a}\right) \;=\; \vec{0}$$

In the case $M = 5$, it can be easily seen that the analytical solution trivially fulfills this equation independent of Γ (and therefore independent of σ_c) as it makes the expression in the brackets vanish. Also the case $M > 5$ is possible, however, then the problem will be under-determined as there is a single- or multidimensional set of coefficient vectors $\vec{a}$ for which the expression is equal to zero. The case of interest therefore is $M < 5$, where it is in general not possible to find a vector $\vec{a}$ such that the expression in the brackets vanishes. The problem can be solved by

$$\vec{a} \;=\; (\Gamma \cdot B)^{-1} \cdot \Gamma \cdot \vec{l} \,.$$

It is worth mentioning that this equation is also applicable to the case $M = 5$. Then, B and Γ are square matrices, so the identity $(\Gamma \cdot B)^{-1} = B^{-1} \cdot \Gamma^{-1}$ holds and one gets $\vec{a} = B^{-1} \cdot \vec{l}$, which is, once again, the analytical solution. For $M > 5$, however, $(\Gamma \cdot B)$ will be singular and the attempt to invert it will fail.

6.5 Comparison of various methods

As described in the previous sections, there are several methods of calculating a profile with a simple, real-time compatible algorithm. Mainly three choices have to be made (which are not fully independent of each other):

- The method of calculation (analytical/least squares approximation)
- The basis functions
- The number of free parameters

Depending on these three choices, a density profile will be obtained that provides a more or less accurate description of the actual plasma density. The next step therefore is to test several methods of profile calculation and to assess the quality of the results by comparing them to a reference profile which is expected to represent the actual profile shape with high accuracy. On ASDEX Upgrade, a density profile is calculated offline by Integrated Data Analysis (in short: IDA), which is based on the output of two diagnostics: Not only the data from the DCN interferometer is used, but also the data from lithium beam impact excitation spectroscopy. The IDA approach uses a probabilistic ansatz to calculate the density profile from the measurements of these two diagnostics. Taking into account the error distribution functions of the involved diagnostics, a profile, which is given as a spline function, is calculated such that the resulting set of spline coefficients maximizes the likelihood of obtaining the actual measurement results. In the edge region, the resulting profile is mainly determined by the local measurements of the lithium beam diagnostic, which cannot penetrate much deeper into the plasma than to the separatrix position due to beam attenuation, whereas the results for the core region do mainly rely on the line-integrated measurements by the interferometer. At the present, the IDA profiles state the most precise density profiles that are available on ASDEX Upgrade. For at least three reasons, the profiles calculated by the real-time algorithm which is presented here, will not be able to reach the same level of precision as IDA:

- Only magnetic equilibria that are calculated via functional parameterization can be used for real-time applications. The IDA approach as an offline diagnostic, however, uses equilibria which are calculated after the end of the plasma discharge and are closer to the actual solution of the Grad-Shafranov equation.
- The real-time algorithm has to exclusively rely on the 5 line-integrated measurements provided by the DCN interferometer, but cannot use the data from the lithium beam diagnostic. The latter is, on the one hand, not yet technically designed for real-time transfer of measured data, and on the other hand, it does not provide a continuous measurement. The lithium beam is pulsed, with a duty cycle of approximately 70% and a period of 80 ms. Therefore, there are time intervals with a length of about

24 ms during which no measurement is available. This is not acceptable when the density profiles are meant to be used for feedback control.

- The real-time calculation has to take less time than one cycle of the feedback control system of the experiment, which is of the order of 1 millisecond. Therefore, the CPU speed of the available computers sets an upper limit to the complexity of the algorithm.

In the following subsections, the results of two real-time approaches will be compared to the IDA reference profiles. The discussion will start with the analytical solution.

6.5.1 Analytical method

For the analytical solution, the number of free parameters has to be equal to the number of measured values. The upper limit to the number of basis functions is therefore five. However, due to the previously described symmetry between the lines of sight of H-2 and H-3, this would give very unstable results. If, for example, H-2 is a tangent to the flux surface $\rho_{pol} = 0.4$, i.e. crosses all flux surfaces with larger flux radius and does not penetrate into regions with lower ρ_{pol}, and H-3 is a tangent to the $\rho_{pol} = 0.41$ surface, then a small difference in the two measured line-integrated densities (e.g. due to measurement inaccuracies) will have enormous impact on the reconstructed profile in the interval $\rho_{pol} \in [0.4; 0.41]$. In the case that the H-2 signal is higher, an irrationally high density will be reconstructed for this interval. Therefore, a reduction of the number of free parameters is required, which is achieved by including only the sum of some interferometer channels into the calculation. As a profile with only one free parameter would not be capable of describing any spatial distribution of density, calculations with 2, 3 and 4 parameters have been performed. Simple polynomials have been used as the basis functions, whereby the linear term must be zero in order to fulfill the boundary condition at $\rho_{pol} = 0$ given in section (6.2.1). For first studies, profiles have been calculated for ASDEX Upgrade discharge #22863, which is characterized by the occurrence of central density peaking around t = 1.65 s. This drives the discharge unstable, and at t = 1.75 s, the interferometer suffers from the first fringe jump (see figure 6.4), so that profile calculation has to be stopped there. As the density profile evolves from a rather flat H-mode profile towards a peaked profile between t = 1.0 s and t = 1.65 s, a variety of different profile shapes is available in this time interval. Density profiles with two, three and four free parameters have been calculated analytically, whereby an exponential decay of density in the scrape-off layer was assumed, with the decay length being 1/5 of the separatrix-limiter distance. Accordingly, the function $g(\rho_{pol})$ in equation (6.1) was set to

$$g(\rho_{pol}) = e^{-5\frac{\rho_{pol}{}^{-1}}{\rho_{lim}{}^{-1}}} .$$

The following table gives the basis functions and the interferometer channels[2] that were used.

number of parameters	basis functions	interferometer channels used
2	1, ρ^2	H1+H2+H3, H4+H5
3	1, ρ^2, ρ^3	H1, H2+H3, H4+H5
4	1, ρ^2, ρ^3, ρ^4	H1, H2+H3, H4, H5

[2] To avoid confusion with a minus sign, the interferometer channel labels will be written without the dash whenever they appear in a sum, e.g. 'H1' instead of 'H-1'.

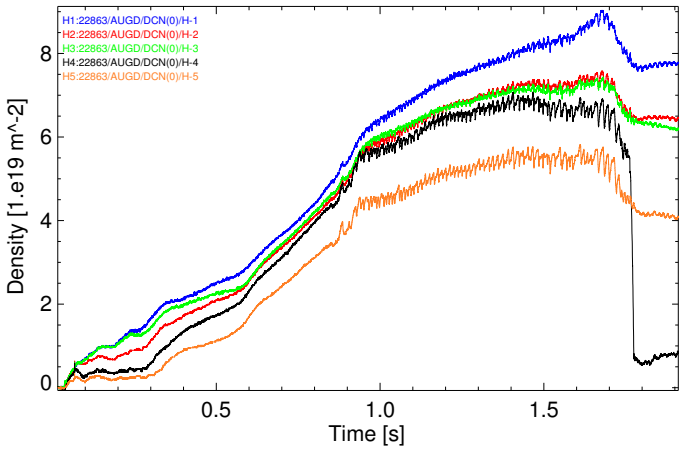

Figure 6.4: *Time traces for the 5 DCN interferometer channels for discharge #22863. The total duration of the discharge is about 5 seconds. This plot, however, stops shortly after the first fringe jump. The rise of the core channel H1 (blue curve) between t = 1.5 and 1.7 s indicates central density peaking.*

Figure 6.5 compares these profiles to the IDA reference for different time slices. Apparently, the profile with two free parameters is only a good description as long as the actual density profile is flat, but as central peaking occurs, it fails to properly depict this development. The resulting density for the core region is much lower than that calculated by IDA especially at t = 1.71 s. Therefore, the 2-parameter profile is not adequate to describe peaked profiles and will in general not be useful. The 3-parameter profile, however, can also describe the peaked profile. Among the 3 candidates, it provides the best approximation to the IDA reference. Its main weakness is the tendency to reconstruct an increase of density between $\rho_{pol} = 0.8$ and 1 (as can be seen at t = 1.5 s, 1.59 s and 1.71 s). The profile with 4 free parameters exhibits the same problem in the edge region in a much more pronounced way. As the line integrals measured by the interferometer channels H-4 and H-5 have to be individually matched here (whereas only the sum of both is used for 2- and 3-parameter profiles), a similar problem as in the case of H-2 and H-3 occurs: H-4 and H-5 do both probe the edge region of the plasma, so a certain amount of symmetry between them exists. Again, a small change in one of these signals can strongly influence the shape of the analytically calculated profile.

To sum up, among the analytically calculated profiles, only the variant with 3 free parameters provides useful results. This can be understood from the interferometer geometry: One channel (H-1) probes the plasma center, two channels (H-4 and H-5) probe the edge, and two channels (H-2 and H-3) are situated in between and usually reach a minimum ρ_{pol} of about 0.4. So effectively, there are just three different line integrals measured, and an analytical solution will therefore provide best results when it has just this number of free parameters. Using less degrees of freedom results in loss of information, using more yields a somewhat under-determined solution which may oscillate.

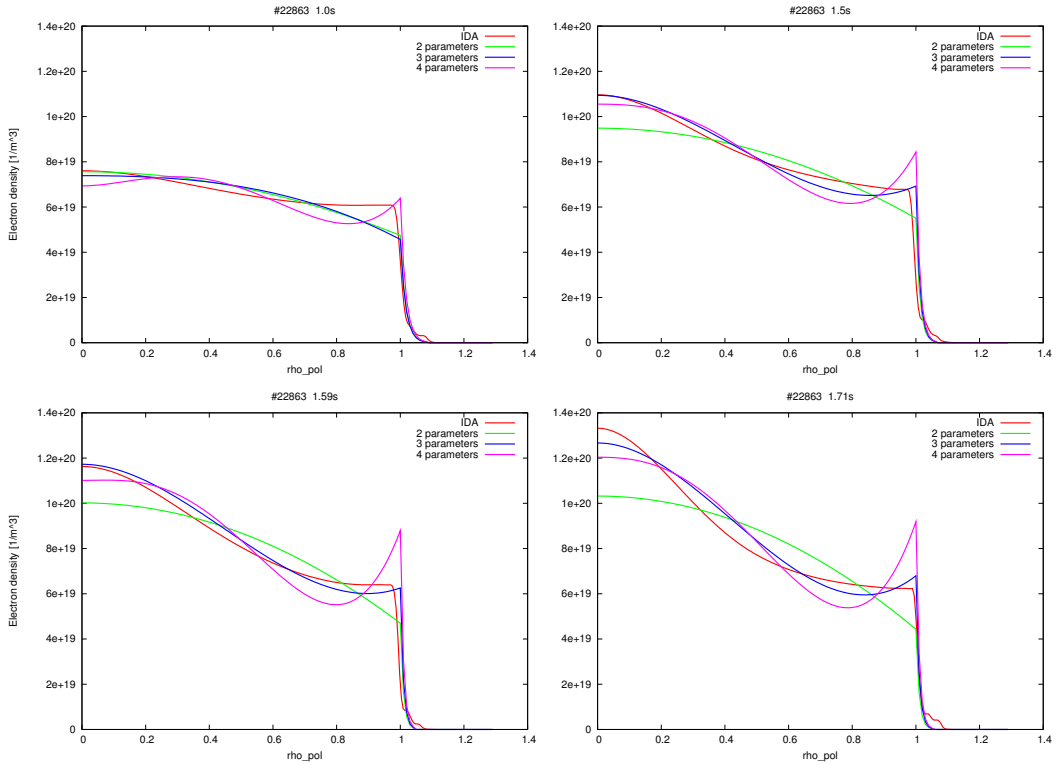

Figure 6.5: *Density profiles for discharge #22863 at t = 1.0 s (top left), 1.5 s (top right), 1.59 s (bottom left) and 1.71 s (bottom right). The curves represent the IDA profile and the results from analytical solution with 2, 3 and 4 free parameters.*

6.5.2 Least squares method

In contrast to the analytical method, the least squares approach can handle a number of measured values that is larger than the number of free parameters. As shown earlier, it is identical to the analytical solution when both numbers are equal. For this reason, a maximum of 4 free parameters will be studied. On the other hand, as illustrated in the previous section, the use of only 2 degrees of freedom results in a loss of information, so the minimum number will be 3.
Figure 6.6 compares profiles obtained by least squares approximation, using 3 and 4 free parameters, respectively, to the IDA profiles of discharge #22863. In addition, the analytical solution with 3 free parameters is shown again. Both profiles with 3 free parameters are rather similar, however, the least squares solution is a bit closer to the IDA profile when the density distribution is flat. The 4-parameter profile is well consistent with the peaked profile at t = 1.71 s, especially the core density is closer to the IDA value than for the two 3-parameter profiles. However, in case of the flat profile at t = 1.0 s, it fails to provide a reasonable description of the density distribution. Like in case of the analytically calculated profile with 4 free parameters, an increase of density is calculated towards the separatrix, which does not represent the actual density characteristics there. This finally confirms the conclusion of the previous section: Effectively, there are line-integrated measurements from 3 different regions of the plasma, so using 3 free parameters is the best choice.
It is favorable to calculate a 3-parameter profile via least squares approximation and not

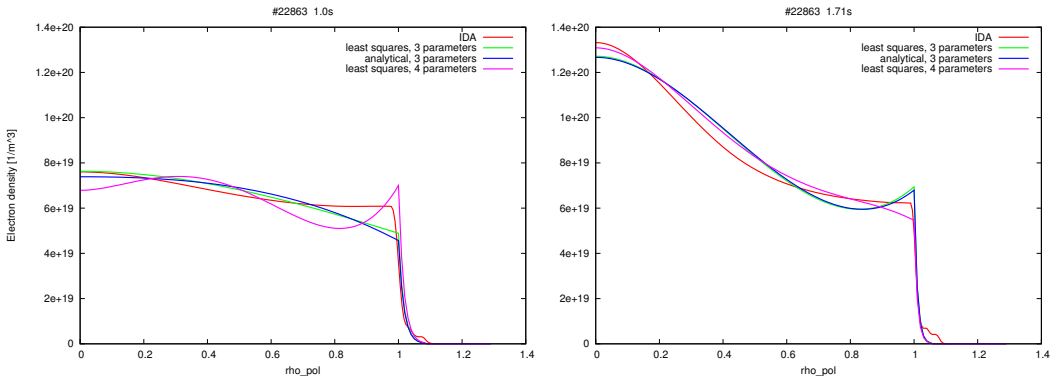

Figure 6.6: *Density profiles for discharge #22863 at t = 1.0 s (left) and 1.71 s (right). The curves represent the IDA profile, the results from analytical solution with 3 free parameters, and from least squares approximation with 3 and 4 parameters.*

analytically, as the analytical solution puts the lines of sight into 3 groups (H1, H2+H3 and H4+H5), which is reasonable due to the given geometry, but may bias the result by giving H-1 a higher weight than any of the 4 other channels. The least squares method is preferable as it treats all 5 channels in a fully equal way.
The profile obtained by using the basis functions 1, ρ^2 and ρ^3, however, does not provide a satisfying description of the density in the interval $[0.8; 1]$ if the profile is peaked (see right diagram in figure 6.6). There is an increase of density in this interval, which is not consistent with IDA. This is due to the properties of the basis functions ρ^2 and ρ^3. When the coefficients in front of those functions have different sign, the square term dominates for small ρ which allows for a convex curvature in the core region. In the edge region, however, the cubic term becomes dominant. This allows for concave curvature, which is necessary to describe a peaked profile. However, in the region $0.8 < \rho_{pol} \leq 1$ this curvature is so strong that the graph of the resulting function starts rising again. To solve this problem, it is therefore necessary to replace the basis function ρ^3 by a different function which is similar in the interval $[0; 0.8]$, but has a smaller second derivative in $[0.8; 1]$. For this purpose, a 4^{th} degree polynomial without linear term has been fitted to the IDA profile for discharge #22863 at t = 1.71 s, i.e. a peaked profile which is not well described by the present basis functions. The result for $\rho \in [0; 1]$ is:

$$n_{e\,fit}(\rho)\ /m^{-3} = 1.35 \cdot 10^{20} - 6.18 \cdot 10^{20}\rho^2 + 9.9 \cdot 10^{20}\rho^3 - 4.47 \cdot 10^{20}\rho^4$$

As 1 and ρ^2 are basis functions anyway, only the last two terms are of interest. As the third basis function, a linear combination of ρ^3 and ρ^4 is introduced, where the ratio of the pre-factors is given by the above term. The third basis function therefore is

$$f_3(\rho) = 2.21\,\rho^3 - \rho^4\ .$$

The effect of using this basis function instead of ρ^3 is illustrated in figure 6.7. There is no significant difference for flat profiles, but in case of central peaking, the increase of density in the edge region is avoided. It is interesting to compare the left diagram in figure 6.7 to the left diagram in figure 6.6. In the latter case, 4 free parameters and the basis functions 1, ρ^2, ρ^3 and ρ^4 have been used, which means that the resulting set of possible profiles just

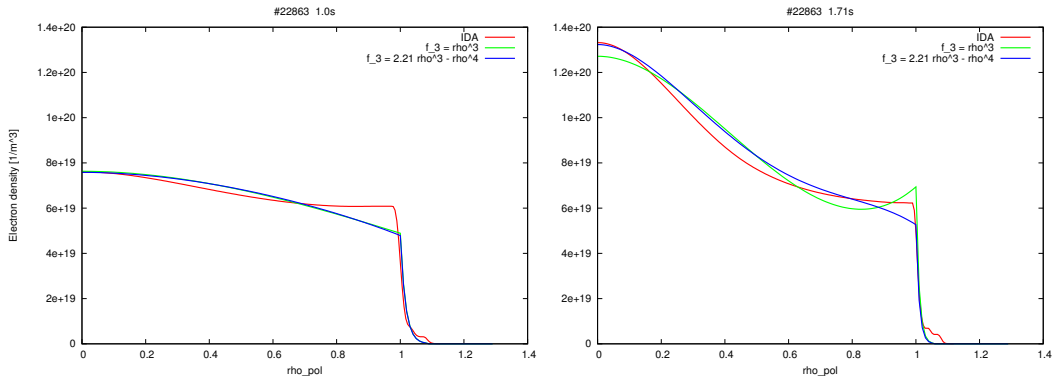

Figure 6.7: *Illustration of the effect of replacing the third basis function* $f_3 = \rho^3$ *by the function* $f_3 = 2.21\rho^3 - \rho^4$*. The least squares approximation algorithm yields the green curve in the first case and the blue one in the latter case. For a flat profile (*$t = 1.0\,s$*, left), there is almost no difference, whereas for a peaked profile (*$t = 1.71\,s$*, right), the rise of density from* $\rho = 0.8$ *to* $\rho = 1.0$ *is avoided.*

contains as a subset those profiles that can be obtained with the newly introduced basis functions. Nevertheless, the approach with the new basis functions provides a reasonable description of the density distribution, whereas the 4-parameter profile shows considerable oscillations. Here, once again, it can be seen that it is beneficial to reduce the number of degrees of freedom from 4 to 3.

So far, the results of the proposed real-time algorithm and the IDA profiles have only been compared for some discrete time slices of a discharge. In order to more reliably assess the quality of the results provided by the new algorithm, it is desirable to compare a large number of time slices. For this purpose, it is helpful to choose a certain value of ρ_{pol} and calculate the temporal evolution of the local density at this flux surface from both, real-time and IDA profile. The correlation between them indicates the level of agreement between the two profiles for the chosen region. Figure 6.8 shows the time trace of the density at the magnetic axis ($\rho_{pol} = 0$) for discharge #22863. The density calculated from the real-time profile is shown as solid line, as this measurement is always available, whereas the values calculated from the IDA profile are shown as crosses, so that the gaps during which the lithium beam is switched off become apparent. Up to about t = 0.6 s, the density calculated by IDA shows considerable oscillations, which can be explained by the fact that neither the used magnetic equilibrium (which differs from that for the real-time method) nor the lithium beam diagnostic provide stable results during the early plasma ramp-up phase. But apart from that, the results are in good agreement.

According to this diagram, the core density reaches a maximum of a bit more than $1.4 \cdot 10^{20}\,m^{-3}$ around t = 1.7 s. The discharge was heated with electron cyclotron resonance heating in the time interval of interest. For the given frequency of 140 GHz and the chosen polarization, the cut-off-density for the microwave beam is about $1.25 \cdot 10^{20}\,m^{-3}$. At this density, the phase velocity of the electromagnetic wave goes to zero, so it can not penetrate deeper into the plasma, but is reflected. For this reason, a significant amount of back-reflected ECRH power is expected to occur around t = 1.7 s if the density reconstruction

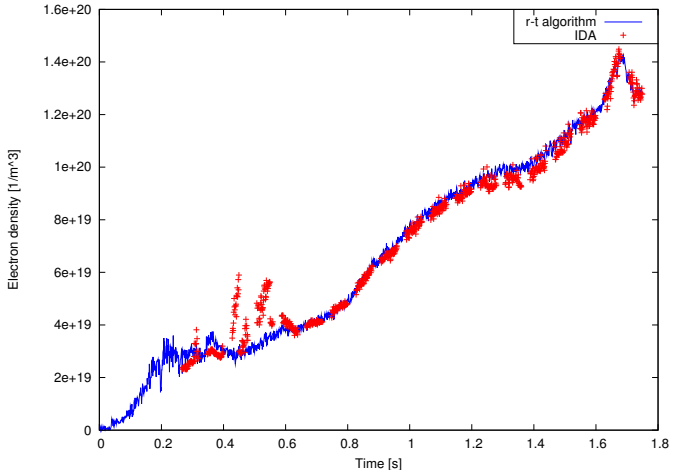

Figure 6.8: *Comparison of the local electron density at $\rho_{pol} = 0$ as derived from the profile provided by the real-time algorithm and the IDA profile. The time scale ends close before the first fringe jump.*

is correct. The ECE diagnostic on ASDEX Upgrade is equipped with a detector that is designed for detecting backscattered ECRH power and acts as an interlock for the heating system if a certain level of power reflection is exceeded. In figure 6.9, this signal is shown together with the core density reconstructed by the 3-parameter profile which was obtained by least squares approximation. It can be seen that the rise of core density above the cut-off level is indeed correlated to a measurable amount of back-reflected ECRH power. This is an independent proof that the reconstructed core density is correct.
As the two diagrams in figure 6.7 show, the IDA profile and the real-time profile mainly deviate in the edge region. Figure 6.10 compares the two density profiles for two other discharges. In the right diagram, IDA reconstructs a higher density at the edge, and accordingly a lower density in the center, as it has to match the same line-integrated measurements as the real-time algorithm. The increased deviation at the edge is due to the fact the IDA algorithm additionally uses the data from the lithium beam diagnostic, which probes the plasma edge. Therefore, the agreement between real-time profiles and IDA is in general better in the inner region of the plasma, where both methods have to rely on the data from the DCN interferometer. However, one has to keep in mind that for a typical plasma configuration, the line of sight of channel H-1 does not cross the magnetic axis (compare figure 6.1), but usually only reaches a minimum ρ_{pol} of the order of 0.2. Therefore, the DCN interferometer does not provide any measurement in the $0 \leq \rho_{pol} < 0.2$ range and the density profiles in this interval do only state an extrapolation. Thus, also in the innermost region of the plasma, a higher level of deviation between the profiles can be observed in some cases. The IDA algorithm is usually run with a monotonicity condition, i.e. the reconstructed $n_e(\rho_{pol})$ is always monotonously decreasing. The real-time algorithm does not include such condition. Therefore, clear deviation in the center is expected density profiles become hollow, which can occur in low-density plasmas with strong central electron heating.

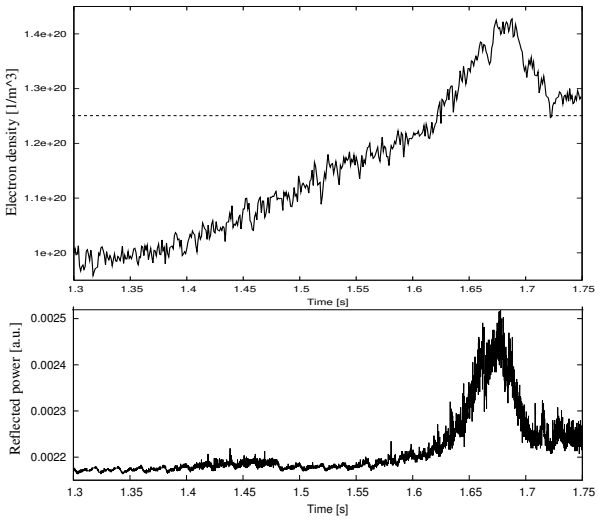

Figure 6.9: *Correlation between the core density reconstructed by the real-time algorithm (upper graph, the dashed line gives the cutoff density) and the backscattered ECRH power in discharge #22863.*

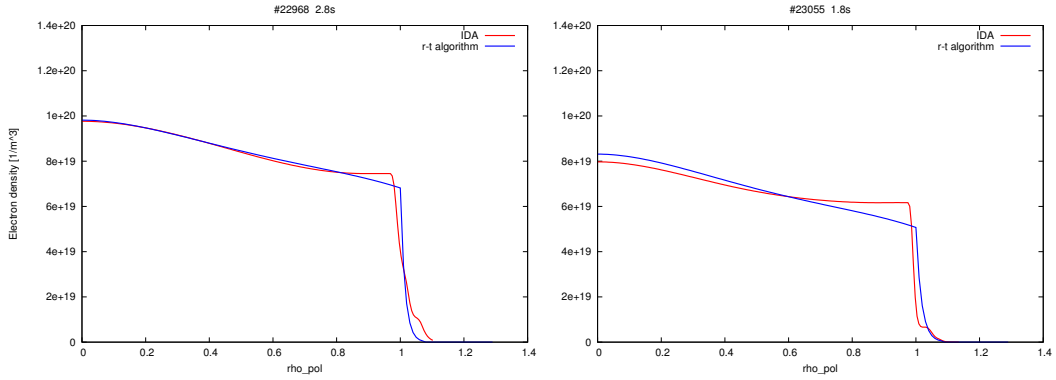

Figure 6.10: *Comparison of the IDA profile and the profile provided by the real-time algorithm for discharge #22968 at $t = 2.8\,s$ (left) and #23055 at $1.8\,s$ (right).*

6.6 Impact of fringe jumps

For the studies performed so far, discharges and time intervals have been chosen manually in which no fringe jumps occur, so that the line-integrated densities provided by the interferometer represent the actual values. As discussed in previous chapters, it may happen that one or several measured line-integrals are affected by an error that is an integer multiple of $0.572\ 10^{19}\,m^{-2}$. The impact of such events on the resulting profile will now be investigated. The fact that the lines of sight of the interferometer channels H-2 and H-3 are situated symmetrically around the plasma center, provides some redundancy. The same holds for the edge channels H-4 and H-5. Regarding the core density, however, only interferometer channel H-1 provides information. Therefore, a fringe jump on channel H-1 has the most severe impact on the profile, whereas a fringe jump e.g. on H-2 is partially

compensated by H-3. In the following example, the influence of a simulated jump on H-1 is tested as a function of the number of fringes that are lost. Figure 6.11 shows the density profile for discharge #22863 at t = 1.0 s, which is a rather flat H-mode profile. In addition, those density profiles are shown which result if the H-1 density is artificially changed by 1 or 2 fringes.

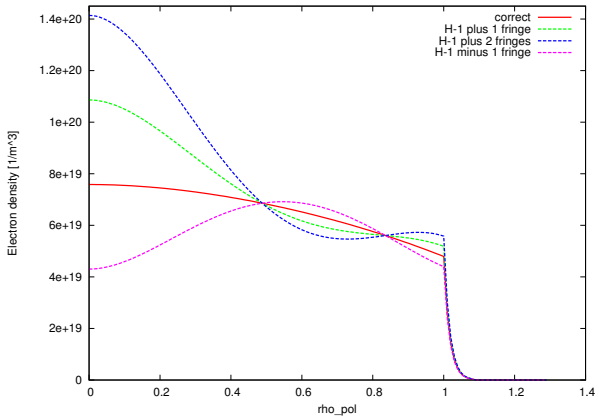

Figure 6.11: *Impact of fringe jumps on the density profile. The solid curve represents the profile for discharge #22863 at t = 1.0 s. The dashed curves have been obtained by shifting the H-1 density by ±1 or +2 fringes, respectively.*

This demonstrates that the loss of 2 fringes dramatically distorts the profile, but already the loss of only 1 fringe significantly influences conclusions e.g. on central density peaking that are drawn from the profile. A shift by -1 fringe makes the profile appear hollow, whereas a shift by +1 fringe results in a peaked profile which is very similar to the one that actually occurs a few hundred milliseconds later in that discharge. It should be emphasized that in this example, the total density is on a rather high level, so that one fringe corresponds to a relative change of the measured density by about 9%. For low-density discharges, the impact on the profile will be even more severe. Therefore, the conclusion is that profile calculation is very sensitive to spurious density signals due to fringe jumps. On the important core channel H-1, not even the loss of 1 fringe is tolerable when an indicator for central density peaking is meant to be extracted from the profile. For this reason, it is important to use only validated density signals for real-time application (see chapter 5).

6.7 Definition of a peaking parameter

The aim of this thesis work is to demonstrate feedback control of the shape of the density profile on ASDEX Upgrade. As this will be relevant for the fusion performance of next-step devices, the focus will be on the amount of density peaking in the plasma center. For feedback experiments, it is therefore desirable to have a scalar parameter which measures the peakedness of the profile. There are several ways of deriving such peaking parameter from the calculated density profile. Here, the density profile will be integrated in the intervals $0 \leq \rho_{pol} \leq 0.4$ and $0.6 \leq \rho_{pol} \leq 1$, as figure 6.12 illustrates. The difference between those

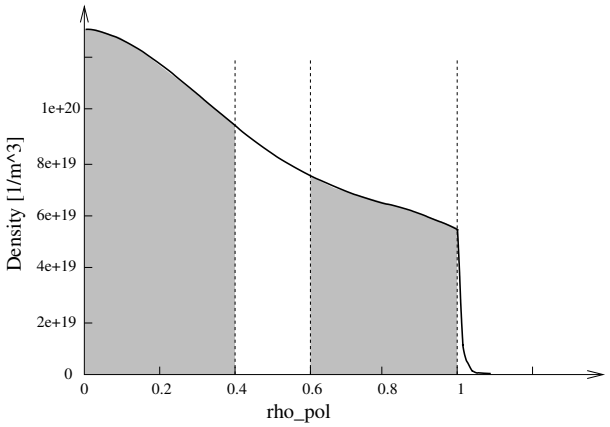

Figure 6.12: *The density profile is integrated in the intervals* $[0; 0.4]$ *and* $[0.6; 1]$.

two integrals can be used as peaking parameter:

$$p_1 = \int_0^{0.4} n_e(\rho_{pol})\ d\rho_{pol} - \int_{0.6}^{1.0} n_e(\rho_{pol})\ d\rho_{pol} \tag{6.12}$$

This peaking parameter has the dimension of a density. It is equal to zero for a flat profile and positive for a peaked profile. This parameter scales with the absolute density, i.e. it increases when the shape of the profile is kept fixed but the total density rises.
In contrast, a dimensionless peaking parameter which does not depend on the absolute density can be obtained by normalizing to the total density:

$$p_2 = \frac{\int_0^{0.4} n_e(\rho_{pol})\ d\rho_{pol} - \int_{0.6}^{1.0} n_e(\rho_{pol})\ d\rho_{pol}}{\int_0^1 n_e(\rho_{pol})\ d\rho_{pol}} \tag{6.13}$$

Evidently, this parameter is undefined when the plasma density is equal to zero. Therefore, its calculation can only start when a certain minimum density has been reached in the ramp-up phase of the discharge.
Those peaking parameters are very convenient for real-time application as the real-time density profile in the interval $0 \leq \rho_{pol} \leq 1$ is given as a polynomial which is trivial to integrate. Therefore, the calculation of the peaking parameters does not consume much computing power.
It should be mentioned that in the literature, different peaking parameters can be found, like the ratio of central density and volume-averaged density, $n_e(0)/\langle n_e \rangle_{vol}$. As illustrated in the previous sections, however, the density at the magnetic axis is not well determined by the measurements of the DCN interferometer. Therefore, it is preferable to use the integral from $\rho_{pol} = 0$ to $\rho_{pol} = 0.4$ for peaking calculation instead of the core density $n_e(0)$. Also other definitions, like $n_e(0.4)/n_e(0.8)$, can be found in the literature, which usually are equal to one for a flat profile. The peaking parameters p_1 and p_2 defined here, in contrast, are equal to zero for a flat profile, see figure 6.13.

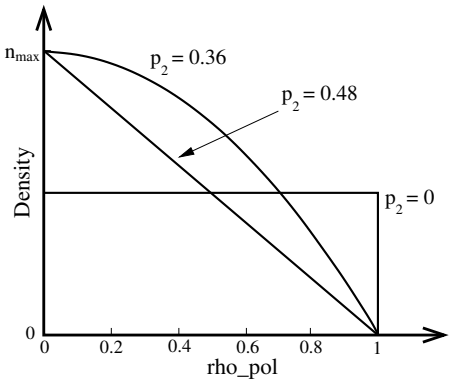

Figure 6.13: *Resulting peaking parameter p_2 for a flat profile, a linear profile and a parabolic profile.*

6.8 Implementation as an ASDEX Upgrade real-time diagnostic

The cycle time of the ASDEX Upgrade discharge control system is of the order of 1 millisecond. This means that each 1 ms, data from diagnostics, status information from heating and power supply systems, data from coil and divertor temperature monitoring systems etc. is collected. The data is compared to the pre-programmed setpoint values (like plasma current, position and size, density,...), and commands are sent to the plasma actuators such as coils, gas inlet valves or heating systems. When talking about 'real-time' diagnostics, then the idea is that the acquisition of data from the hardware, data analysis by a real-time algorithm and data transfer to the feedback control system should not last longer than one cycle time, so that the control system is always supplied with an up-to-date result. Thus, when density profiles and peaking parameters are to be used for feedback control, their calculation and transfer to the control system has to be completed within less than a millisecond. To fulfill this criterion, it is necessary to use a computer whose processor is fast enough to complete the required calculation within one cycle time. However, this is only a necessary condition for real-time operation, but not a sufficient one. The principal difficulty in this context is that in modern operating systems, many processes are running in parallel, and the main design criterion is to provide fast response to the commands of a human user who is sitting in front of the monitor. If, for example, the user moves the mouse, he expects that the cursor on the screen immediately follows this movement. If there was a delay of a second, this would not be acceptable. However, if the delay is just a millisecond, it is too short for human perception and the user will have the impression of a smooth movement of the mouse cursor. Therefore, standard operating systems have been designed to run smooth on the time scale of human perception. For them, it is not critical when some system-internal background process occupies the processor for a few milliseconds and interrupts a user program.
For some applications, like feedback control on a fusion experiment, however, this is not an acceptable status. Here, an operating system is required which provides deterministic behavior, i.e. for which it can be guaranteed that a given algorithm will, under all circumstances, finish within a certain time interval. Such operating systems with deterministic response time are referred to as 'real-time operating systems'. The ASDEX Upgrade dis-

charge control system, for example, is based on the commercial real-time operating system VxWorks by Wind River [36]. The magnetic diagnostic, from which the 69×39 flux matrix can be obtained, is based on LabView real-time by National Instruments [37]. For the 2009 ASDEX Upgrade campaign, the algorithm for density profile calculation was implemented on a SPARC workstation with the UNIX-based operating system SOLARIS by Sun Microsystems [38]. The crate with the backplane bus system that hosts the digital DCN phase counters (see figure 5.18 in section 5.4) was connected to this computer to provide access to the interferometer data. By accordingly adjusting the SOLARIS scheduler and giving the data acquisition and processing program highest priority, a completion of the task within less than a millisecond was reliably achieved.

Another issue is low-latency data transfer between the real-time diagnostics and to the control system. A standard Ethernet connection via the Transmission Control Protocol / Internet Protocol (TCP/IP) does not meet the timing requirements. This protocol guarantees that all sent data packets do arrive at the receiver and arrive in the proper order. Ensuring this requires some additional overhead including re-sending of data in case of packet loss. This slows down the data transfer, a typical transfer time is in most cases about 1-2 ms, but from time to time, interruptions of the order of 10 ms and more are observed, e.g. due to packet loss. Therefore, some faster transfer strategy is required. On ASDEX Upgrade, two methods of real-time communication are currently in use. One of them is Ethernet transfer using the User Datagram Protocol (UDP). This protocol does hardly include any error handling services, it does not guarantee the arrival of a packet, and the packets may arrive in different order than they were sent. However, as this saves much overhead, transfer is faster than with TCP/IP. It has been found that the transfer of some ten floating point numbers takes some hundred microseconds. Therefore, this solution was chosen for the transfer of the profile coefficients and the peaking parameters to the control system. However, this transfer time does no longer hold for larger data arrays, like the 69×39 matrix that is provided by the magnetic diagnostic. As a second transfer strategy, which is able to handle large data arrays, a reflective memory technology has been chosen on ASDEX Upgrade. Each computer in the corresponding real-time network is equipped with a PCI plug-in card that has 256 MB of memory on board. Those cards are connected to each other via optical fibers, through which the content of the memory is synchronized between the cards. When one participant in the network writes data into the memory, the same data appears in the memory of the other PCI cards within microseconds.
However, in the year 2009, when the main experimental studies for this thesis were carried out, the installation of the real-time data network was still an ongoing process. Initially, only the UDP path that connects the interferometer computer with the control system was operational, but the magnetic diagnostic was not yet connected. For this reason, a static magnetic equilibrium was used for profile calculation. Before a discharge with feedback control on the density profile could be performed, the 69×39 ρ_{pol} matrix from an earlier discharge with identical plasma parameters had to be read from the database and inserted into the program code on the interferometer computer. By the end of the 2009 campaign, the magnetic diagnostic was connected to the control system via a reflective memory card. However, the only link between the control system and the interferometer computer was still a UDP connection, not being capable of transferring the large matrix within the required time. Nevertheless, a way has been found to calculate density profiles from the real-time magnetic data. An important property of the algorithm for profile calculation is that the calculation of the $\beta_{Hc,k}$'s according to equation (6.7) does only require data from magnetic

measurements, but no input from the interferometer. For this reason, it was decided to split the algorithm in two parts and distribute them to two computers: The first part was implemented on the computer of the magnetic diagnostic. It takes the large 69×39 flux matrix and calculates the $\beta_{Hc,k}$'s. In case of 4 basis functions, which is the maximum number that was foreseen during the development phase of the algorithm, these form just a 5×4 matrix. The corresponding 20 floating point numbers are successfully transferred to the interferometer computer via UDP within the given time limit. There, the second part of the algorithm calculates the profile coefficients and finally the peaking parameters from the $\beta_{Hc,k}$'s and the measured line-integrated densities. The results are then sent to the control system via UDP.
At the end of the 2009 campaign, the magnetic diagnostic delivered a new equilibrium each 6 milliseconds. The density, in contrast, is measured with a frequency of about 10 kHz. To provide a density profile each control cycle, the measured densities were collected and averaged over 1 millisecond and then used for profile calculation, together with the latest received magnetic data. That way, each magnetic equilibrium is used 6 times on average.

7 Experiments on the impact of central ECRH on the density profile

The experimental aim of this work is to perform real-time feedback control of the shape of the density profile on ASDEX Upgrade. Routinely, the discharge control system only allows for density feedback control of the line-integrated density measured by one channel of the DCN interferometer. This line-integrated measurement is compared to a pre-programmed setpoint and the gas inlet valves are controlled accordingly. That way, basically the average number of particles in the plasma is controlled, but not their spatial distribution.
The active control of the density profile is more challenging as it does not only require the real-time calculation of the profile, but also the identification of at least one actuator that allows for a modification of the shape of the profile. In principle, one could think of using the gas inlet valve as actuator. However, when the total density shall be kept constant, one has hardly any freedom to modify the gas inlet rate. Just short gas pulses are possible in that case, which only cause transient effects. A better option would be the use of a second fueling system like the pellet injector which provides a non-peripheral particle source. However, the injection of pellets is accompanied by an increased risk of fringe jumps, which would force one to stop the calculation of the density profile. Therefore, it was decided to use central heating as actuator for profile control. As the electron cyclotron resonance heating provides a very localized power deposition in the plasma, it is a very useful tool for applying local heat sources, which in turn influence the density profile under certain conditions, see chapter 2.
Before active feedback on the density profile could be performed, a series of test discharges was required to identify plasma parameters for which ECRH has an effect on the density profile. This effect had to be quantified to define the operational window for the feedback experiments. In those test discharges, the ECRH was turned on and off in a periodic sequence to test the reproducibility of the effect and study the involved time constants.
In the first section of this chapter, the test discharges performed in low confinement mode will be presented. The second section describes those in H-mode, and the third one the experiments with feedback control, which are the first demonstration of active shaping of the density profile with ECRH on ASDEX Upgrade.
A summarizing overview of the experiments and an analysis of the underlying processes of heat particle transport will be presented in the next chapter.

7.1 Feed-forward experiments in L-mode

As shown in chapter 2, central ECRH causes a flattening of the density profile in low-density L-mode discharges when the most unstable mode is a TEM. This effect can be

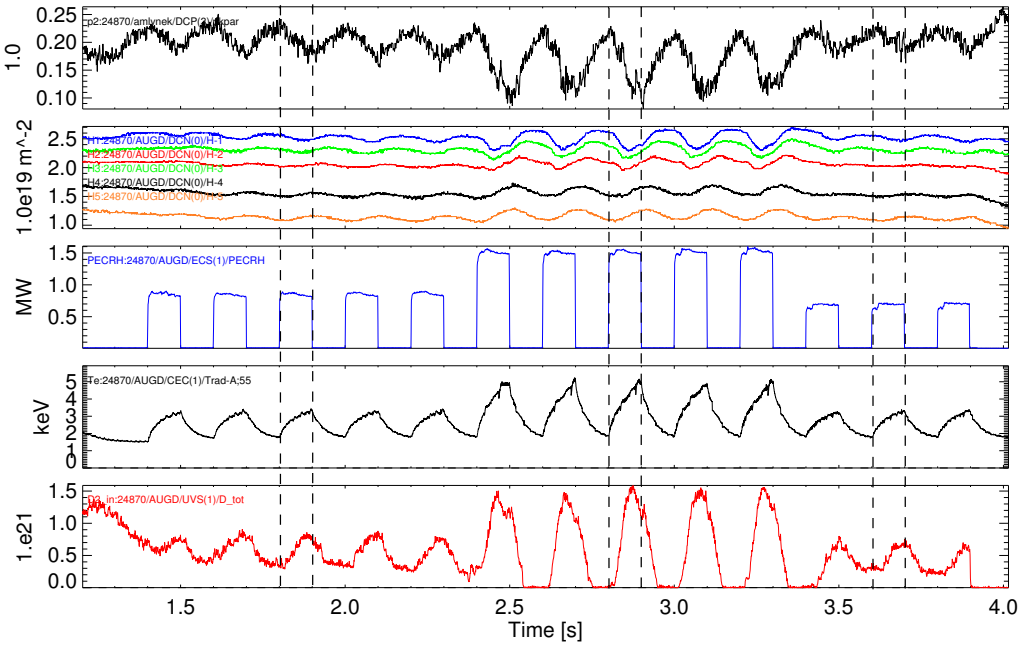

Figure 7.1: *Discharge #24870 ($n_{e,\,lin\,H-1} = 2.5{\cdot}10^{19}\,m^{-2}$): Time traces of the peaking parameter p_2, the 5 line-integrated densities measured by the DCN interferometer, the applied ECRH power, the electron temperature measured by ECE channel 55 and the throughput of the gas inlet valves (from top to bottom).*

exploited for active control of the density profile shape. In a first test discharge (#24870), the global plasma parameters of earlier experiments performed on ASDEX Upgrade (plasma current $I_P = 600\,\mathrm{kA}$ and line-integrated electron density on H-1 $n_{e,lin} = 2.5{\cdot}10^{19}\,m^{-2}$) have been used. The toroidal field in the plasma center was set to $B_T = -2.5\,\mathrm{T}$, which allows for second-harmonic ECRH power deposition in the center for the gyrotron frequency of 140 GHz. The ECRH launcher was adjusted in such way that the heating beam goes through the plasma center according to ray-tracing calculations performed for an earlier reference discharge with identical parameters. After reaching the flat-top phase, the ECRH system was turned on and off in a pre-programmed pattern. After 5 pulses with a power of about 0.9 MW, a duration of 100 milliseconds each and a spacing of 100 ms, there were further five pulses at 1.5 MW and three at 0.7 MW. Figure 7.1 shows the time traces of the peaking parameter p_2 as defined in equation (6.13) in section 6.7, the 5 interferometer channels, the applied ECRH power, the temperature measured by ECE channel 55 and the throughput of the gas inlet valves. In this discharge, the gas valves were controlled by the routinely used density feedback algorithm which tries to keep the H-1 density fixed at $2.5 \cdot 10^{19}\,m^{-2}$. Therefore, one has to be aware that an observed change of the density profile is not necessarily a pure effect of density pump-out by ECRH. When central heating power is applied and causes a reduction of the density measured by interferometer channel H-1, the density feedback system will open the gas valves, which causes secondary effects on the profile as the gas inlet comes from the plasma edge. Apparently, the H-1 density

and the peaking parameter start decreasing and the H-5 density starts increasing as soon as the ECRH is turned on. For the H-5 density, this behavior is observed until the end of the heating pulse. For the H-1 density, this is different. When about 2/3 of the ECRH pulse have elapsed, it becomes constant or even slightly rises again, at least in the case of high ECRH power. At low heating power, the peaking parameter falls and rises in phase with the ECRH pulses. At high ECRH power, this is similar, however, one observes a trend of saturation after about 2/3 of the heating pulse. The amplitude by which the peaking parameter p_2 varies is roughly proportional to the applied ECRH power. The gas valves open and close according to the modulation of H-1. This experiment confirms that switching on ECRH is a useful actuator for flattening the density profile at the given plasma parameters.

To study the effect of pure ECRH and pure gas puffing on the density profile, a further discharge (#25092) was performed, where an H-1 density of $2.5 \cdot 10^{19}\ m^{-2}$ was set by using a feedback loop until $t = 1.3\,s$. Then, the gas inlet rate was set to a fixed level of $0.8 \cdot 10^{21}$ particles per second, which was expected to provide an approximately constant density according to the experience made in earlier discharges. It turned out that this level was slightly too low, as one ended up at an H-1 density of about $2.1 \cdot 10^{19}\ m^{-2}$ at $t = 3.0\,s$. There were 4 ECRH pulses of 100 ms duration with 0.9 MW and further 4 pulses with 1.5 MW until $t = 3.0\,s$ (see figure 7.2). That way, the effect of ECRH could be studied without the secondary effect due to the density feedback on H-1. The result is similar to that obtained

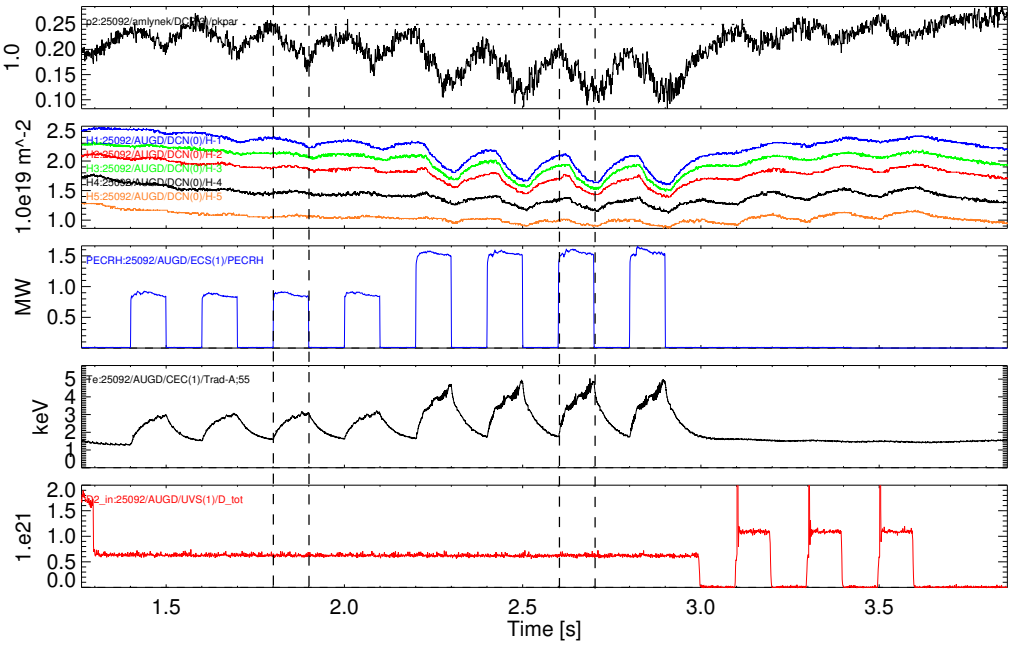

Figure 7.2: *Discharge #25092 ($n_{e,\,lin\ H-1} = 2.5 \cdot 10^{19}\ m^{-2}$): Time traces of the peaking parameter p_2, the 5 line-integrated densities measured by the DCN interferometer, the applied ECRH power, the electron temperature measured by ECE channel 55 and the throughput of the gas inlet valves (from top to bottom).*

with n_e feedback, just two differences are apparent:

- The H-1 density now keeps falling until the end of the ECRH pulse. The previously described trend of saturating or even rising after two thirds of the ECRH pulse is no longer observed. This was evidently a result of the gas puff from the edge and the resulting over-all increase of density.
- Going to 1.5 MW heating power mainly causes a downward shift of the peaking parameter, but the amplitude by which it is modulated by the heating pulses does not grow very much compared to the 0.9 MW case. This was different in the previously discussed discharge, where a growth by a factor of about two was observed, which is approximately the factor by which the heating power is increased.

In addition, the effect of gas pulses at constant heating power was studied after t = 3 s. The ECRH system was switched off to have pure ohmic heating and the gas level was first set to zero. Then, 3 gas pulses of 100 ms duration followed. They cause an increasing density on all 5 lines of sight of the interferometer, which is more pronounced on the edge channels. As a result of this, the peaking parameter decreases, but its variation is much smaller than that caused by ECRH pulses.
These results show that operating in density feedback mode enhances the effect of flattening with ECRH. A reduction of the core density results in an opening of the gas valves which in turn increases the edge density and thus helps to reduce the peaking of the density profile. The observations made so far cannot exclude that the density response may still be ongoing when the ECRH is switched on or off after 100 ms. Therefore, further discharges with an ECRH pulse duration of 500 ms were performed to explore the level at which density flattening saturates. Figure 7.3 shows the corresponding time traces for discharge #25231, which contains both, ECRH pulses during density feedback on H-1 and at fixed gas level. The peaking parameter reaches approximately the same saturation level in both cases, with n_e feedback on H-1 and at constant gas level. When n_e feedback control is applied, however, saturation is achieved more quickly. In case of 1.5 MW heating power, the peaking parameter saturates within 100 ms, in case of 0.7 MW, it needs of the order of 120-130 ms. When using a fixed gas level, this lasts about 150 ms (1.5 MW heating power) and 200 ms (0.8 MW). Also the relaxation time of the peaking parameter after switching off ECRH increases when a constant gas level is used. From this, one can conclude that using density feedback on H-1 accelerates the flattening process, but does not significantly influence the achievable saturation level. This supports the initially stated assumption that, if the total particle content of the plasma is not allowed to change much, the gas valves can only induce transient effects on the density profile, but no persistent changes.
In discharge #25092, which was performed at constant gas level, the modulation of the peaking parameter at 1.5 MW was much less than in discharge #24870, where density feedback on H-1 was applied. From the observations made in #25231, one can conclude that at constant gas level, a pulse duration of 100 ms is not quite sufficient to reach the lower saturation level, and the pulse spacing of 100 ms is not enough to allow for a full recovery of the peaking parameter to its original value. In #25231, full relaxation lasts approximately 150-200 ms when operating at a fixed gas level. This explains why the the peaking parameter showed less modulation in #25092 than in the reference case #24870.

As the next step, the dependency of the flattening effect on the absolute density will be discussed. For this purpose, discharge #24870 was repeated at line-integrated densities

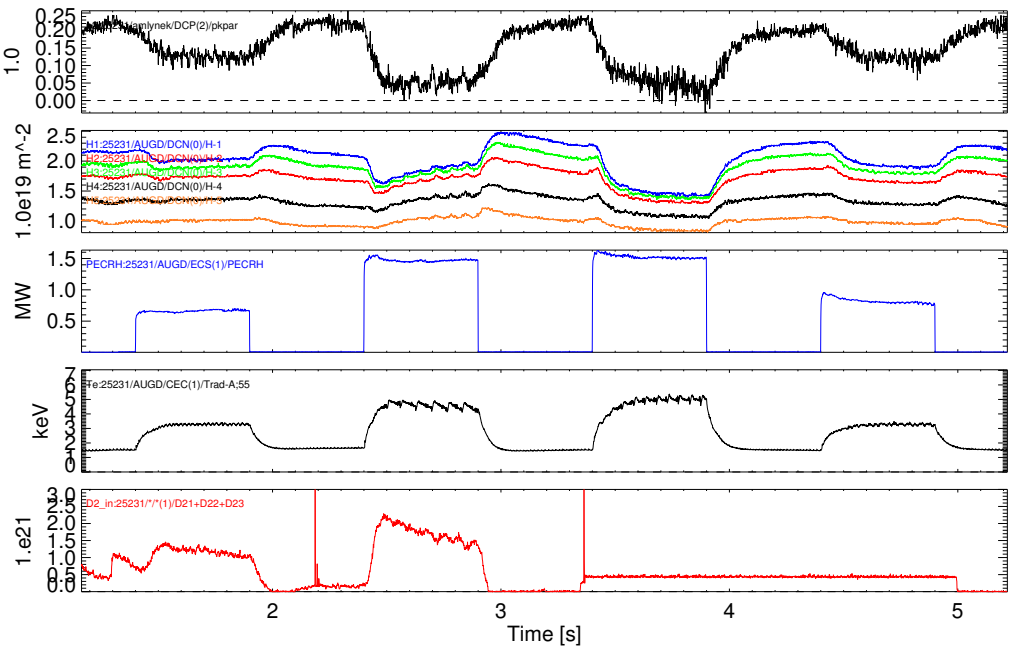

Figure 7.3: *Discharge #25231: Time traces of the peaking parameter p_2, the 5 line-integrated densities measured by the DCN interferometer, the applied ECRH power, the electron temperature measured by ECE channel 55 and the throughput of the gas inlet valves (from top to bottom). During the first two ECRH pulses, the density feedback loop on interferometer channel H-1 was active. The following two pulses were performed at constant gas level.*

of 2.0, 3.0 and $4.0 \cdot 10^{19}\, m^{-2}$. In case of 2.0 (#25042, time traces are not shown), one gyrotron pair dropped out during the discharge, so there were no pulses with full 1.5 MW heating power. Flattening at 0.7-0.8 MW, however, works well, similarly to #24870. At $3.0 \cdot 10^{19}\, m^{-2}$ (#25041), there is only a weak effect on the peaking parameter at a heating power of 0.7-0.8 MW (compare figure 7.4). Only at full 1.5 MW, a clear and strong flattening effect is observed. The peaking parameter increases and drops in phase with the ECRH pulses, as observed in the previous discharges. However, the temporal behavior of the central density (H-1) differs from that in #24870. Here, it reaches its minimum in the middle of the ECRH pulse already and then starts rising again. On the one hand, this may indicate that the over-all increase of density that is initiated by the feedback loop on the line-integrated H-1 density outweighs the pump-out effect at this point, forcing the core density to rise again. However, this assumption cannot be verified as no reference discharge at constant gas level was performed at this density. On the other hand, it may be due to the fact that this discharge shows a transition to H-mode, which will become apparent in the further discussion.
When going to a density of $4.0 \cdot 10^{19}\, m^{-2}$ (discharge #25038), the picture is completely different, see figure 7.5. Heating pulses at low power (0.8 MW) have the opposite effect now: They cause the core density to increase and the edge density to decrease, leading to

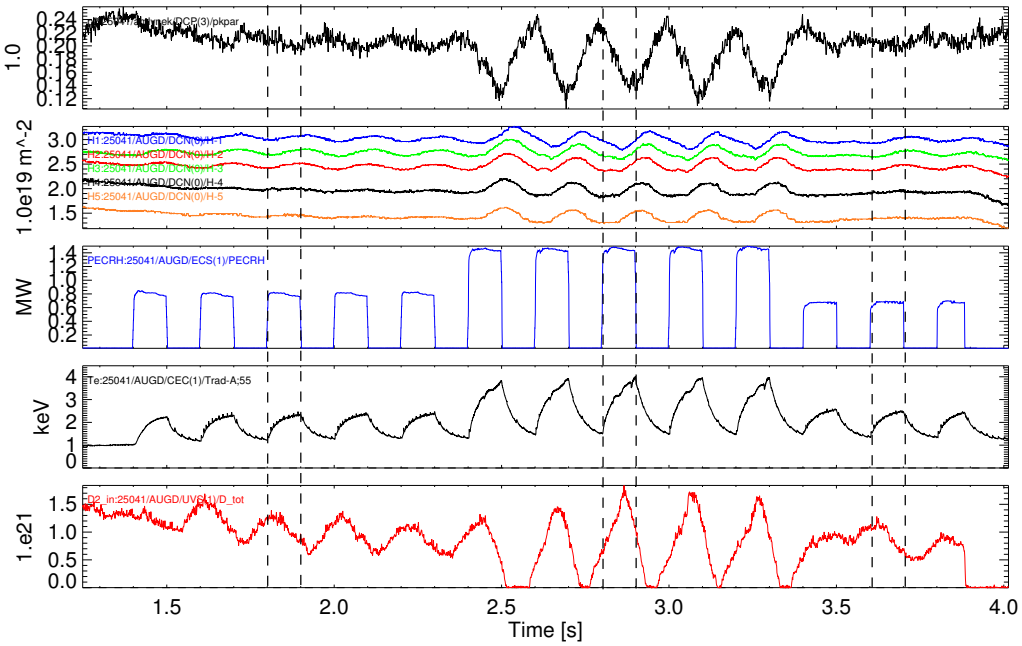

Figure 7.4: *Discharge #25041 ($n_{e,\,lin\,H-1} = 3.0{\cdot}10^{19}\,m^{-2}$): Time traces of the peaking parameter p_2, the 5 line-integrated densities measured by the DCN interferometer, the applied ECRH power, the electron temperature measured by ECE channel 55 and the throughput of the gas inlet valves (from top to bottom).*

significant density peaking. So the previously described effect of pump-out reverses sign. When going to 1.4 MW heating power, the picture changes again. After a settling time of two pulses, the heating pulses induce a coherent oscillation of the plasma density on all 5 interferometer channels. The peaking parameter decreases when ECRH is on and increases when ECRH is off.

To sum up, the application of central ECRH allows for a flattening of the density profile of L-mode discharges up to a density of about $2.5 \cdot 10^{19}\,m^{-2}$. At $3.0 \cdot 10^{19}\,m^{-2}$, flattening is still possible, but requires the use of full 1.5 MW of ECRH power. At a density of $4.0 \cdot 10^{19}\,m^{-2}$, central heating with 0.8 MW makes the profile more peaked. The flattening of the profile and the relaxation lasts approximately 100 ms when density feedback on H-1 is applied. When operating at constant gas level, it lasts about 150-200 ms.

7.2 Feed-forward experiments in H-mode

The influence of central ECRH on the density profile of H-mode discharges was also investigated. According to figure 2.8 in chapter 2, a flattening effect should be observable at low densities of the order of $4.0 \cdot 10^{19}\,m^{-2}$. However, one has to be aware that the discharges on which this figure is based have been carried out before ASDEX Upgrade was equipped with

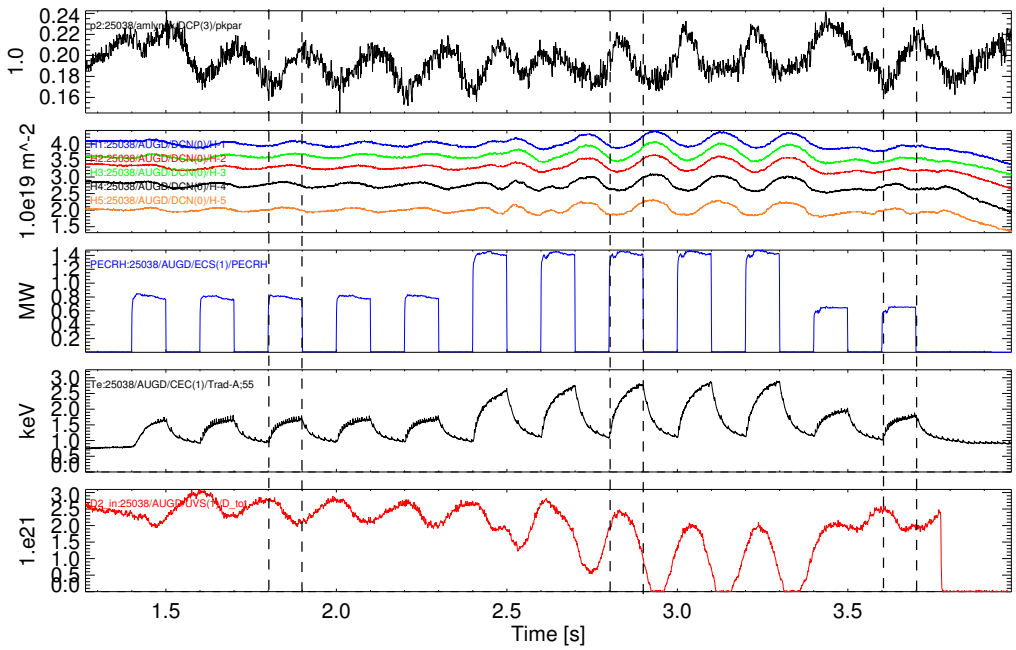

Figure 7.5: *Discharge #25038 ($n_{e,\,lin\ H-1} = 4.0 \cdot 10^{19}\,m^{-2}$): Time traces like in figure 7.4.*

a first wall that consists entirely of tungsten. Due to the new wall material, the operational window of ASDEX Upgrade has changed and it is no longer possible to perform low-density H-mode discharges at the same low collisionality. Anyway, this density range in H-mode is only accessible on ASDEX Upgrade shortly after a boronization of the vessel walls, as otherwise, recycling of particles from the wall increases the plasma density above this value even when all gas inlet valves are closed, at least when neutral beam heating is applied, which fuels as well.

In a first discharge (#25450), ECRH pulses were injected into a 600 kA H-mode plasma with a density of $4.0 \cdot 10^{19}\,m^{-2}$, heated by 5 MW of neutral beam injection. However, no effect of the ECRH on the density was observed. As the discharge was suffering form a neoclassical tearing mode, which resulted in poor confinement, it was repeated at reduced NBI power (4 MW, discharge #25455) to avoid the mode. However, also under these conditions with strongly reduced mode activity, no significant effect of ECRH was observed.

In discharge #25456, slightly modified parameters were used: The density was set to $5.0{\cdot}10^{19}\,m^{-2}$, only 2.5 MW of NBI were injected and the ECRH launcher angle was modified a little, but should still cause central power deposition according to ray-tracing calculations. These parameters were copied from an earlier discharge that was found in the database. There was no feedback control on the total density, the gas level was set to a fixed value which would provide the desired density according to prior experience. As figure 7.6 illustrates, a strong effect of central ECRH on the density profile is observed: Whereas the edge channels H-4 and H-5 are not affected, a clear and reproducible increase of density is observed on the core channel H-1. This increase is roughly proportional to the ECRH power.

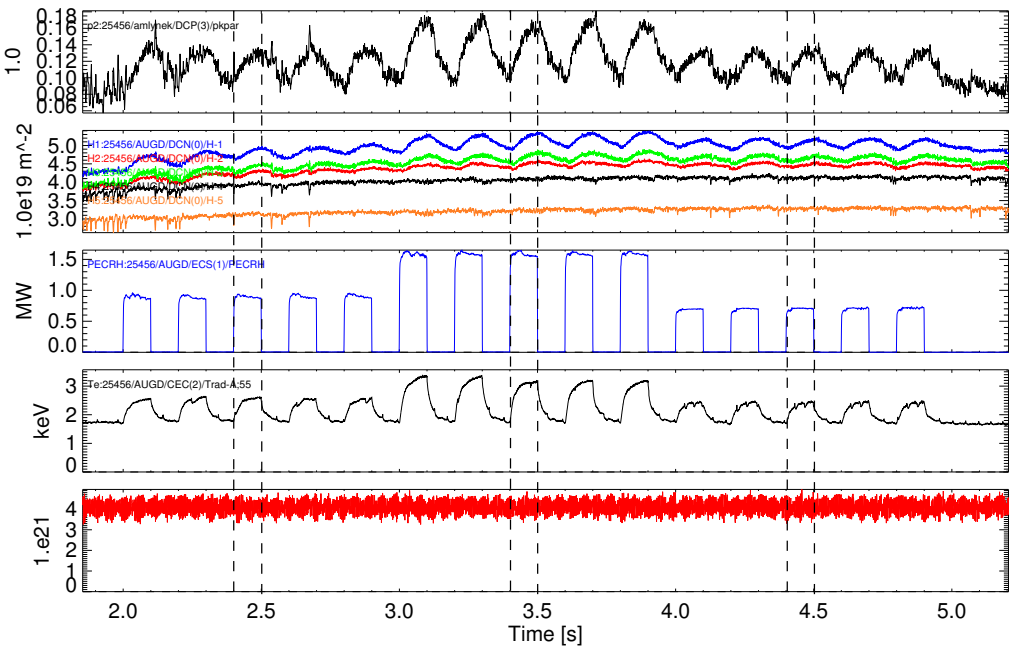

Figure 7.6: *Discharge #25456: Time traces of the peaking parameter p_2, the 5 line-integrated densities measured by the DCN interferometer, the applied ECRH power, the electron temperature measured by ECE channel 55 and the throughput of the gas inlet valves (from top to bottom).*

The normalized peaking parameter p_2, which is shown in the figure, increases when ECRH is on and decreases when ECRH is off. That way, a set of plasma parameters has been identified which allows for profile control with ECRH in H-mode. All feedback experiments in H-mode were performed with those settings.
That way, it is possible to increase the peaking of the density profile by applying central ECRH. A flattening of the profile like in the low-density L-mode case, however, can not be achieved.

7.3 Experiments with feedback control of the density profile

There are several requirements for successful feedback control of the density profile. Firstly, the density profile must be available in real-time, which requires the magnetic equilibrium and the measurements by the DCN interferometer. Secondly, a scalar parameter has to be derived from the profile which measures its peakedness, and this parameter has to be communicated to the control system. Finally, a control algorithm is required which continuously monitors the peaking parameter and sends commands to the actuator, namely the ECRH system.
The experiments for feedback control of the density profile were performed in 3 different stages of technical implementation. Initially, the profiles were calculated from a static

magnetic equilibrium, as the real-time data transfer from the magnetic diagnostic was not yet implemented, and the feedback loop operated with so-called 'inserted segments' in the discharge control program. This control technique had been used for other applications in the past and could be adapted for profile control with low time effort. As a consequence of the static equilibrium, any changes of plasma position and magnetic configuration had to be avoided, as otherwise, the calculated density profile would have been affected by a systematic error. The technique of inserted control segments continuously monitors an input parameter of the control system, in this case the peaking parameter, and compares it to a pre-defined threshold. If it is above the threshold, the control system jumps into an additional program segment in which the ECRH is turned on. This segment is left when either the peaking parameter falls below a second (lower) threshold, or when a certain amount of time has elapsed. All other control parameters besides the ECRH power are kept at their previous value during the segment. As a consequence of inserting this segment, all subsequent events scheduled in the discharge program are delayed by the duration of the segment. This is a clear disadvantage of the method, as it prevents changes of plasma parameters, such as the total density, during the phase with profile control. A programmed change would occur at a later point in time which can not be precisely predicted. So only feedback control at constant total density was performed with this method, which allowed for the use of the non-normalized peaking parameter p_1 defined in section 6.7.
In a second phase, a more advanced feedback controller was used, which does no longer delay subsequent program elements. This controller allows to define a time-dependent setpoint to the peaking parameter in the discharge program. The controller has a built-in hysteresis, so there are two thresholds which are situated symmetrically above and below the setpoint. If the peaking parameter rises above the upper threshold, ECRH is turned on, and if it falls below the lower threshold, ECRH is turned off. This scheme can be reversed when ECRH increases the peaking of the profile, like in the H-mode case. With this controller, density ramps could be performed during the feedback control phase, so it was necessary to use the normalized peaking parameter p_2, which does not scale with the absolute density. The density profile, however, was still calculated on the basis of a static equilibrium. Shortly before then end of the 2009 campaign, profile calculation on the basis of real-time magnetic equilibria was implemented. This allowed for changes of the magnetic configuration and the plasma position during the discharge, which is the last required improvement for universal feedback control.

First, real-time control of the density profile was demonstrated in L-mode in discharge #24985 with the control scheme based on inserted segments (see figure 7.7). In this discharge, the non-normalized peaking parameter p_1 was calculated in real-time. For comparison, also the normalized peaking parameter p_2 is shown in the figure, which has been calculated afterwards with a time resolution of $100\,\mu$s. As the real-time algorithm averages the measured line-integrated densities over a millisecond before calculating the profile (see end of section 6.8), the peaking parameter calculated in real-time shows less noise. The peaking controller was switched on at $t = 1.7\,$s, the upper threshold for turning on ECRH was set to $p_1 = 5 \cdot 10^{18}$ and the lower threshold for turning off to $p_1 = 4 \cdot 10^{18}$. Density feedback control on H-1 was applied, the setpoint was $3 \cdot 10^{19}\,m^{-2}$. So one has to be aware that there are two feedback controllers active at the same time, one of them controlling the line-integrated H-1 density, using the gas inlet valves as actuator, and one the shape of the density profile, using central ECRH as actuator. These two controllers are not independent of each other, but due to the observations made in the preparatory feed-forward

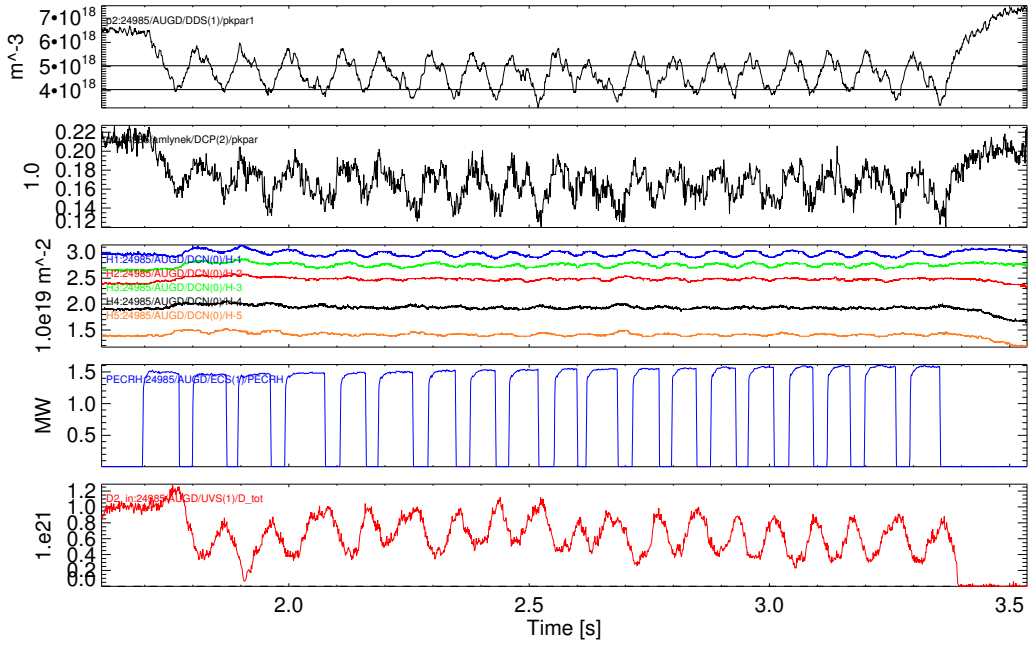

Figure 7.7: *Discharge #24985: Time traces of the peaking parameter p_1 (calculated in real-time), including the controller thresholds, the peaking parameter p_2, the 5 line-integrated densities measured by the DCN interferometer, the applied ECRH power and the throughput of the gas inlet valves (from top to bottom). There is no ECE measurement available for this discharge.*

experiments, it can be expected that feedback on the line-integrated density enhances the effect of central ECRH on the density profile. The timeout limit for the inserted segments was set to 100 ms and the maximum number of segments to 19, just to ensure that the load limit of the gyrotrons (2 seconds) cannot be exceeded.
As the time traces show, the peaking parameter is above the upper threshold at $t = 1.7\,s$, and accordingly, ECRH is switched on. The profile flattens, and as the lower threshold is reached, ECRH is switched off. This results in an immediate increase of the peaking parameter. In contrast, when the upper threshold is reached and ECRH is switched on, the peaking parameter continues rising for about 10 ms until it starts decreasing. For this reason, there is overshooting in the positive direction.

For all further feedback experiments, the more advanced control scheme without inserted segments has been used, in connection with the normalized peaking parameter p_2. In discharge #25303, the new possibilities provided by the improved control scheme were exploited by performing a density scan during the control phase. The peaking controller was active for 1.9 seconds, the peaking setpoint was statically set to 0.14 with a hysteresis of ± 0.005. Initially, the (line-integrated) plasma density for H-1 was set to $2.0 \cdot 10^{19}\,m^{-2}$ and kept at this value for 0.4 s. Then, steps were programmed up to 2.5, 3.0 and 4.0 with a temporal distance of 0.5 s. Figure 7.8 shows the time traces for this discharge. At the first

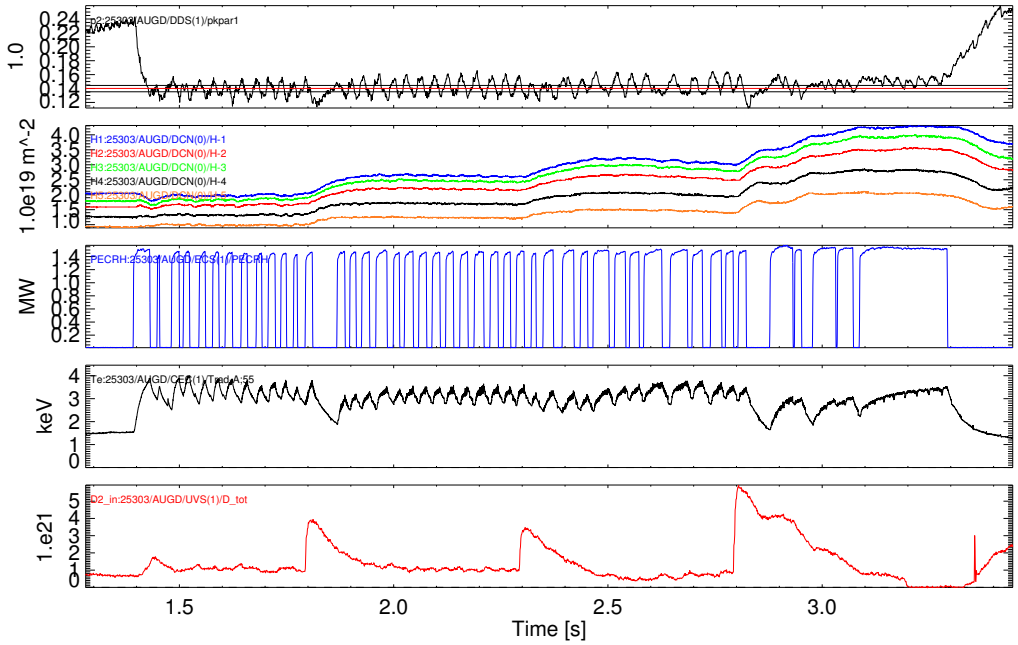

Figure 7.8: *Discharge #25303: Time traces of the peaking parameter p_2, including the controller setpoint (red line) and thresholds (black lines), the 5 line-integrated densities measured by the DCN interferometer, the applied ECRH power, the electron temperature measured by ECE channel 55 and the throughput of the gas inlet valves (from top to bottom).*

three density levels (2.0, 2.5 and 3.0), profile control works and one observes an increasing duty cycle of the ECRH modulation when going to higher densities. The duration of the heating pulses increases, whereas the time interval between two of them does not change much. This indicates that the peaking parameter always increases rapidly when ECRH is off, but in presence of ECRH, it decreases the more slowly the higher the total density is. At a density of $4.0 \cdot 10^{19}\, m^{-2}$, however, a status is finally reached where ECRH is permanently on but peaking does not decrease any more. This confirms the observation made in the previous feed-forward experiments that the effect of ECRH on the density profile changes significantly between 3.0 and $4.0 \cdot 10^{19}\, m^{-2}$, and it shows the limitations of the method.
Also in this discharge, an overshooting of the peaking parameter in the positive direction is observed, and especially at a density of $2.0 \cdot 10^{19}\, m^{-2}$ in the negative direction as well. A closer look reveals that there is a time delay of 2-3 milliseconds between the crossing of the threshold and the switching of the ECRH. This is an inherent property of the controller. Furthermore, about half a millisecond elapses until the gyrotrons deliver their full output power. After this, there is an additional time-lag until the peaking parameter shows a response to the modified ECRH power. At densities of 2.5 and $3.0 \cdot 10^{19}\, m^{-2}$, there is a rather prompt response when ECRH is switched off. However, when ECRH is switched on, the peaking parameter continues rising for several milliseconds before it starts decreasing. This results in an overshooting in the positive direction. At a density of $2.0 \cdot 10^{19}\, m^{-2}$, in contrast, there is overshooting in both directions.

Another application of the feedback system has been tested in discharge #25304, in which a constant density of $3.0 \cdot 10^{19}\, m^{-2}$ was chosen, but a linear ramp from 0.09 to 0.20 was programmed as setpoint for the peaking controller, see figure 7.9. The feedback scheme

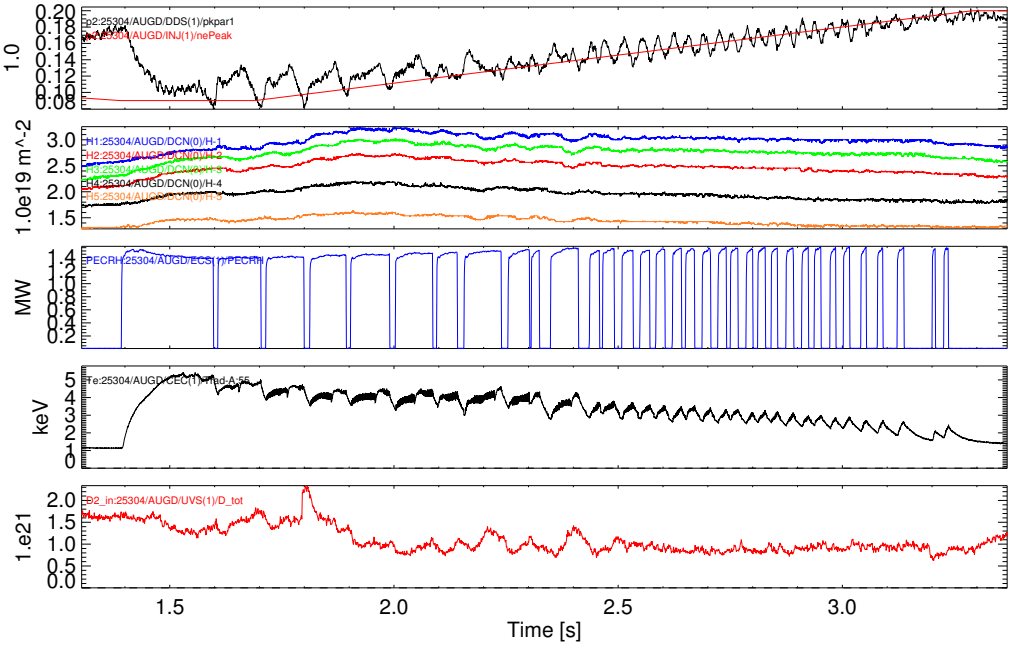

Figure 7.9: *Discharge #25304: Time traces of the peaking parameter p_2, including the controller setpoint (red line, hysteresis ± 0.005), the 5 line-integrated densities measured by the DCN interferometer, the applied ECRH power, the electron temperature measured by ECE channel 55 and the throughput of the gas inlet valves (from top to bottom).*

worked, the peaking parameter actually oscillates around the setpoint, following the ramp. It is remarkable that in the early phase, when the peaking setpoint is around 0.10, the duty cycle of ECRH modulation is close to 1: When ECRH is switched off, the peaking parameter immediately starts rising and crosses the upper threshold within approximately 10 milliseconds. Accordingly, ECRH is switched on again, but the peaking parameter nevertheless continues rising at reduced slope for further 50-60 ms. Only then, it starts decreasing. Later in the discharge, when the peaking setpoint is higher, this is different. There, ECRH causes a prompt drop of the peaking parameter.

Feedback control of the density profile could also be demonstrated for the H-mode case. The global plasma parameters were copied from the feed-forward discharge #25456. As central ECRH has been found to cause a peaking of the density profile under these conditions, the feedback scheme had to be reversed: The ECRH system is switched on when the peaking parameter is below the setpoint, and off when it is above. Again, there are two thresholds which are situated symmetrically around the setpoint. As setpoint for the peaking parameter, a linear ramp going from 0.06 to 0.18 within 1 second was programmed in discharge

#25481. Then, at t = 3.0 s, the setpoint was set to 0.13 and successively, some plasma parameters were modified. First, NBI power was increased from 2.5 to 5 MW at t = 3.3 s. Then, 0.25 s later, the gas setting was changed from a fixed level to density feedback on H-1 with a setpoint of $4.0 \cdot 10^{19}\, m^{-2}$. Finally, there were two pre-programmed ECRH pulses with a duration of 100 ms. As figure 7.10 illustrates, peaking control was successful. The

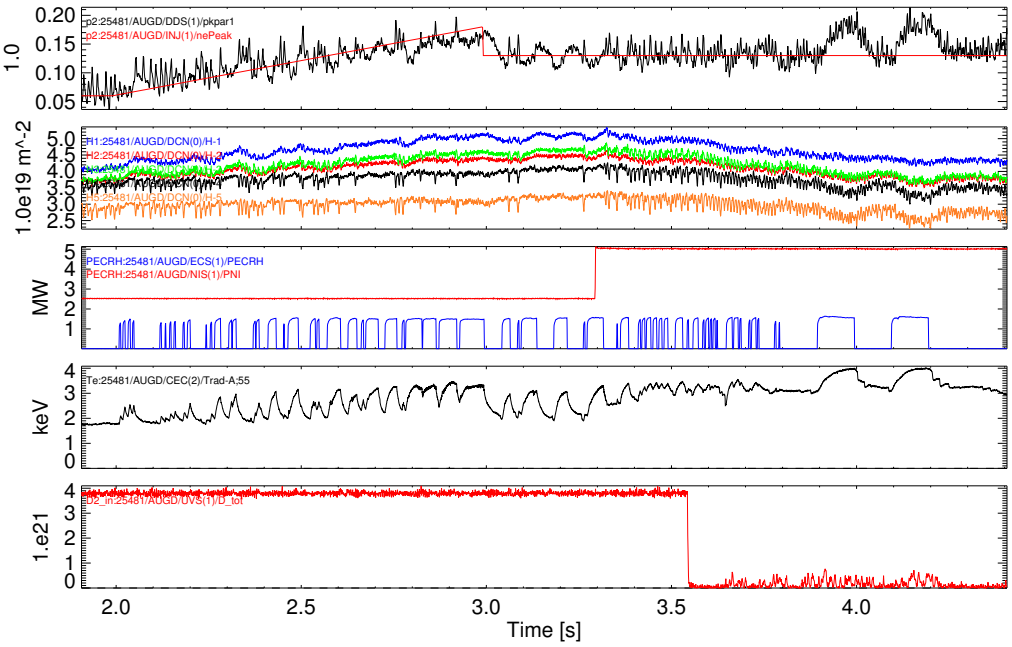

Figure 7.10: *Discharge #25481: Time traces like in figure 7.9. The third box in addition shows the neutral beam heating power as red curve.*

peaking parameter follows the linear ramp, and it performs the programmed step down at 3.0 s. All in all, the peaking parameter is more noisy than in L-mode due to the impact of ELMs on the density measurement. When the neutral beam heating power is increased, the peaking parameter shows noise at higher frequency, but still remains centered around the setpoint value. When density is reduced, the peaking parameter remains at the desired value. However, it still does so when the peaking controller is switched off at 3.8s, so from this data it is not possible to unambiguously assess whether the feedback control scheme still works at the reduced density. When the two pre-programmed ECRH pulses are injected into the plasma, the response of the density differs from that observed under the initially chosen conditions. At a density of about $4.5 \cdot 10^{19}\, m^{-2}$ (H-1) and 5 MW of NBI power, ECRH has no significant influence on the core density any more, however, it causes a reduction of the edge density.

Finally, when the real-time data transfer from the magnetic diagnostic had been implemented and density profiles were calculated from actual real-time magnetic data, one last discharge (#25677) was performed in which feedback control was applied in L-mode and H-mode. In the L-mode case, ECRH was turned on when the peaking parameter was

above the setpoint, and in H-mode, it was turned on when the parameter was below the setpoint. Figure 7.11 shows the time traces for this discharge. The controller was intended to be active in L-mode configuration from 1.5 to 2.5 s and in H-mode configuration from 3.3 to 4.3 s. Accordingly, three linear ramps were programmed as setpoint for the density peaking in those two time intervals. For technical reasons, the controller could only be enabled at t = 1.8 s. That way, feedback control in L-mode was restricted to the time window from 1.8 – 2.5 s. It can be seen that in both, L-mode and H-mode, feedback control was successful.

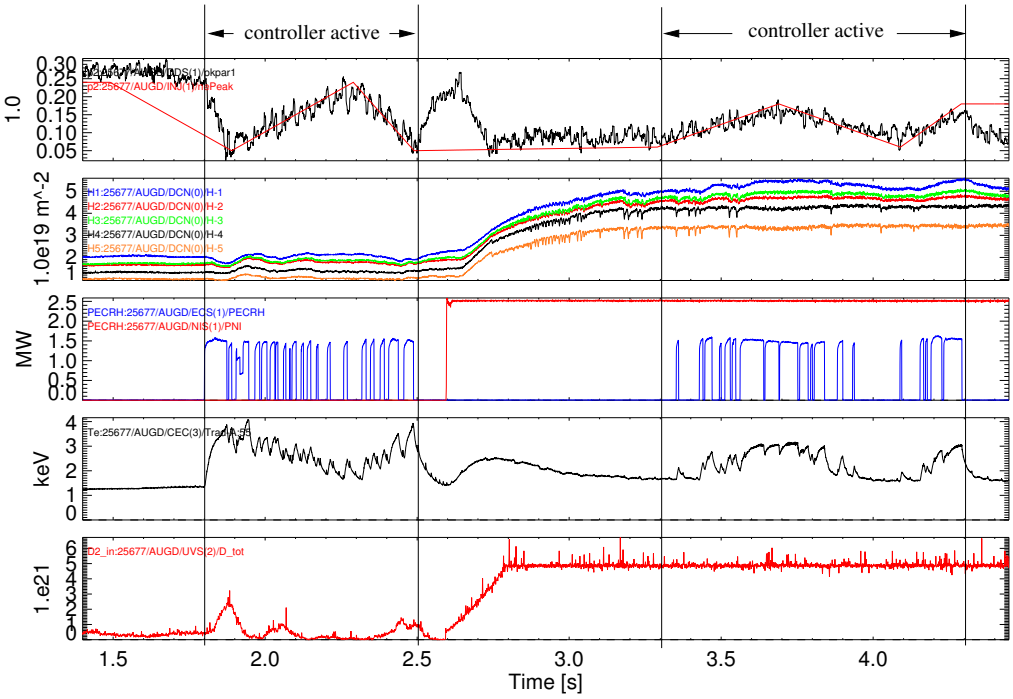

Figure 7.11: *Discharge #25677: Time traces like in figure 7.10.*

8 Analysis of the results

The experiments discussed in the previous chapter have shown that the application of central electron heating allows for a modification of the spatial distribution of density under certain conditions. In the first section of this chapter, the dependence of this effect on the plasma density will be discussed. In the following sections, the experimentally observed response of temperature and density profile to heating pulses will be analyzed with respect to the temporal behavior, and a simple simulation based on the transport equations will be performed to find out which assumptions on the transport coefficients are necessary to reproduce the experimental data.

8.1 Density dependence of the effect of ECRH

Figure 8.1 shows a diagram similar to figure 2.8 in chapter 2. It contains all those discharges listed in the previous chapter that were performed with a pre-programmed ECRH timing. The circles represent the cases with purely ohmic heating, the triangles the values after 100 ms heating with two gyrotrons and the squares the values after 100 ms at full ECRH power. In contrast to figure 2.8, the peaking parameter has not been normalized to 1 for the purely ohmic case. Evidently, at line-integrated H-1 densities up to $2.5 \cdot 10^{19}\, m^{-2}$, ECRH causes a strong flattening of the density profile. At a density around $3.0 \cdot 10^{19}\, m^{-2}$, the use of 2 gyrotrons is not very effective any more. Only at full heating power, a flattening comparable to that at lower density occurs. At a density of $4.0 \cdot 10^{19}\, m^{-2}$, the effect reverses sign and heating with 2 gyrotrons makes the profile more peaked. The case with 4 gyrotrons for this density is not included in the diagram, as the peaking parameter showed different response to the 5 ECRH pulses at this power, see section 7.1. In the NBI-heated H-mode discharge #25456, ECRH increases the peaking proportionally to the applied ECRH power. As the majority of discharges was performed in L-mode, the following more detailed analysis will focus on those.
As shown by figure 8.1, only a weak flattening is caused by 2 gyrotrons at a density of $3.0 \cdot 10^{19}\, m^{-2}$. This indicates that the flattening mechanism observed up to $2.5 \cdot 10^{19}\, m^{-2}$ has almost disappeared at this density. The strong flattening at full heating power is caused by a transition from an L-mode to a weakly developed H-mode regime, which usually has flatter profiles. Figure 8.2 shows the time traces of the edge interferometer channel H-5, the injected ECRH power, the gas inlet rate and a scrape-off layer current monitor signal, which is obtained by shunts that are connected to the divertor target modules [39], for discharge #25041 in a time window around two 1.5 MW heating pulses. A transition from L-mode to H-mode is accompanied by a sudden drop of the current monitor signal, whereas an H-L transition causes a sudden increase [39]. An L-H transition occurs when the power

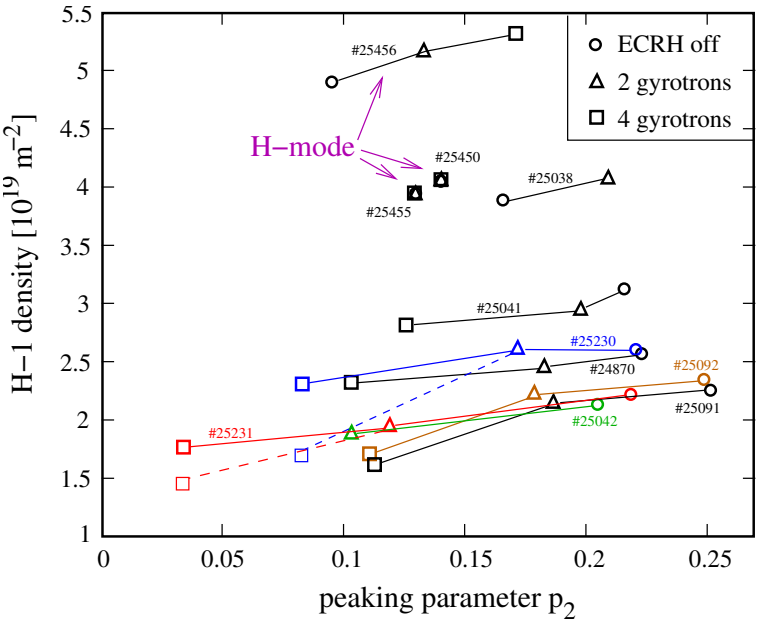

Figure 8.1: *Response of the normalized peaking parameter p_2 to ECRH pulses. The diagram shows the line-integrated density measured by interferometer channel H-1 and the peaking parameter for the cases without ECRH (circles), with 0.7-0.9 MW of ECRH (triangles) and with 1.5 MW of ECRH (squares). Symbols corresponding to the same discharge are connected by lines. In discharges #25230 and #25231, there were heating pulses in phases with and without density feedback on H-1. At full ECRH power, the H-1 density significantly differs for both cases. Therefore, both densities are shown in the diagram. The dashed lines represent the cases with constant gas level.*

flux through the plasma edge is above a certain threshold. This threshold depends on the density. For discharges which are similar to those discussed here, a minimum of the power threshold is reported to be at a line-averaged density[1] around $4.0 \cdot 10^{19}\, m^{-3}$ in [40]. When going to lower densities, the threshold strongly increases. One has to be aware that the power flux through the plasma edge does not instantaneously change when the central heating power is changed, as the heat content W of the plasma does in general not remain constant:

$$P_{edge} = P_{heating} - \frac{dW}{dt}$$

Accordingly, there is often a time delay between an increase of the heating power and the transition from L-mode to H-mode. This can be seen in figure 8.2: During the first half of each heating pulse, the edge density remains constant, although an increasing amount of gas is injected. Then, in the middle of the heating pulse, there is a sudden drop of the current monitor signal, indicating the transition to H-mode, and at the same time, the edge density starts rising and continues like this until the end of the ECRH pulse. The transition back to L-mode occurs roughly 50 ms after the end of the heating pulse, as the current monitor signal shows.
This is well consistent with the observations made in discharge #25304 (see section 7.3).

[1] Line-averaged and line-integrated density for the central interferometer channel H-1 are practically the same (besides the unit, m^{-3} instead of m^{-2}), as the chord length through the plasma is about 1 meter.

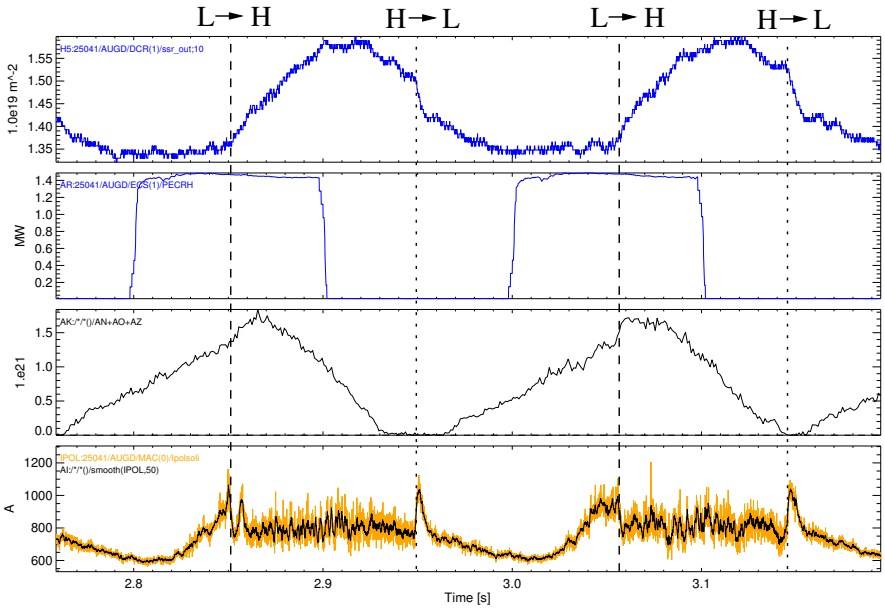

Figure 8.2: *Time traces of edge interferometer channel H-5, injected ECRH power, gas inlet rate and scrape-off layer current monitor signal (from top to bottom) for discharge #25041, which had an H-1 density of* $3.0 \cdot 10^{19}\, m^{-2}$*. In the bottom box, the orange curve represents the raw current monitor signal, whereas the black one has been averaged over 50 samples. The dashed lines mark the L-H transitions and the dotted lines the H-L transitions.*

There, real-time control of the peaking parameter was performed at a density of $3.0 \cdot 10^{19}\, m^{-2}$, using all 4 gyrotrons. When the setpoint to the peaking parameter is low, switching off ECRH results in an immediate increase of the density peaking. However, when ECRH is switched on, the peaking parameter continues rising for 50-60 ms. Only then, it starts decreasing. Again, this shows that the response of the peaking parameter is mainly due to an L-H transition, which occurs with a time delay of approximately 50 ms after turning on ECRH.
In L-mode discharges with a density of $4.0 \cdot 10^{19}\, m^{-2}$, central heating with 2 gyrotrons makes the profile more peaked. The injection of several heating pulses with all 4 gyrotrons, however, does not result in a uniform response of the peaking parameter. Figure 8.3 shows the time traces of the 5 interferometer channels, the peaking parameter p_2, the applied ECRH power and the scrape-off layer current monitor for discharge #25038 around four ECRH pulses at full power. Again, a transition to H-mode is observed. In contrast to discharge #25041, however, the onset of this transition is not fixed relatively to the beginning of the heating pulse. The first transition occurs quite at the end of the first pulse. In the following pulses, the transition occurs earlier, finally about 60-70 ms after switching on ECRH. This drift of the onset time of the L-H-transition explains the different response of the peaking parameter to the ECRH pulses. The first two do not have any significant effect, whereas the following ones cause a slight flattening of the density profile.

All in all, the following conclusion on the response of the density profile to central electron heating in L-mode discharges can be drawn: At densities up to about $2.5 \cdot 10^{19}\, m^{-2}$, central

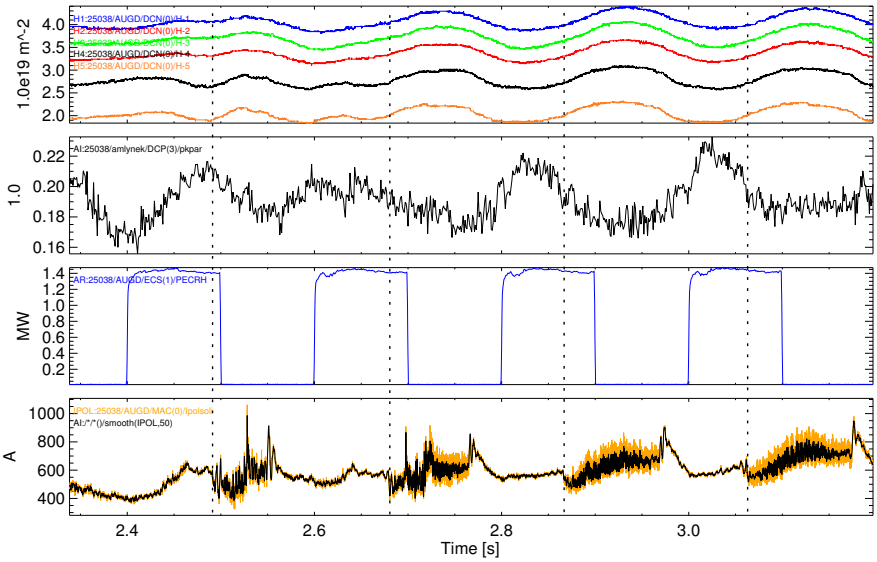

Figure 8.3: *Time traces of the 5 interferometer channels, the peaking parameter p_2, the injected ECRH power and the scrape-off layer current monitor signal (from top to bottom) for discharge #25038, which had an H-1 density of $4.0 \cdot 10^{19}\, m^{-2}$. In the bottom box, the orange curve represents the raw current monitor signal, whereas the black one has been averaged over 50 samples. The dashed lines mark the L-H transitions.*

ECRH causes a strong reduction of the core density and thus a flattening of the density profile. With increasing density, this effect becomes weaker and finally reverses sign. At $3.0 \cdot 10^{19}\, m^{-2}$, there is still a weak flattening, whereas at $4.0 \cdot 10^{19}\, m^{-2}$, central heating increases the peaking of the density profile. Most likely, a neutral point exists in between those two densities where ECRH does not cause any effect on the profile.
Figure 8.4 shows a diagram similar to figure 2.9 in chapter 2, where the peaking parameter has been plotted versus the effective collisionality ν_{eff}, which is defined by $\nu_{eff} = 0.1 n_e Z_{eff} R/T^2$ [17] [2]. The result is in agreement with the observations presented in [16] and [17]: At low collisionality, the dominant turbulence type is the trapped electron mode (TEM) and density pump-out in response to central heating is observed. At higher collisionality, however, an ITG mode becomes dominant and central heating causes a peaking of the profile.
In the experiments, this basic effect was sometimes overlaid by a transition from L-mode to H-mode. The use of 2 gyrotrons did not provide enough power to cross the H-mode threshold in any case and therefore always allowed for an undisturbed observation of the effect described above. The use of 4 gyrotrons, however, triggered a transition to H-mode when the density was around or above $3.0 \cdot 10^{19}\, m^{-2}$. At $3.0 \cdot 10^{19}\, m^{-2}$, the basic effect of ECRH is still a slight flattening of the density profile, which is strongly enhanced by the L-H transition. Therefore, reducing the peaking works well with 4 gyrotrons at this

[2] In this equation, the density n_e has to be inserted in units of $10^{19}\, m^{-3}$, the major radius R in meters and the temperature T in keV. Z_{eff} is the effective atomic number. ν_{eff} is here a global parameter, as in [17], so n_e, T and Z_{eff} are volume-averaged.

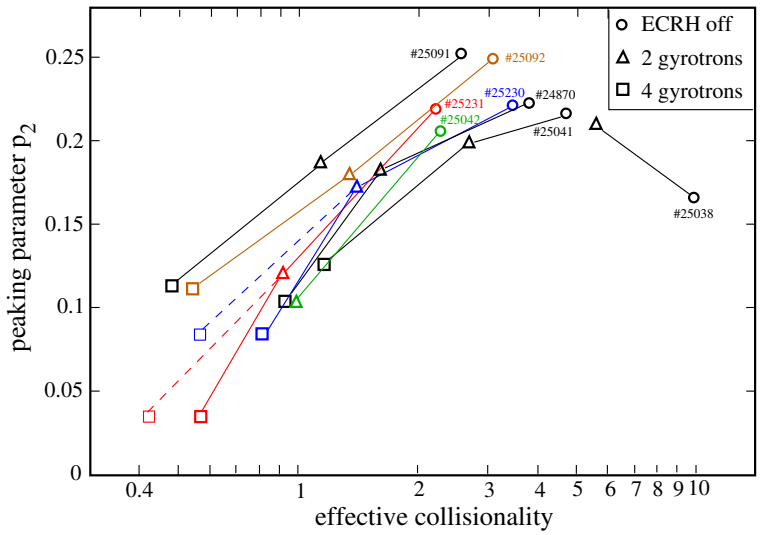

Figure 8.4: *Peaking parameter p_2 as a function of the effective collisionality. The diagram includes all L-mode discharges performed with a pre-programmed ECRH pattern, where the circles represent the cases without ECRH, the triangles the cases with 0.7-0.9 MW of ECRH and the squares the cases with 1.5 MW of ECRH. Symbols corresponding to the same discharge are connected by lines. Like in figure 8.1, the cases with constant gas level for discharges #25230 and #25231 are shown as dashed line.*

density. At $4.0 \cdot 10^{19}\, m^{-2}$, however, the basic effect has reversed and makes the density profile more peaked. The L-H-transition is now a counteracting effect and therefore, not much modulation of the density peaking is achieved. By trend, the effect of the transition to H-mode is a little stronger, resulting in a slight flattening of the profile.

8.2 Temporal evolution of density and temperature profiles in the experiments

Figure 8.5 shows the electron temperature profile of discharge #24870 as measured by the ECE radiometer at 3 different points in time. At $t = 2.2\,s$, there was only ohmic heating, at $t = 2.3\,s$, 0.85 MW of central ECRH were injected, and at $t = 2.7\,s$, there were 1.5 MW ECRH power. As one can see, central heating causes an overall increase of temperature, but the shape of the profile does not change much.
Figure 8.5 also shows the density profiles for the same discharge and the same points in time. The density profiles provided by integrated data analysis (IDA) and by the real-time algorithm do both show a flattening in the presence of central heating. The real-time code delivers a centrally hollow profile in the case with full ECRH power. IDA, in contrast, never delivers hollow profiles due to the built-in monotonicity condition, see end of section 6.5.
In the experiments performed in feed-forward mode, there were several ECRH pulses with identical duration at identical plasma parameters. This yields the opportunity to study the transient behavior of density and temperature profile. For this purpose, time windows have been selected which contain a sequence of heating pulses of identical power. For such time

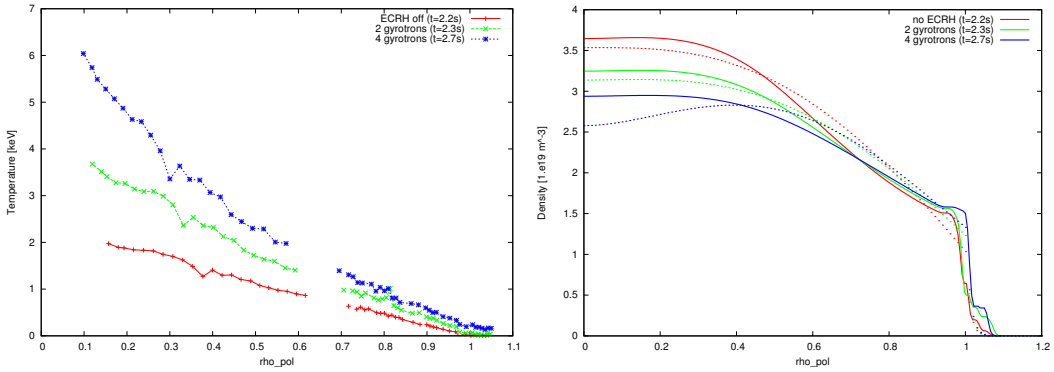

Figure 8.5: *Temperature (left) and density (right) profiles for discharge #24870 in a phase with purely ohmic heating (2.2 s, red), with 0.85 MW of ECRH (2.3 s, green) and with 1.5 MW of ECRH (2.7 s, blue). Gaps in the temperature profile are due to inactive ECE channels. The density profiles drawn with a solid line are IDA profiles, whereas the dotted lines represent the profiles delivered by the real-time algorithm.*

interval, a flux radius ρ_{pol} is chosen and the temporal evolution of the local density and temperature at this radius is calculated from the IDA profile and the ECE measurements, respectively. The response of the plasma to ECRH pulses can then be investigated in a scatter diagram in which density is plotted versus temperature. The result for discharge #25042, $\rho_{pol} = 0.5$ and $2.6\,s \leq t \leq 3.9\,s$ is shown in figure 8.6. As there is density pump-

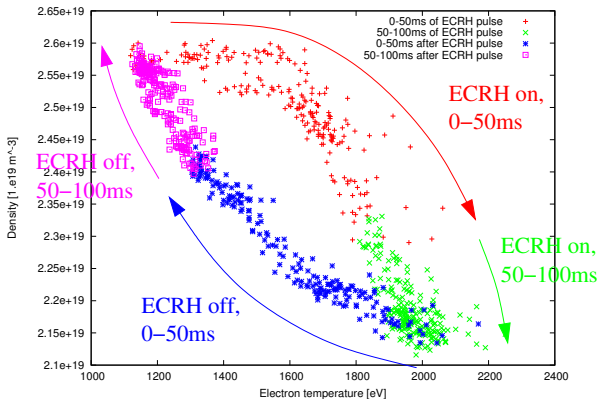

Figure 8.6: *Scatter plot of density versus electron temperature at $\rho_{pol} = 0.5$ for discharge #25042 in the time window $2.6\,s \leq t \leq 3.9\,s$, which contains 7 ECRH pulses with 0.65 MW. The data points corresponding to the first 50 ms of an ECRH pulse, the second 50 ms of the pulse, the first 50 ms after the pulse and the second 50 ms after the pulse are shown in different color.*

out in response to central heating in this discharge, the data points form a band that goes from top left (high density and low temperature) to bottom right (low density and high temperature). The remarkable feature is the formation of a hysteresis loop. The top left and bottom right end of the band represent the state of saturation when ECRH is off and on, respectively. The trajectory in the $n_e - T_e$ plane on which the system evolves

between the two states of saturation, however, depends on the direction. To illustrate the temporal order in which the hysteresis loop is passed through, figure 8.6 shows the data points corresponding to 4 different time intervals in different color: The data in the first 50 ms of an ECRH pulse is shown in red, the second 50 ms of the pulse in green, the first 50 ms after the pulse in blue and the remaining 50 ms before the next pulse in violet. This shows that the loop is run through in the clockwise direction: When ECRH is turned on, there is first a rise of temperature, and only with some delay, the density decreases. When ECRH is switched off, there is a prompt decrease of temperature, whereas the increase of density is initially much slower.
Further $n_e - T_e$ diagrams have been generated for other discharges and other radii, see figure 8.7. It can bee seen that the shape of the hysteresis loop depends on the plasma parameters. It should be noticed that the hysteresis is also present in discharges that were performed at constant gas inlet rate, such as #25092, so it is not just a secondary effect due to density feedback on the line-integrated density. In some cases, like discharge #24870 at 0.85 MW heating power, hardly any hysteresis loop can be observed within the noise level of the involved diagnostics.
An interesting case is discharge #25041 (see bottom of figure 8.7), which was performed at a density of $3.0 \cdot 10^{19}\, m^{-2}$. At an ECRH power of 0.8 MW, not much effect on the density was observed, so the bands in the $n_e - T_e$ diagram are almost horizontal. The hysteresis loops enclose only a small area and are run through in the counterclockwise direction. A heating power of 1.5 MW, however, caused a strong flattening of the density profile. The bands in the $n_e - T_e$ diagram are tilted accordingly, however, there is no significant hysteresis in the core region. Just close to the edge, e.g. at $\rho_{pol} = 0.8$, a hysteresis loop is visible again. This loop is run through in the counterclockwise direction and the states of saturation correspond to the bottom left and top right corner. This is also observed in #24870, where it is likely to be caused by increased gas puffing when the core density decreases. In case of #25041, however, the hysteresis loop at $\rho_{pol} = 0.8$ encloses a much larger area. This can be explained by the L-H transition that is triggered in this discharge: A transition to H-mode strongly increases the edge density and therefore results in a large hysteresis loop in the $n_e - T_e$ diagram for large radii.

8.3 Numerical simulation of density and temperature profile

The intention of this chapter is to explain the experimentally observed transient behavior of local density and temperature in response to heating pulses on the basis of the transport equations given in chapter 2. In the first instance, the application of central heating power results in a modification of the temperature profile. From the fact that also the density profile shows a response to the additional heating power, one learns that there exists some coupling mechanism between temperature and density. The equations for the particle flux $\vec{\Gamma}$ and the heat flux $\vec{q}_{heat}$,

$$\vec{\Gamma} \;=\; -D\vec{\nabla}n_e \;-\; C_T n_e \frac{\vec{\nabla}T}{T} \;+\; \vec{v}_p n_e$$

$$\vec{q}_{heat} \;=\; -\chi n_e \vec{\nabla}T \;+\; \vec{v}_e n_e T\,,$$

which were introduced as equations (2.1) and (2.2) in chapter 2, contain the thermodiffusion coefficient C_T, which couples the particle transport to the temperature gradient and

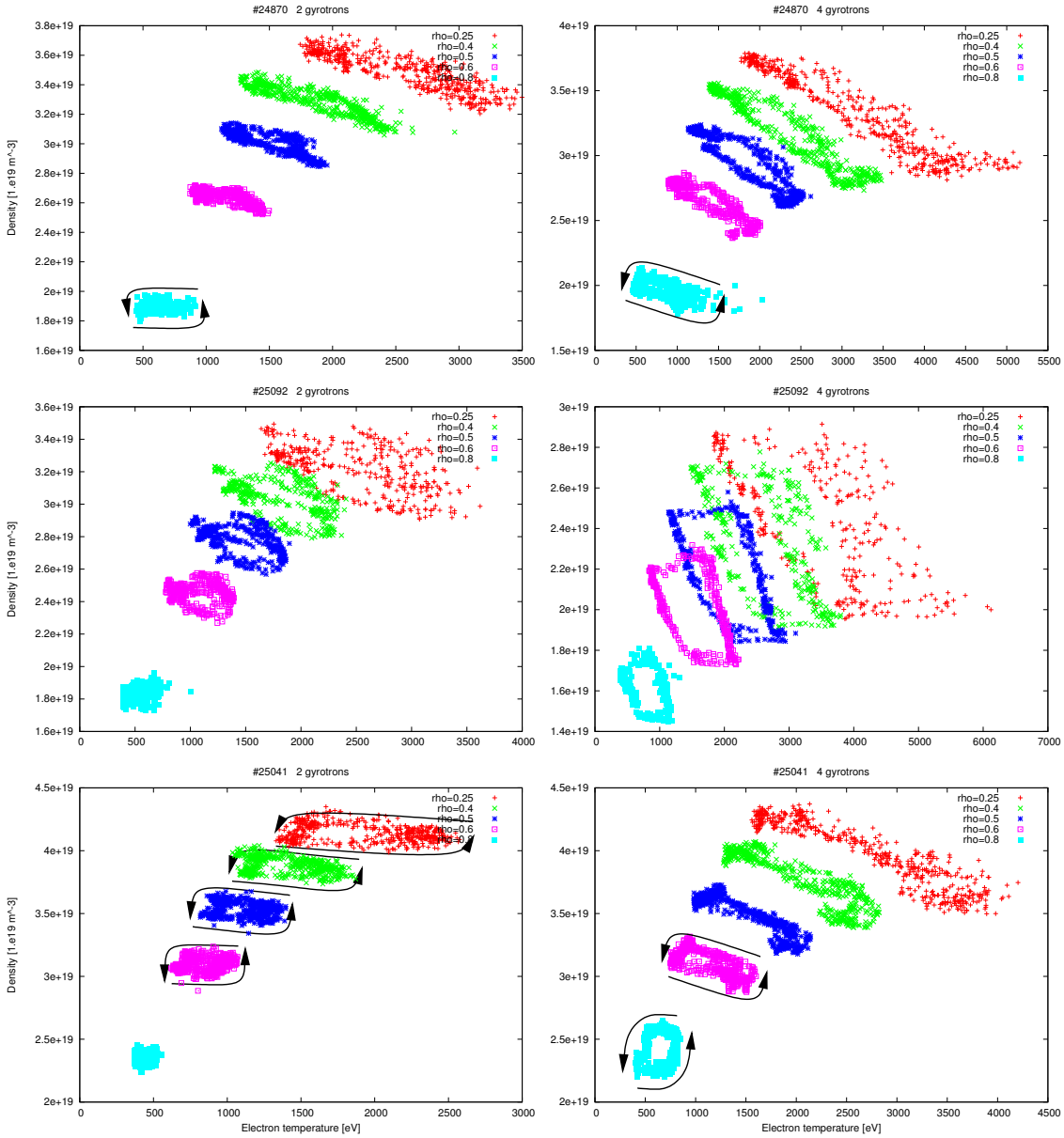

Figure 8.7: *Scatter plots for different discharges (top: #24870, center: #25092, bottom: #25041), different heating powers (left column: 2 gyrotrons, right column: 4 gyrotrons) and radii (red: $\rho_{pol} = 0.25$, green: $\rho_{pol} = 0.4$, blue: $\rho_{pol} = 0.5$, violet: $\rho_{pol} = 0.6$, bright blue: $\rho_{pol} = 0.8$). The majority of hysteresis loops is run through in clockwise direction, the exceptions are marked with arrows.*

thus the density profile to the temperature profile. However, one has to keep in mind that the transport coefficients like the diffusion coefficient D and the inward convection term $\vec{v}_P$ are not necessarily constant, but may depend on temperature and temperature gradient, which also causes a coupling to the temperature profile.
The temperature profile which occurs under stationary conditions can be calculated from the condition that the total heat flux through a flux surface is equal to the net heating power deposited inside this surface. The stationary density profile for a case without central sources, like here, is determined by the condition that the particle flux is equal to zero everywhere, i.e. the diffusion term is balanced by the sum of thermodiffusion and convection. The temporal evolution of the profiles, in contrast, is much more difficult to calculate as the conditions for the stationary case do not hold and one has to solve coupled differential equations for $n_e(\rho_{pol}, t)$ and $T_e(\rho_{pol}, t)$. For this reason, a numerical approach, which is described in detail in appendix A.3, is used to theoretically predict the time dependence of the profiles. This numerical model describes the temporal evolution of the temperature profile in a cylindrical volume which has rotational symmetry with respect to the cylinder axis. The cylindrical geometry states a good approximation also for the tokamak when assuming circular and concentric flux surfaces. In the radial direction, the volume is divided into N equidistant sections which are assumed to have each a homogeneous temperature. For a given temperature distribution, the heat flow balance for each of these sections is calculated, as well as the resulting new temperature after one discrete time step. That way, a recursion formula is obtained which allows to calculate the temperature evolution from one time step to the next. An analogous formula for the density has been derived from the above equation for the particle flux and implemented in the model. It is just a qualitative model which uses dimensionless input parameters and provides results in arbitrary units.
The simulations were performed with $N = 20$ and initially flat distributions of temperature and density. For the outermost radial section, boundary conditions for heat and particle flux have to be defined. The particle flux through the boundary area of the cylinder was set to zero, resulting in a conservation of the volume-integrated density and thus of the total number of particles in the plasma. Furthermore, the boundary of the cylinder was assumed to be connected to an infinitely large temperature reservoir of constant temperature $T_{ambient}$. This choice of the boundary conditions was motivated by the fact that in the experiments under consideration, there were no central particle sources, and in the phases of constant density, the peripheral fueling was just balanced by the particle losses at the edge. Hence, one can assume that there are no net particle sources or sinks. However, there were central heat sources, so it was not possible to exclude any heat flux through the boundary, as this would have resulted in a monotonously increasing heat content of the plasma. Therefore, a surrounding heat reservoir was introduced which can absorb the injected heating power and allow for a thermal equilibrium.

First, a constant set of transport coefficients χ, D, C_T and v_P was used. Heating power was assumed to be deposited in the innermost radial section only, which corresponds to a very centrally peaked heating profile. With those settings, some thousand time steps were calculated during which the result converges to a thermal equilibrium. The resulting density and temperature profiles are shown in figure 8.8 as green curves. As heating power is only deposited in the center, the same heat flux has to go through the boundary area of all radial volume elements. This area grows proportionally to the radius r, therefore, the temperature gradient has to have roughly a $1/r$ dependence (this is only an approximation, due to the n_e dependence of the heat flux, see equation (2.2) in chapter 2). Accordingly,

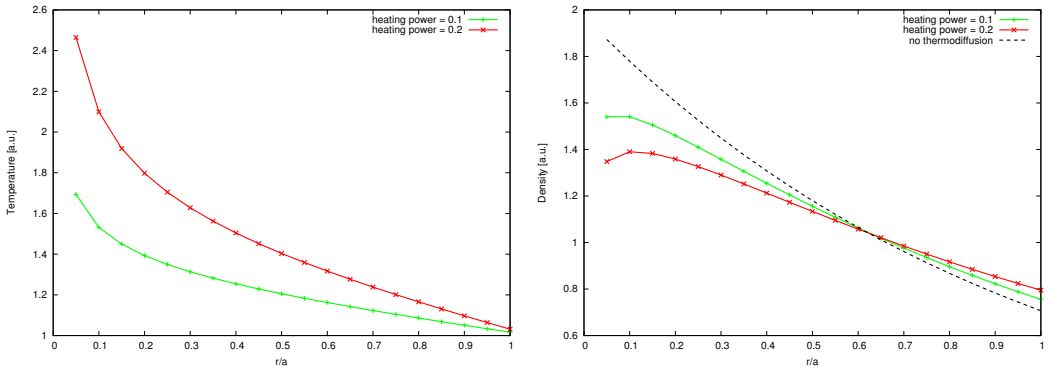

Figure 8.8: *Simulated temperature profile (left) and density profile (right) with* $N = 20$, $\chi = 0.01$, $D = 0.01$, $C_T = 0.005$, $v_P/N = 0.0005$ *and* $T_{ambient} = 1.0$. *The central heating power is* $P_{heat} = 0.1$ *(green curves) or* $P_{heat} = 0.2$ *(red curves), respectively. The dashed black line in the right diagram represents the case* $C_T = 0$, *which is identical for any applied heating power.*

the temperature profile is approximately a logarithm function[3]. The density profile would be rather peaked in the absence of thermodiffusion (see dashed line in figure 8.8), as a result of the inward pinch term v_P. With non-zero thermodiffusion coefficient C_T, however, the density profile is rather flat in the center due to the strong temperature gradient. The result of doubling the heating power is also illustrated in figure 8.8 in red: The temperature globally increases, but the shape of the temperature profile remains the same. The density profile, in contrast, flattens and even becomes slightly hollow in the central region. This is a very simple numerical model with static transport coefficients, which would, for example, fail to produce stiff temperature profiles in case of off-axis heating. In addition, there is no mechanism built in which ensures that density profiles have zero derivative in the center. But nevertheless, the calculated effect of increased central heating power on temperature and density profile is in qualitative agreement with the experiments.
As the next step, a simulation of the temporal evolution of the density profile was performed. For the chosen coefficients χ and D, it takes a little more 1,000 time steps until the simulated temperatures and densities converge to a static value. The simulation is started with low heating power in the center and 3,000 time steps are calculated. Then, the heating power is doubled and further 3,000 steps of calculation are performed. After this, heating power is set back to the original value and 4,000 further time steps follow. The resulting time traces of temperature and density at the radial location $r/a = 0.35$ are shown in figure 8.9. The temperature starts rising when the central heating power is increased and then asymptotically approaches to its new saturation level. The local density, however, first starts rising for several time steps before it drops and evolves towards a new saturation level which is lower than the previous value. When the heating power is reduced again, the same happens with opposite sign, i.e. there is again an initial change of density which goes away from the new saturation level. This initial overshooting of density becomes weaker at lower radii. As the density profile flattens in the center when heating

[3]Mathematically, its discontinuity in the limit $r \to 0$ can be understood as follows: Heating power is assumed to be deposited in the innermost volume element only. In the limit $N \to \infty$, this is equivalent to a Dirac-Delta like distribution of the heating power located at $r = 0$. This requires an infinite temperature gradient at $r = 0$.

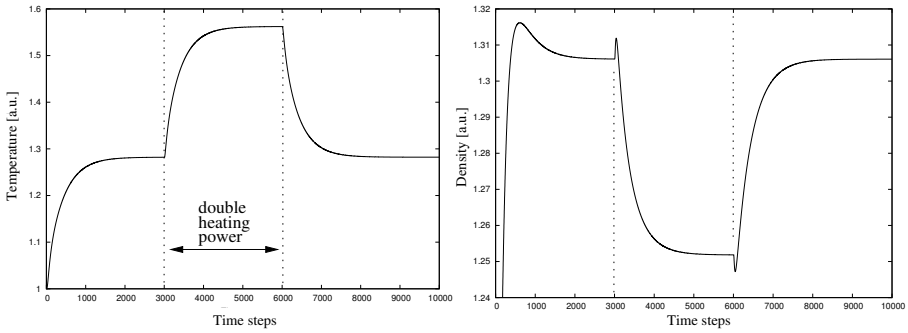

Figure 8.9: *Simulated time trace of temperature (left) and density (right) at r/a=0.35 when heating power is increased from 0.1 to 0.2 at time step 3,000 and reduced to 0.1 at time step 6,000. All other parameters are the same as those used in figure 8.8.*

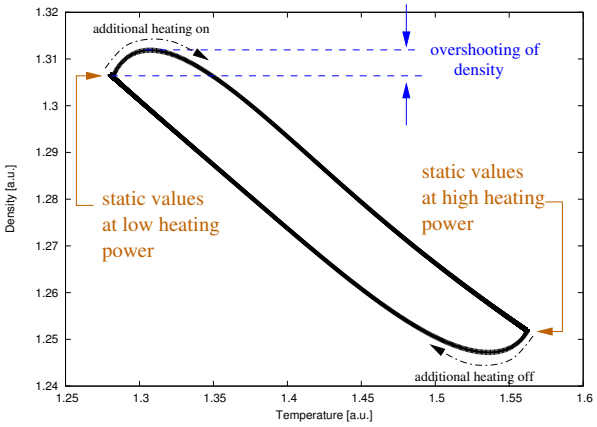

Figure 8.10: *Simulated density versus temperature at r/a=0.35, using the data from figure 8.9.*

power is increased, particles have to move from the center to the edge. At mid-radius, the flattening of the profile still corresponds to a decrease of density, however, shortly after the increase of the central heating power, the particles expelled from the center arrive there, resulting in a temporary increase of density. In figure 8.10, the local density at $r/a = 0.35$ is plotted versus the local temperature for time indices 2,000 to 10,000. The model yields a hysteresis loop which is run through in the clockwise direction. In principle, this is in agreement with the experimental observations, however, the shape of the actual hysteresis curve is different. Whereas the model predicts an initial rise of density right after turning on central heating, which is followed by a longer decay phase, the experimental curves remain at constant density in the beginning and do then start dropping.
Therefore, it was attempted to find a set of transport coefficients which provide a more realistic description of the hysteresis loop. As the coupling between temperature and density provided by the thermodiffusion coefficient C_T yields an initial overshooting of the density at mid-radius, a different coupling scheme is used: The coefficient C_T is set to zero, but a temperature dependence of the inward convection coefficient v_P is introduced. This is motivated by the fact that the thermodiffusion coefficient C_T, which causes a particle flux

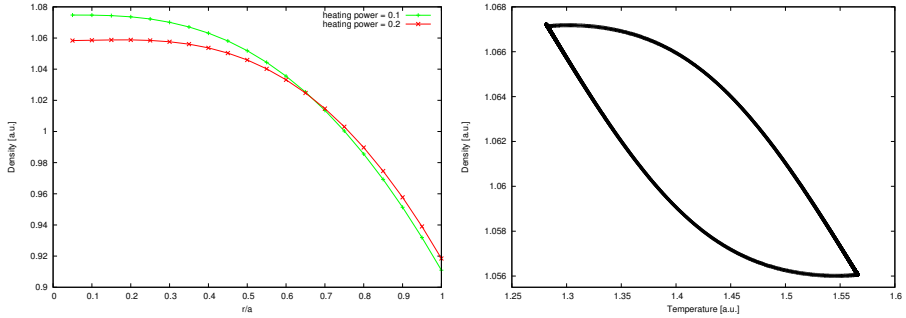

Figure 8.11: *Left: Simulated density profiles with $C_T = 0$, but a temperature- and radius-dependent pinch term $v_P = 0.0005 \cdot (1 - T/2.0)\, r^{1.5}$. The other parameters are identical to those given in the caption of figure 8.8. The green curve represents the case $P_{heat} = 0.1$ and the red curve $P_{heat} = 0.2$. Right: Resulting curve in the $n_e - T_e$ plane for r/a=0.35 when heating power is switched from 0.1 to 0.2 and back.*

directed outwards in cases where a TEM is dominant, was found to strongly increase with an increasing ratio of electron to ion temperature T_e/T_i [16]. The normalized (electron) temperature gradient $\nabla T/T$, however, is reported to remain almost unchanged when localized electron heating is applied to the plasma center [41], due to the stiff behavior of the plasma temperature profiles. For this reason, the thermodiffusion term in the equation for the particle flux $\vec{\Gamma}$ mainly varies due to the temperature-dependence of C_T rather than due to changes of the normalized temperature gradient. To achieve more realistic modeling, it is therefore reasonable to neglect the dependence on the temperature gradient and describe the coupling between density and temperature profile by means of a purely temperature-dependent term. This can be done with $C_T = 0$ and a convection term v_P that is proportional to $(1 - T/T_0)$, where the constant 1 represents the inward pinch and the T-dependent part provides the desired coupling to the temperature profile.
The density profiles obtained with static transport coefficients in general had non-zero derivative in the center. To avoid this, an additional radius dependence of v_P was added which goes to zero in the limit $r \to 0$. It was found that with the ansatz $v_P = v_{P0}(1 - T/T_0)\, r^{1.5}$, more realistic density profiles are obtained, as well as hysteresis curves in the $n_e - T_e$ plane which are in better agreement with the experimental results, see figure 8.11. The initial overshooting of density is negligible, so that the curve is almost parallel to the temperature axis right after changing the heating power. The area enclosed by the hysteresis loop grows with the ratio of heat conductivity χ and diffusion coefficient D, as figure 8.12 illustrates. The radial dependence of the simulated hysteresis curve is shown in figure 8.13.

With this simple numerical model, it has been shown that the occurrence of a hysteresis curve in the $n_e - T_e$ diagram in response to sudden changes of the central heating power can be reproduced on the basis of the transport equations (2.1) and (2.2) in chapter 2, even with static transport coefficients. In that case, the coupling between density and temperature is provided by the thermodiffusion coefficient C_T. Alternatively, a dependence of the transport coefficients on temperature (or temperature gradient) can be introduced, by which one obtains a large number of degrees of freedom for modeling. It has been shown that by using a temperature-dependent and radius-dependent inward pinch coefficient $v_P = v_P(T, r)$ and

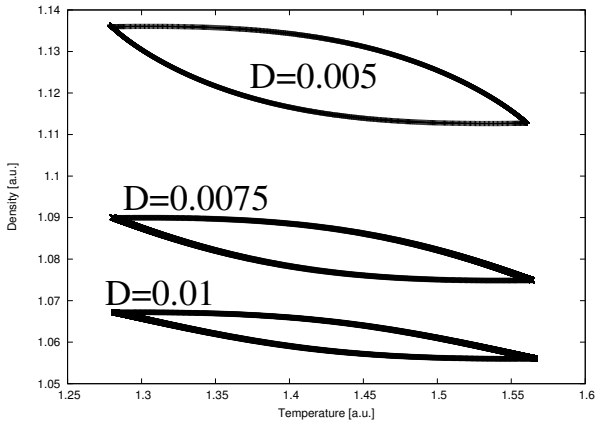

Figure 8.12: *Impact of the ratio χ/D on the area enclosed by the hysteresis curve. The diffusion coefficient D is varied, whereas all other parameters are identical to those used in figure 8.11. The vertical offset of the curves is due to the fact that a reduction of D makes the profiles more peaked.*

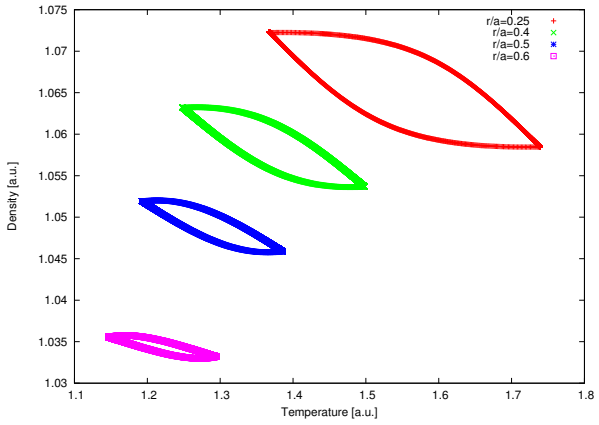

Figure 8.13: *Radial dependence of the hysteresis loop. For the parameters used in figure 8.11, the curve is shown at r/a=0.25 (red), 0.4 (green), 0.5 (blue) and 0.6 (violet).*

neglecting the thermodiffusion term, a more realistic description of the experimental data than with static coefficients can be achieved: The shape of the hysteresis loop delivered by the simulation is consistent with the experiments, its radial dependence is correctly reproduced and a variation of the area enclosed by the loop is predicted when the parameters D and χ change.
This leads to the conclusion that the analysis of the transient behavior in density pump-out experiments can provide more information on the ratio of the transport coefficients and their dependence on local quantities such as temperature than just a study of the stationary density and temperature profiles. By performing quantitative simulations with more advanced transport codes such as the ASTRA[4] package, it should be possible to reproduce the large variety of curves in figure 8.7 and gain a more detailed picture of the underlying transport phenomena. However, within the scope of this thesis, whose main focus was on the demonstration of real-time control of the density profile, it was not possible to carry out simulations with this much more complex code.

[4] **A**utomatic **S**ystem for **TR**ansport **A**nalysis

9 Summary and Outlook

In this thesis work, it has been experimentally demonstrated that the shape of the plasma density profile in ASDEX Upgrade discharges can be actively controlled with a feedback loop in which the actuator is central electron cyclotron resonance heating (ECRH). Depending on the plasma parameters, peaking or flattening of the profile can be achieved. This is the first demonstration of feedback profile control in ASDEX Upgrade and provides the basis for other feedback possibilities in the future. The requirements for successful feedback control are:

- A reliable density measurement
- Fast calculation of the density profile
- A real-time magnetic equilibrium
- Real-time data transfer to the control system
- An actuator capable of modifying the density profile

The first step on the way to feedback control was the creation of the technical basis for the real-time calculation of the density profile. This profile is calculated from the 5 line-integrated density measurements provided by the sub-millimeter interferometer, which, however, may be affected by measurement errors, so-called 'fringe jumps'. The development and construction of new readout electronics for the interferometer allowed for the definition of a reliable real-time detection criterion for fringe jumps, which ensures that no density profile distorted by spurious density signals is used for feedback control. The faster response of the new electronics to rapid changes of density also provides new opportunities, such as the observation of sawtooth instabilities and their precursor oscillations. This, however, was not investigated in more detail here.
Another major part of this work was the development of a fast but sufficiently accurate computer algorithm which calculates the density profile from the 5 line-integrated measurements, taking into account the magnetic equilibrium. The density profile is parameterized as a fourth degree polynomial of the normalized poloidal flux radius, and the line-integrated densities along the 5 lines of sight are calculated as a function of the polynomial coefficients. The set of coefficients that provides best consistency with the measurement is then determined via least squares approximation. On the one hand, the numerical complexity of this algorithm was kept low to run in real-time on present-day computers (computation time $<1\,\mathrm{ms}$), and on the other hand, the resulting density profiles are in good agreement with profiles calculated by more complex offline algorithms. After setting up a real-time data network which allows for the communication of the density profile to the control system

during the discharge, experiments for real-time control of the density profile were carried out. From the density profile, which was calculated each millisecond, a scalar peaking parameter was derived and used as input to a feedback control loop.
As an actuator for modifying the shape of the density profile, central electron cyclotron resonance heating (ECRH) was used. In preparatory experiments, the effect of this heat source on the profile was explored with a pre-programmed heating pattern to define the operational window for the feedback control experiments. It was found that central electron heating reliably and reproducibly causes a reduction of the core density and thus a flattening of the density profile in low density L-mode discharges, which, according to the literature, coincides with a trapped electron mode (TEM) being the dominant instability. When going to higher collisionality, which is accompanied by a transition to a plasma regime where an ion temperature gradient (ITG) mode dominates, the effect becomes weaker and finally reverses sign, making the profile more peaked. Above a certain power threshold, central heating triggers a transition to high confinement mode (H-mode), which results in a flattening of the profile and thus enhances or weakens the initial effect, depending on plasma parameters. On this basis, feedback control of the density profile in L-mode discharges was successfully demonstrated. The achievable amount of flattening was limited by the available ECRH power of 1.5 MW.
Also in H-mode, experiments were carried out. In literature, past experiments on ASDEX Upgrade are reported in which a flattening of the density profile by ECRH was achieved in low-density H-mode discharges. However, it was found that such experiments cannot be reproduced at present, as the installation of an all-tungsten first wall prevents one from accessing the operational regime with low collisionality required for such "pump-out" experiments. However, a set of plasma parameters in H-mode could be identified for which central heating increases the peaking of the density profile. That way, feedback control could also be performed in H-mode. All in all, it has been shown that active feedback control is possible and the density profile can be adjusted to the desired shape within the capabilities of the actuator. An unavoidable secondary effect of density profile control with ECRH, however, is a variation of the temperature profile.
Due to the large number of ECRH pulses, the preparatory experiments provided a very good basis for particle transport studies, as the transient behavior of the density profile in response to the heating pulses could be investigated. This analysis revealed that especially at mid-radius, the density responds more slowly to steps in the applied heating power than the temperature, resulting in a hysteresis curve in the density-temperature diagram. The shape of this curve, the area enclosed by it and the direction in which it is run through depends on the plasma parameters and the radial position. A large variety of such curves was observed in the experiments.
A simple one-dimensional numerical transport model has been developed, which includes the main characteristics of heat and particle transport. It was shown that the occurrence of a hysteresis loop in the density-temperature diagram can be simulated on the basis of the transport equations for heat and particles already with a set of constant transport coefficients. However, by assuming that the coupling between temperature and density profile is provided by a temperature-dependent inward convection term, a hysteresis loop is simulated whose shape is much better consistent with the experimental observations. The agreement of simulated and measured density profiles, temperature profiles and hysteresis loops suggests that such a temperature dependence of the convection velocity, which has been postulated by theory, exists.

The work presented here can be extended in the near future along both, the transport physics line and the real-time line. The large variety of hysteresis curves observed in the experiments deserves to be investigated in more detail by applying more complex, quantitative transport simulation codes such as ASTRA, as this promises to provide a deeper insight into the underlying processes of heat and particle transport. In addition, it is desirable to perform gyrokinetic calculations of turbulence stability to identify the most unstable mode in the experiments, especially the respective role of TEM and ITG as well as possible transitions during the heating pulses.
On the experimental side, future ASDEX Upgrade campaigns will provide extended possibilities for peaking control as additional gyrotrons are being installed and the ECRH power limitation of 1.5 MW will be increased to 4 MW by the end of 2010.
Further development of the algorithm for density profile calculation can be envisaged. As illustrated, the density profiles provided by the current real-time algorithm mainly differ from those calculated by more complex offline algorithms in the edge region, which can be understood from the fact that the offline codes also include edge diagnostics such as lithium beam impact excitation spectroscopy. In the near future, when also edge diagnostics such as the mentioned lithium beam diagnostic, the reflectometer and the Thomson scattering diagnostic meet the technical requirements for real-time data transfer, the algorithm may be extended to include also edge measurements.
In addition, further applications of real-time density profile determination besides active profile control are foreseen. One of them is the active stabilization of neoclassical tearing modes (NTMs), a magneto-hydrodynamic instability which occurs on flux surfaces with a rational safety factor q, most frequently at $q = 3/2$ and $q = 2/1$. As NTMs cause a reconnection of field lines and therefore deteriorate the confinement quality of the plasma and thus the fusion performance of a future power plant, it is desirable to have a tool for active NTM stabilization. Stabilization can be achieved with the help of the ECRH system by locally driving a current on the affected rational flux surface (so-called electron cyclotron current drive). This, however, requires precise steering of the ECRH launcher so that the right flux surface is hit. As the beam does in general not propagate along a straight line in the plasma due to refraction, this requires a ray tracing calculation to be performed in real-time. This is only possible when the density profile is known. For this reason, the interferometer with the real-time algorithm for profile calculation is going to be part of a rather complex network of real-time diagnostics for active NTM stabilization.

A Appendix

A.1 The sawtooth instability

Besides transport perpendicular to the field lines, the confinement quality of fusion devices is also limited due to large-scale magneto-hydrodynamic (MHD) instabilities, which can result in a reconnection of magnetic field lines on different flux surfaces which are normally well separated from each other, resulting in a shortcut of different confinement regions. This causes rapid energy and particle exchange. An important MHD instability, the so-called sawtooth instability, is briefly discussed here.

The sawtooth instability, which limits the core confinement in a tokamak plasma, represents the case $q = 1$, where q is the safety factor, see definition in section 3.1. Theoretically, it has been found that a magnetic configuration with a core safety factor $q < 1$ is unstable. In a standard tokamak scenario, the q factor in the center is around one and typically increases towards the edge to a value around 3-4. Under a wide range of operating conditions, one observes an increase of the current density in the center, which makes the safety factor drop below one. This makes the configuration unstable and results in fast magnetic reconnection inside the $q = 1$ surface. As a result of this, the profiles of density and temperature are suddenly flattened [7]. At the same time, the current density in the center rapidly decreases. After this collapse, the current density increases continuously, until the next collapse occurs. That way, there is a periodic process, which is characterized by a slow increase and a sudden drop of the core density and temperature. As the corresponding time traces have a sawtooth-like shape, this instability is called the 'sawtooth instability'. The magnetic reconnection takes place in a very narrow layer. The hot core inside the $q = 1$ surface is displaced and moves towards this reconnection layer, see figure A.1. The radius of the remaining core decreases and the reconnected flux forms an island with flat temperature distribution which grows and finally fills the whole reconnection zone. When observing the process at a fixed toroidal location, one sees a rotation of the hot core and the cold island, which is also illustrated in the figure.

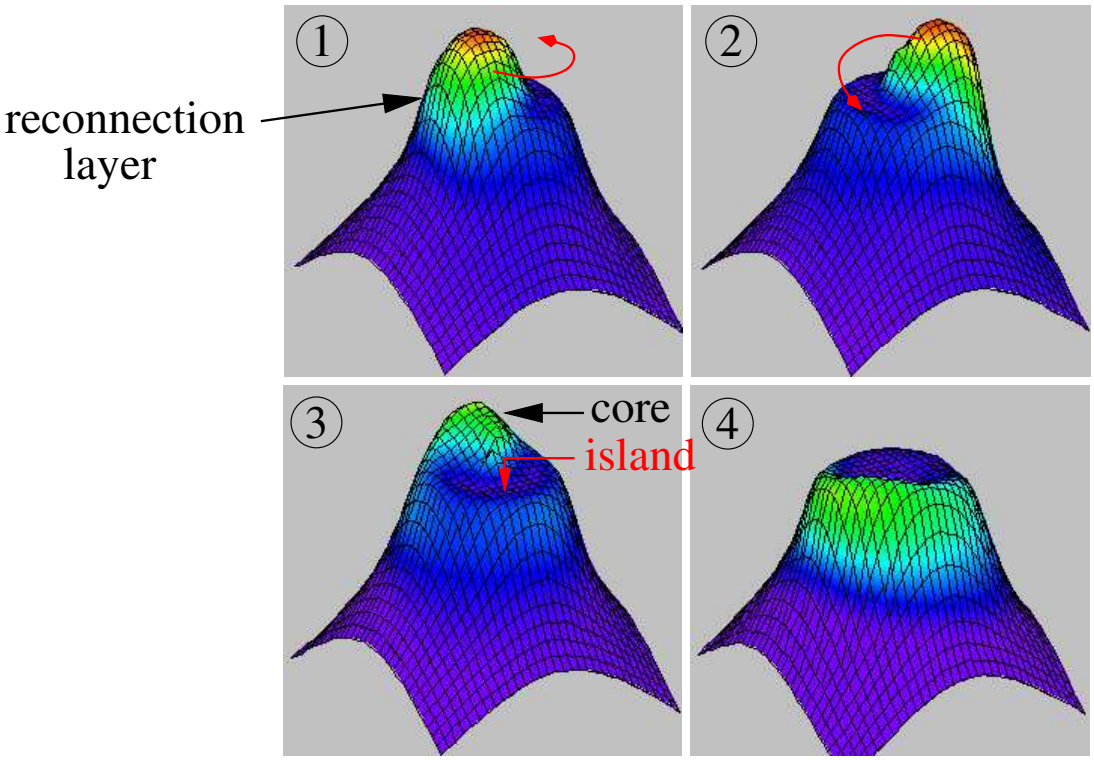

Figure A.1: *Graphical representation of a simulated temperature profile for a TFTR discharge during a sawtooth crash. The hot plasma core is displaced, which is accompanied by the appearance of a cold island. Both, core and island, rotate inside the $q = 1$ surface. After the crash, the whole temperature profile inside the reconnection zone is flat. [42]*

A.2 The vertical $CO_2/HeNe$ interferometer on ASDEX Upgrade

For the vertical channels, a CO_2 laser with a wavelength of $10.64\,\mu$m is used. As there are many transitions between rotational and vibrational states of the CO_2 molecule that correspond to wavelengths in the $9-11\,\mu$m range, the laser is equipped with an optical grating inside the resonator for line selection. In order to apply the heterodyne principle, the laser beam has to be split and one component has to be frequency-shifted. For this purpose, an acousto-optic modulator (AOM) is used. This device consists of a quartz crystal with an acoustic transducer on top. Sound waves are injected into the crystal, resulting in periodic compression and expansion of the material along the direction of sound propagation. That way, the refractive index of the material is locally increased and reduced. On a light beam propagating through the quartz perpendicular to the sound wave, this has the same effect as an optical grating. For some applications like active laser mode-locking, a sound

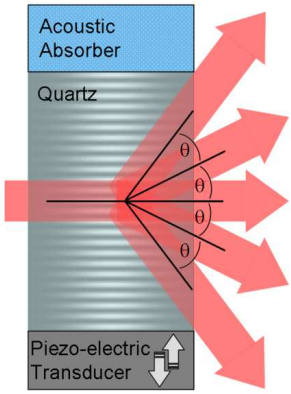

Figure A.2: *Schematic of an acousto-optic modulator. [43]*

reflector is attached to the crystal, resulting in a standing wave. That version has the properties of an optical grating that is at rest, but appears and vanishes periodically. For frequency shift applications, however, there is a sound absorber at the other end of the crystal. Effectively, this is like a grating that moves through the crystal at sound speed v_s. The slit pitch d is determined by the sound frequency f_s as $d = v_s/f_s$. If a light beam enters the crystal perpendicular to sound propagation and is diffracted by this grating, the zeroth order behaves the same as in case of a grating at rest, as the velocity of the grating has no component along the direction of propagation of the light. However, for all higher orders, there is a non-vanishing component $v_{||} = v_s \sin\alpha$, resulting in a Doppler shift of the frequency. As the condition for the k^{th} order of constructive interference for a grating of pitch d is given by $k\,\lambda = d \sin\alpha$, $v_{||}$ can be written as

$$v_{||} = v_s \cdot \frac{k\,\lambda}{d} = k\,\lambda f_s\,.$$

The corresponding Doppler shift $\Delta\omega$ of the laser light is (in first order of Taylor expansion) given by

$$\Delta\omega = \omega\,\frac{v_{||}}{c} = \omega\,\frac{k\,\lambda f_s}{c} = 2\pi\,k\,f_s = k\,\omega_s\,, \tag{A.1}$$

which means that the angular frequency of the sound wave ω_s is simply added k times to the angular frequency of the light.

For the vertical interferometer channels, a C-shaped frame around the torus is used to mount all optical components (see figure 4.7 in section 4.4), providing entire mechanical decoupling from the plasma vessel. But due to the short wavelength, the system is highly sensitive to any small deformation of the C-frame structure during plasma discharges. Therefore, a compensation system is required, which uses a 632.8 nm Helium-Neon laser. The infrared beam from the CO_2 laser and the visible beam from the HeNe laser are sent to individual acousto-optic modulators which are operated at 40 MHz. Then, the two frequency-shifted beams are superimposed in a beam splitter, as well as the two unshifted beams leaving the AOMs in 0^{th} order of diffraction (see figure A.3). One of the resulting beams is split into

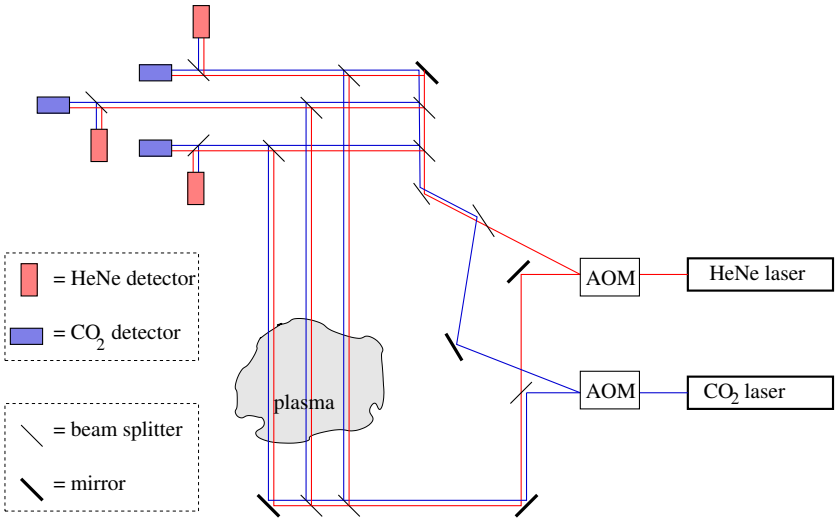

Figure A.3: *Schematic setup of the CO_2 interferometer. For convenience, the superimposed beams from CO_2 and Helium-Neon laser have been drawn with slight offset here. In the real interferometer, they lie in each other.*

3 components and sent through the plasma vessel along 3 different chords, the other one is just split. After combination of frequency-shifted and unshifted beams in 3 beam splitters, each resulting beam in analyzed in two different detectors. One of them is only sensitive to the CO_2 wavelength, the other one to the HeNe wavelength. It has been found that simultaneous adjustment of all 3 interferometer channels is rather difficult due to the small beam waist and the long optical paths. Although parallel operation of all 3 channels has been temporarily achieved in the past, the effort of doing so in daily operation turned out to be too high due to thermal drift problems. Therefore, only 2 channels which are labeled as V-1 and V-2 are operated simultaneously. If required, an additional mirror can be inserted so that the interferometer operates on a third line of sight, labeled as V-3, exclusively. It is worth mentioning that there is no reference beam in the CO_2/HeNe system. This is due to the fact that the sound emitter inside the acousto-optic modulator has to be driven by an external oscillator whose output signal can directly be used as reference. Phase comparison between this signal and the beat signal from the detector allows optical path calculation. Changes in the optical path result from changes of plasma density and from mechanical

path variations ΔL. Therefore, equation (4.6) becomes:

$$\varphi_{CO_2} \;=\; \lambda_{CO_2}\, r_e \int\limits_0^L n_e(x)\, dx \;+\; \frac{2\pi}{\lambda_{CO_2}}\, \Delta L$$

The analog equation is valid for the phase shift φ_{HeNe} of the Helium-Neon laser. All in all, there are two measured phase shifts and two unknown variables, the plasma density and ΔL. By multiplying one of these equations by the ratio of the laser wavelengths and subtracting it from the other, the mechanical path variation ΔL can be eliminated and we get

$$\varphi_{CO_2} \;-\; \frac{\lambda_{HeNe}}{\lambda_{CO_2}}\varphi_{HeNe} \;=\; \lambda_{CO_2}\, r_e \int\limits_0^L n_e(x)\, dx \;-\; \frac{\lambda_{HeNe}^2}{\lambda_{CO_2}}\, r_e \int\limits_0^L n_e(x)\, dx\,.$$

So the solution for the line-integrated electron density is given by

$$\int\limits_0^L n_e(x)\, dx \;=\; \frac{1}{r_e}\, \frac{\lambda_{CO_2}}{\lambda_{CO_2}^2 \;-\; \lambda_{HeNe}^2} \cdot \left(\varphi_{CO_2} \;-\; \frac{\lambda_{HeNe}}{\lambda_{CO_2}}\varphi_{HeNe}\right)\,. \qquad \text{(A.2)}$$

As $\lambda_{HeNe}^2 << \lambda_{CO_2}^2$, the factor in front of the brackets can be replaced by $1/r_e\lambda_{CO_2}$ in good approximation.

The readout electronics for the CO_2 system has mainly two tasks: Firstly, it receives the 40 MHz reference oscillator and probe signals from the CO_2 and the $HeNe$ system and calculates the phase shifts. Secondly, it calculates the plasma density from both phase shifts according to the above equation. The signals from the detectors and from the frequency generator that drives the acousto-optic modulators are (almost) sinusoidal. They are sent through comparators in order to generate square wave signals. The two signals (plasma and reference signal) from the CO_2 system are sent to 4-bit binary counters, so the frequency is divided by 16. Now, a set-reset flip-flop is supplied with the counter outputs (see figure A.4). A rising edge of the reference signal sets the flip-flop and a rising edge of the plasma signal resets it. The output of the flip-flop is a square wave signal whose duty cycle depends on the relative phase of plasma and reference signal. Sending it to a low-pass filter results in a DC voltage that is proportional to this duty cycle and thus to the phase shift of plasma and reference signal. The dynamic range of this phase detector is 16 fringes. The phase counter for the Helium-Neon system is just the same, with the only difference that an 8-bit binary counter is used, so the frequency is divided by 256 and therefore the dynamic range of the counter is 256 fringes. Consequently, two analog voltages are available now, one of them being proportional to $\varphi_{CO_2}/16$ and the other to $\varphi_{HeNe}/256$. In order to calculate the plasma density, φ_{HeNe} times the ratio of the two wavelengths (1/16.748) is needed according to equation (A.2). As the binary counter for the HeNe system is 4 bits longer, there is an additional division by 16 compared to the CO_2 system. Therefore, just further multiplication of the resulting voltage by $16/16.748 = 0.955$ is required before the voltages from the CO_2 branch and the HeNe branch can be subtracted. These two steps are performed with an analog circuitry that is based on several operational amplifiers. The resulting output voltage is proportional to the line-integrated electron density. The preload function of the binary counters allows to set the density output to a defined zero level before the plasma discharge starts.

Per interferometer channel, 3 signals are digitized and stored for every plasma discharge:

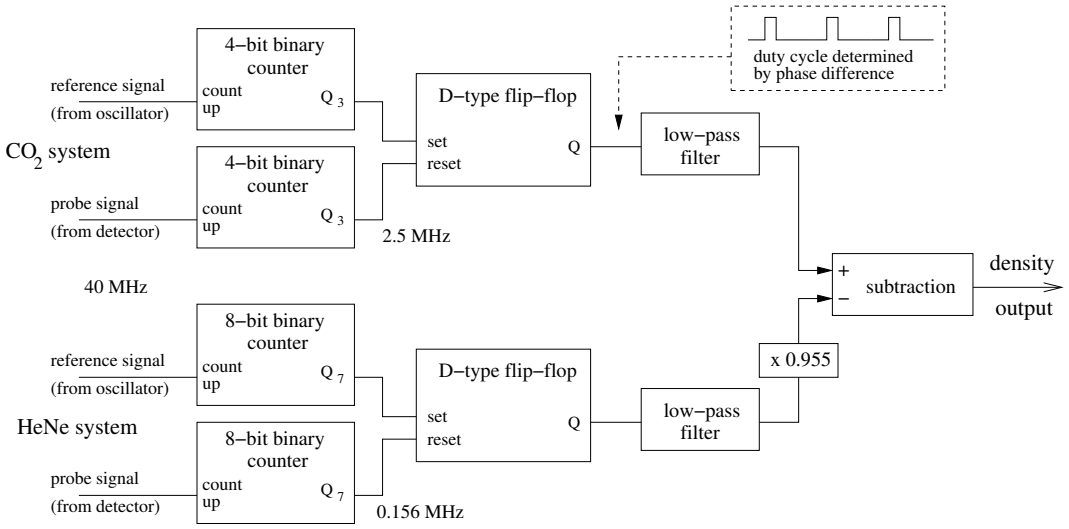

Figure A.4: *Schematic diagram of the readout electronics for the CO_2 interferometer.*

The phase output of the CO_2 system, the phase output of the HeNe system and the density output signal. Figure A.5 shows an example of this. It is remarkable that mechanical variations of the path length dominate the signals of the two sub-systems. CO_2 and HeNe signal have very similar shape, which represents vibrations of the C-frame. Just the very small difference between those two signals contains the desired information on plasma density.
In addition, it can be seen that the noise level of the resulting density signal is rather high. After the end of the plasma discharge after a bit more than 8 seconds, there is a zero line that is affected by noise with an amplitude on the order of $10^{19}\,m^{-2}$. This noise mainly contains frequencies in the range of 200 Hz to 1 kHz, which is most probably caused by the vibration of vacuum pumps in the close vicinity of the interferometer. The method of vibration compensation is based on the assumption that geometric path variations are the same for CO_2 and $HeNe$ branch, which is certainly true as soon as both beams have been superimposed in a beam splitter. However, path variations that occur between the acousto-optic modulators and the beam splitter, cannot be compensated. In contrast to other fusion experiments with two-color interferometers, like the DIII-D tokamak in San Diego/USA, where the optical path between the acousto-optical modulators and the beam splitter was kept as short as possible and all components in between were mounted on a common optical table [44], the spatial separation of those components is rather large on ASDEX Upgrade. This is most probably the reason for the incomplete vibration compensation. The noise level of the density signal can be dramatically reduced by averaging it over a period of about 5 milliseconds, which, of course, reduces the temporal resolution.
The big advantage of the $CO_2/HeNe$ interferometer compared to the DCN system is its insensitivity to any strong density gradients in the plasma, as beam refraction does not play a role at the given wavelengths. In addition, the high modulation frequency of 40 MHz makes it possible to study fast phenomena in the plasma, at least when their frequency is much higher than that of the background noise. As the phase shifts caused by density variation are less than 2π for both wavelengths, this interferometer system can easily follow fast changes of density like those caused by pellet injection or disruptions.
Whereas plasma phenomena cannot induce any fringe jumps in this interferometer system,

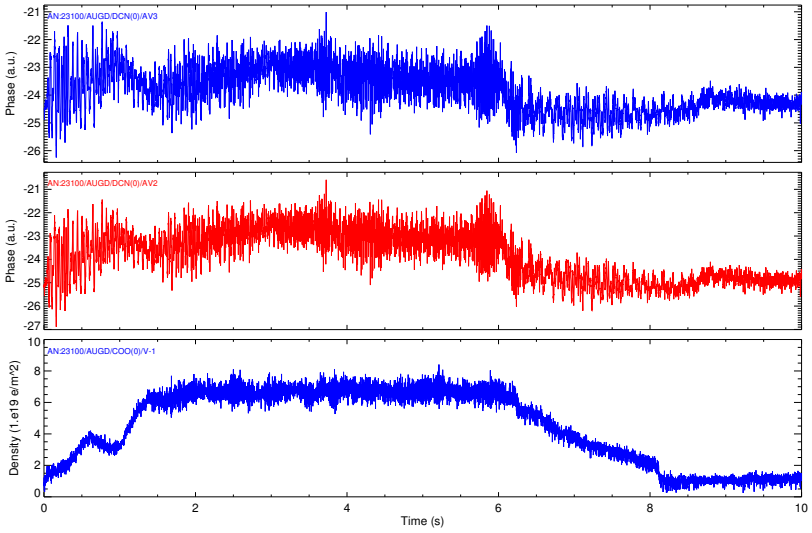

Figure A.5: *Time traces for CO_2 interferometer channel V-1 in ASDEX Upgrade discharge #23100. The upper curve is the phase for the CO_2 branch, the middle one for the HeNe branch, and the lower graph shows the resulting density signal in electrons per m^2.*

jumps due to electric cross-talk are sometimes observed. Some fringe jumps are directly correlated in time with the switching-on or switching-off of the neutral beam heating. In addition, whole series of fringe jumps in the infrared branch of channel V-2 have been temporarily observed which are perfectly correlated in time with the switching of the beam chopper of the lithium beam diagnostic. The main disadvantage of this interferometer system is the high noise level of the output signals and the very limited number of lines of sight. For this reason, the DCN signals are usually preferred for physics analysis, like the calculation of density profiles that will be presented in this thesis. Just for studying fast phenomena, like the effect of massive gas injection for disruption mitigation or the measurement of toroidal Alfven eigenwaves, the CO_2 system with its much higher beat frequency is used. In addition, the CO_2 interferometer provides a good fallback solution for the case that the DCN interferometer can no longer properly measure the plasma density.

A.3 A simple numerical heat and particle transport simulation

The following approach allows for a simulation of the radial heat and particle transport in a cylindrical volume, where rotational symmetry with respect to the cylinder axis is assumed. When neglecting the Shafranov shift, it is also applicable to a torus. The radius of the cylinder will be labeled a, which is equivalent to the minor radius in case of toroidal geometry. The length of the cylinder will be referred to as L, which has to be replaced by $2\pi R$ for a torus with major radius R.
First, the cylinder is discretized in the radial direction by defining N equidistant, cylindrical surfaces, see figure A.6. The radius of the i^{th} surface is given by

$$r_i \;=\; i\,\frac{a}{N}, \quad i = 1, \ldots, N \;,$$

and its area by

$$A_i \;=\; 2\pi L r_i \;.$$

The volume enclosed by two neighboring surfaces, which has the shape of a hollow cylinder, is given by

$$V_i \;=\; \pi L(r_i^2 - r_{i-1}^2) \;, \quad i = 2, \ldots, N \;.$$

The innermost surface encloses a solid cylinder that has the volume $V_1 = \pi L r_1^2$.

We assume that each of these N volumes has constant temperature T_i.
In general, the heat flux through an area A is given by

$$\frac{dQ}{dt} \;=\; \lambda A \frac{dT}{dx} \;,$$

where x is a spatial coordinate perpendicular to A and λ is the heat conductivity of the material. With the discretization made above, the temperature gradient across the area A_i, which separates the i^{th} from the $(i+1)^{th}$ volume, is given by

$$\frac{T_{i+1} - T_i}{r_{i+1} - r_i} \;=\; \frac{N}{a}(T_{i+1} - T_i) \;.$$

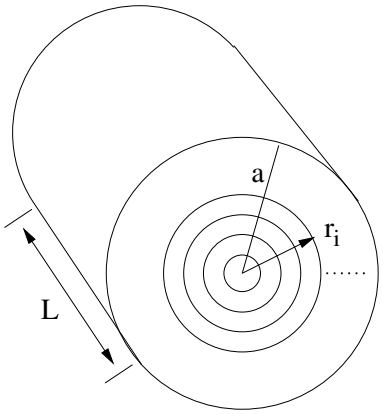

Figure A.6: *The cylindrical volume is subdivided into N hollow cylinders with outer radius r_i, $i = 1, \ldots, N$.*

We assume that each of the N volumes contains a local heat source P_i. Then, the net heat flux into the i^{th} volume is given by

$$\dot{Q}_i \;=\; \chi A_{i-1}(T_{i-1} - T_i) - \chi A_i(T_i - T_{i+1}) + P_i \;,$$

where the constant $\chi = \lambda N/a$ was introduced. The heat capacity of the i^{th} volume is $C_i = cV_i$, where the constant c depends on the material. Accordingly, the change of the temperature ΔT_i within the time Δt is given by

$$\Delta T_i \;=\; \frac{\dot{Q}_i}{C_i}\Delta t \;.$$

To study the temporal evolution of the temperature, we discretize the time axis. This leads to the following recursion formula for the temperature:

$$T_i(t_{j+1}) \;=\; T_i(t_j) \;+\; \frac{\chi A_{i-1}(T_{i-1}(t_j) - T_i(t_j)) - \chi A_i(T_i(t_j) - T_{i+1}(t_j)) + P_i}{cV_i} \qquad \text{(A.3)}$$

This equation holds for $i = 2, \ldots, N-1$. In the case $i = 1$, the first term in the numerator has to be dropped as the innermost volume is a solid cylinder, and in the case $i = N$, one has to introduce a boundary condition for the temperature, like a constant ambient temperature.
The simple heat transport model derived so far can be applied to solids, but also to plasmas. In the latter case, the constant χ is equivalent to the heat diffusion coefficient χ in equation (2.2) in chapter 2. One just has to take into account the factor n_e in this equation and accordingly change the above recursion formula. The first term in the numerator has to be multiplied by an additional factor $(n_{i-1}(t_j) + n_i(t_j))/2$, and the second one by $(n_i(t_j) + n_{i+1}(t_j))/2$.
An analogous recursion formula for the plasma density, which uses the transport coefficients from equation (2.1) in chapter 2, is given by:

$$\begin{aligned} n_i(t_{j+1}) \;=\; n_i(t_j) \;+\; \frac{1}{V_i}\cdot\Big[\;& DA_{i-1}(n_{i-1}(t_j) - n_i(t_j)) - DA_i(n_i(t_j) - n_{i+1}(t_j)) + \\ & + C_T A_{i-1}(T_{i-1}(t_j) - T_i(t_j)) \cdot \frac{n_{i-1}(t_j) + n_i(t_j)}{T_{i-1}(t_j) + T_i(t_j)} - \\ & - C_T A_i(T_i(t_j) - T_{i+1}(t_j)) \cdot \frac{n_i(t_j) + n_{i+1}(t_j)}{T_i(t_j) + T_{i+1}(t_j)} + v_p(n_i(t_j)A_i - n_{i-1}(t_j)A_{i-1}) \;\Big] \end{aligned} \qquad \text{(A.4)}$$

In the case $i = 1$, one has to drop the terms that contain expressions with the index $i-1$, and in the case $i = N$, one has to make an assumption on the particle flux through the outermost surface. One possibility is to set this flux to zero, which provides a conservation of the volume-integrated density and thus of the particle number.

An example

A computer program based on those recursion formulas was written, which shall now be tested for a simple example where the equilibrium temperature distribution can be calculated analytically:

We consider a solid cylinder which is heated with homogeneous power density p. A practical example of this would be a cylindrical metal rod through which a current along the cylinder axis is flowing, causing ohmic heating. The surface of the cylinder is kept at constant temperature $T_{ambient}$. The equilibrium temperature profile will be referred to as T(r). We consider a cylindrical area at radius r, see figure A.7. In the volume enclosed

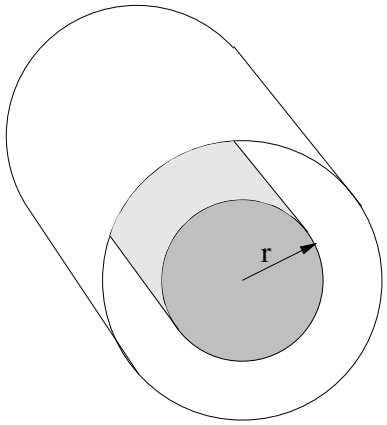

Figure A.7: *A cylinder is heated with homogeneous power density. In thermal equilibrium, the heating power deposited in the highlighted volume is conducted through the lightly shaded area.*

by this area, the power $P_{in} = pL\pi r^2$ is deposited. The heat flux through this area is $P_{out} = -2\pi r L \lambda \frac{dT(r)}{dr}$. In thermal equilibrium, we have $P_{in} = P_{out}$, which yields

$$\frac{dT(r)}{dr} = -\frac{p}{2\lambda} r \, .$$

The temperature profile can be obtained by integration, taking into account the boundary condition:

$$T(r) = T_{ambient} + \frac{pa^2}{4\lambda} - \frac{p}{4\lambda} r^2$$

Figure A.8 shows the analytical solution and the numerical solution for $N = 10$, $N = 20$, $N = 50$ and $N = 100$ for the case $p = 1$, $a = 1$ and $\lambda = 0.005$.

Evidently, the temperature obtained from the simulation is systematically above the analytical value in the center, but the deviation goes to zero in the limit $N \to \infty$. This offset could be avoided by replacing the definition of r_i with $r_i = (i - \frac{1}{2}) \frac{a}{N}$. However, as this model is only used for qualitative studies, the offset is not critical. The diagrams shown in figures 8.8 - 8.13 in chapter 8 would be qualitatively the same with the other definition of r_i.

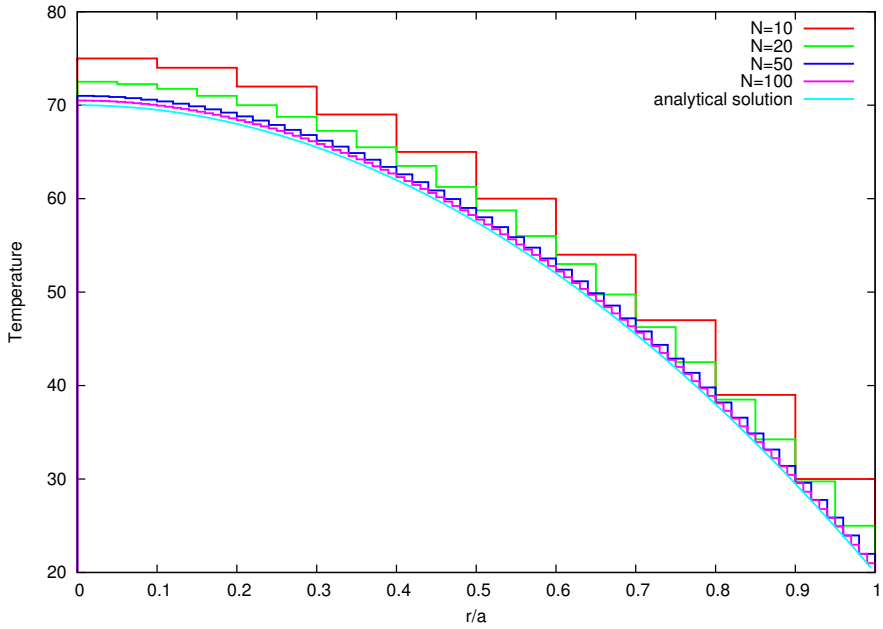

Figure A.8: *Temperature profile in a solid cylinder with radius* $a = 1$*, which is homogeneously heated with a power density* $p = 1$*. The heat conductivity of the material is assumed to be* $\lambda = 0.005$ *and the ambient temperature* $T_{ambient} = 20$*. The diagram shows the analytical solution and the numerical solution for* $N = 10$*,* $N = 20$*,* $N = 50$ *and* $N = 100$*.*

Bibliography

[1] *BP Statistical Review of World Energy June 2009* http://www.bp.com/statisticalreview

[2] H. S. Bosch: *Nuclear Fusion.* Lecture Notes in Physics **670** (2005) 445-460.

[3] W. Häfele, J.P. Holdren, G. Kessler et al.: *Fusion and fast breeder reactors.* International Institute for Applied System Analysis, Laxenburg, Austria (1977).

[4] S.J. Bame, J.E. Perry: $T(d,n)He^4$ *Reaction.* Physical Review **107** (1957) 1616-1620.

[5] Max-Planck-Institut für Plasmaphysik (IPP): *Kernfusion - Berichte aus der Forschung.* Folge 2 (2002) ISSN 0172-8482.

[6] C. Angioni, E. Fable, M. Greenwald et al.: *Particle transport in tokamak plasmas, theory and experiment.* Plasma Physics and Controlled Fusion **51** (2009) 124017.

[7] J. Stober: *Particle Transport in Magnetically Confined Fusion-Plasmas at High Density.* Habilitation Thesis, Ludwig-Maximilians-Univertität München, 2007.

[8] E. Fable, O. Sauter: *Gyrokinetic calculations of steady-state particle transport in electron internal transport barriers.* Plasma Physics and Controlled Fusion **50** (2008) 115005.

[9] J. Wesson: *Tokamaks.* Oxford engineering and science series, Oxford University Press, Oxford, second edition (1997).

[10] H. W. Bartels, H. S. Bosch, R. Brakel et al.: *IPP Summer University for Plasma Physics.* Lecture Notes (2007).

[11] G.R. Tynan, A. Fujisawa, G. McKee: *A review of experimental drift turbulence studies.* Plasma Physics and Controlled Fusion **51** (2009) 113001.

[12] R. Dux, R. Neu, A.G. Peeters et al.: *Influence of the heating profile on impurity transport in ASDEX Upgrade.* Plasma Physics and Controlled Fusion **45** (2003) 1815-1825.

[13] C. Angioni, A.G. Peeters, G.V. Pereverzev et al.: *Theory-based modeling of particle transport in ASDEX Upgrade H-mode plasmas, density peaking, anomalous pinch and collisionality.* Physics of Plasmas **10** (2003) 3225-3239.

[14] http://fusion.gat.com/theory/Gyromovies

[15] G.T. Hoang, C. Bourdelle, B. Pegourie et al.: *Particle Pinch with Fully Non-inductive Lower Hybrid Current Drive in Tore Supra.* Physical Review letters **90** (2003) 155002.

[16] C. Angioni, A.G. Peeters, X. Garbet et al.: *Density response to central electron heating: theoretical investigations and experimental observations in ASDEX Upgrade.* Nuclear Fusion **44** (2004) 827-845.

[17] C. Angioni, A.G. Peeters, F. Ryter et al.: *Relationship between density peaking, particle thermodiffusion, Ohmic confinement, and microinstabilities in ASDEX Upgrade L-mode plasmas.* Physics of Plasmas **12** (2005) 040701.

[18] F. Leuterer, M. Beckmann, A. Borchegowski et al.: *The ECRH system of ASDEX Upgrade.* Fusion Engineering and Design **56-57** (2001) 615-619.

[19] N. K. Hicks, W. Suttrop, K. Behler et al.: *FAST SAMPLING UPGRADE AND REAL-TIME NTM CONTROL APPLICATION OF THE ECE RADIOMETER ON ASDEX UPGRADE.* Fusion Science and Technology **57** (2010) 1-9.

[20] G. Braithwaite, N. Gottardi, G. Magyar et al.: *THE JET POLARI-INTERFEROMETER.* Review of Scientific Instruments **60** (1989) 2825.

[21] K. Kawahata, K. Tanaka, Y. Ito et al.: *Far infrared laser interferometer system on the Large Helical Device.* Review of Scientific Instruments **70** (1999) 707-709.

[22] D. Veron: *HIGH SENSITIVITY HCN LASER INTERFEROMETER FOR PLASMA ELECTRON DENSITY MEASUREMENT.* Optics communications **10** (1973) 95-98.

[23] V.G. Petrov: *Influence of Refraction on Plasma Density Measurements.* Plasma Physics Reports **32** (2006) 311-316.

[24] V.V. Kubarev, E.A. Kurenskii: *Ultralow-noise high-power DCN laser with rf pumping.* Quantum Electronics **26** (1996) 303-306.

[25] O. Gehre: Personal communication.

[26] H.R. Koslowski: *A real-time multiradian phase detector for interferometry based on a digital phase locked loop.* Measurement Science and Technology **5** (1994) 307-309.

[27] M. Maraschek: Personal communication.

[28] A. Mlynek, G. Schramm, H. Eixenberger et al.: *Design of a digital multiradian phase detector and its application in fusion plasma interferometry.* Review of Scientific Instruments **81** (2010) 033507.

[29] Y. Ito, K. Tanaka, T. Tokuzawa et al.: *Development of a phase counter with real-time fringe jump corrector for heterodyne interferometer on LHD.* Fusion Engineering and Design **74** (2005) 847-851.

[30] K. Behler, H. Blank, H. Eixenberger et al.: *Real-time diagnostics at ASDEX Upgrade - Architecture and operation.* Fusion Engineering and Design **83** (2008) 304-311.

[31] C. Gil, A. Barbuti, D. Elbeze et al.: *Fringe jump analysis and electronic corrections for the Tore Supra far infrared interferometer.* Review of Scientific Instruments **79** (2008) 10E710.

[32] C. Mazotta, O. Tudisco, A. Canton et al.: *Measurement of density profiles using the new infrared scanning interferometer for FTU.* Physica Scripta **T123** (2006) 79-83.

[33] W. Schneider, P.J. McCarthy, K. Lackner et al.: *ASDEX Upgrade MHD equilibria reconstruction on distributed workstations.* Fusion Engineering and Design **48** (2000) 127-134.

[34] L. Giannone, W. Schneider, P.J. McCarthy et al.: *Real time magnetic field and flux measurements for tokamak control using a multi-core PCI Express system.* Fusion Engineering and Design **84** (2009) 825-828.

[35] K. McCormick, R. Dux, R. Fischer et al.: *Main chamber high recycling on ASDEX Upgrade.* Journal of Nuclear Materials **390-391** (2009) 465-469.

[36] http://www.windriver.com/products/vxworks/

[37] http://www.ni.com/

[38] http://www.sun.com/

[39] A. Kallenbach, A. Carlson, G. Pautasso et al.: *Electric currents in the scrape-off layer in ASDEX Upgrade.* Journal of Nuclear Materials **290-293** (2001) 639-643.

[40] F. Ryter, T. Pütterich, M. Reich et al.: *H-mode threshold and confinement in helium and deuterium in ASDEX Upgrade.* Nuclear Fusion **49** (2009) 062003.

[41] F. Ryter, F. Leuterer, G. Pereverzev et al.: *Experimental Evidence for Gradient Length-Driven Electron Transport in Tokamaks.* Physical Review Letters **86** (2001) 2325-2328.

[42] D. Stotler: *Sawtooth Crash Animation.* http://w3.pppl.gov/~dStotler/sawtooth.html

[43] http://en.wikipedia.org/wiki/Acousto-optic_modulator

[44] M. Van Zeeland: Personal communication.

Danksagung

An dieser Stelle möchte ich mich ganz herzlich bei all jenen bedanken, ohne die diese Arbeit und vor allem die damit zusammenhängenden Experimente niemals möglich gewesen wären. Neben allen anderen wissenschaftlichen und technischen Mitarbeitern des ASDEX Upgrade Teams gilt mein besonderer Dank...

- Herrn Prof. Dr. Hartmut Zohm für die Möglichkeit, in seinem Bereich eine Doktorarbeit anzufertigen, und natürlich für seine intensive und wertvolle Betreuung und Unterstützung.
- George Sips und François Ryter für die Betreuung meiner Arbeit.
- Clemente Angioni für die aufschlussreichen Diskussionen über turbulenten Transport.
- Kent McCormick für die Einführung an ASDEX Upgrade und in die Plasmainterferometrie, sowie natürlich dafür, dass er zu jeder nur erdenklichen Tages- und Nachtzeit ein offenes Ohr für meine Fragen hatte und stets Geschichten aus seiner jahrzehntelangen Karriere in der Fusionsforschung zu erzählen hatte.
- Josef Bönisch, der mir den gesamten Interferometeraufbau zeigte und mir bei meinen ersten Schritten im Institut so liebenswert zur Seite stand, wenn auch die Zeit der Zusammenarbeit wegen seines Eintritts in den Ruhestand leider nur von kurzer Dauer war.
- Jörg Eheberg und Johannes Friesen für die allzeit gute Zusammenarbeit, die weit über den täglichen Betrieb des Interferometers hinausging.
- Gerold Schramm, der mir gleich in meinen ersten Wochen am Institut bereitwillig Lötkolben und Bauteile in die Hand gab und meinen Eigenentwicklungen bei der Ausleseelektronik nicht nur freien Lauf ließ, sondern mir auch stets mit Rat zur Seite stand.
- Horst Eixenberger, der meine gedruckte Schaltung auf einem CPLD implementierte und bei allen Fragen zur Elektronik stets ein offenes Ohr für mich hatte, sowie seinem jungen dynamischen Elektroniker-Team, bestehend aus Sven Klink, Thomas Schwarz, Andreas Wöls und Ludwig Kammerloher.
- Matthias Reich, der das Programm-Template für Echtzeitdiagnostiken so energisch vorangetrieben und meine Experimente damit letztlich erst ermöglicht hat. Natürlich sei ihm an dieser Stelle auch für die Geduld gedankt, die er mitunter aufzubringen hatte, wenn in einem von mir geschriebenen Programmteil wieder mal ein 'copy & paste'-Fehler steckte.
- Albert Kagarmanov, der die Template-Programmierung fortführte und für mich die Ursache des einen oder anderen 'segmentation fault' aufspürte.
- Manfred Zilker, ohne dessen Hilfe ich den Linux-Treiber für das PCI-Entwicklerboard niemals zum Laufen bekommen hätte, das letztlich die Datenaufnahme mit der zweiten Generation der DCN-Ausleseelektronik ermöglichte.

- Richard H. Cole, den ich nicht nur wegen seiner Programmierfähigkeiten zu schätzen lernte, sondern vor allem auch wegen seiner stets freundlichen und herzlichen Art, die eine echte Bereicherung für die tägliche Arbeit im Kontrollraum war.
- Klaus Lüddecke, der in Rekordzeit die Echtzeitkommunikation zwischen meiner Diagnostik und der schnellen Steuerung zum Laufen brachte.
- Karl Behler und seinem gesamten Team für die Bereitstellung all der Hard- und Softwarekomponenten, die meine Experimente letztlich ermöglicht haben. Besonderer Dank gilt dabei Andreas Lohs, der sich viel Zeit nahm, als die erste Datenaufnahme mit der neuesten Generation der DCN-Ausleseelektronik anstand.
- Christoph Fuchs für seine jederzeitige Unterstützung, wenn ich Fragen zu den Datenbank-Zugriffsroutinen hatte.
- Louis Giannone, der die erste Hälfte meines Algorithmus zur Profilberechnung in Rekordzeit von C++ nach LabView übersetzte.
- Wolfgang Treutterer, der den neuen Regler für die Profilkontrolle bereitstellte, sowie natürlich auch Thomas Zehetbauer, Dieter Zasche und Gregor Neu.
- Wolfgang Zeidner und Gaby Fröhlich, deren FARO-Messung Ende 2007 wir die genaue Kenntnis der Koordinaten der DCN-Sichtlinien verdanken.
- Andreas Bolland und Anton Mayer, auf deren Hilfe beim Betrieb und Umbau der Bremsstrahlungsdiagnostik ich mich stets verlassen konnte - wenn auch diese Diagnostik letztlich keinen Eingang in meine Dissertation fand.
- den Sekretärinnen Frau Bauer, Frau Jordan, Frau Jung, Frau Porsch und natürlich ganz besonders Frau Daube, die sich bei der Organisation von Dienstreisen immer so viel Zeit für mich nahm.